Spectroscopy and Systematic Effects: an eEDM experiment using BaF molecules

Marshall, Virginia Rose

DOI:
10.33612/diss.972290628

Spectroscopy and Systematic Effects: an eEDM experiment using BaF molecules

Cover: an abstract version of an interference spectrum, referencing those shown in Chapter 5 of this thesis. Credit to Dr. Sylvia Rousseva.

university of groningen

Nikhef

The work in this thesis has been carried out at the Van Swinderen Institute for Particle Physics and Gravity of the University of Groningen. This work is done as part of the NL-*e*EDM consortium which receives funding (EEDM-166) from the Dutch Research Council (NWO). This work originates as part of the research programme of the Foundation for Fundamental Research on Matter (FOM), and falls as of 1 April 2017, under the responsibility of Netherlands Foundation of Scientific Research Institutes (NWO-I), which is part of the Dutch Research Council (NWO).

Cover: Dr. Sylvia Rousseva
Printing: Gildeprint

university of groningen

Spectroscopy and Systematic Effects: an *e*EDM experiment using BaF molecules

PhD Thesis

to obtain the degree of PhD at the
University of Groningen
on the authority of the
Rector Magnificus Prof. J.M.A. Scherpen
and in accordance with
the decision by the College of Deans.

This thesis will be defended in public on

Tuesday 23 April 2024 at 12:45 hours

by

Virginia Rose Marshall

born on 3 November 1993
in Southampton, UK

Supervisor
Prof. S. Hoekstra

Co-Supervisor
Dr. L. Willmann

Assessment committee
Prof. R.A. Hoekstra
Prof. T. Langen
Prof. M. Merk

Contents

Chapter 1

Introduction: the eEDM and its connection to the Standard Model

1.1 The Electron's Electric Dipole Moment (eEDM)

Probing the properties in particles of the Standard Model of particle physics (SM) with high precision allows complimentary experiments to those that can be undertaken using high energy experiments such as those at particle accelerators. Particle physics experiments have been searching for violation of charge-parity conjugation symmetry (CP- violation) since its discovery in 1964 in the decays of neutral kaons [1]. A non-zero CP violating permanent electric dipole moment of an elementary particle would further constrain the SM and its possible extensions significantly [2]. Such extensions include models which try to explain the apparent matter- antimatter asymmetry in the universe. Many experimental approaches, including the LHCb experiment [3], are searching for sources of this violation that may contribute towards explaining the observed asymmetry.

One burgeoning area is the search for the electron's electric dipole moment (eEDM), which has been a source of much experimental interest for decades. The eEDM implies a non-uniform charge distribution along the spin axis of the electron itself, which is at odds with time-reversal (or CP-violation under the CPT theorem) invariance [4]. Much literature has been written on this topic [5–8], and as such the focus of this report will not be the theory or the origin of an eEDM, but rather the experimental search for it.

While recent SM calculations predict a value of the eEDM to be $\mathrm{d_e} \leq 10^{-35}$ e cm [9], extensions to the SM yield predictions that are larger by many orders of magnitude and could in some cases reach up to the present experimental bounds. Although the SM value remains smaller than is currently possible to measure experimentally, new technologies have enabled an ever increasing measurement sensitivity, and recent measurements have allowed a new upper limit of $|\mathrm{d_e}| < 4.1 \times 10^{-30}$ e cm (90% confidence level) [10] to be found. An upper limit this large means that theories that aim to improve upon the SM in order to explain some of its yet unexplained features, such as Supersymmetry (SUSY), can be constrained by the experimental results [11], independent of potential contributions to the matter dominance problem.

1.2 Measuring the eEDM in a molecule

In compound systems such as molecules, there is an enhancement factor for a potential EDM on the electron which arises from the molecular structure of certain paramagnetic polar diatomic molecules, which induces a permanent molecular EDM [12–15]. This enhancement gives rise to a much larger permanent EDM which therefore could be observed for the molecules. The size of the induced EDM means that it is experimentally preferential, as it is orders of magnitude larger than the eEDM itself. Predictions of the eEDM from SM extensions include values that are within experiment reach when this enhancement factor is applied, and can therefore be constrained by measurement using molecules with such enhancement factors.

1.3 Observable in an eEDM measurement

The frequency ω of the precession of a particle's spin in an electric $\vec{E}$ or magnetic $\vec{B}$ field is related to the respective dipole moments $\vec{d}$ and $\vec{\mu}$ via the corresponding Hamiltonian [4, 16]

$$H = \hbar\omega = -\vec{\mu}\vec{B} - \vec{d}\vec{E}. \tag{1.1}$$

Measuring ω with precisely known $\vec{B}$ and $\vec{E}$ fields allows the determination of the eEDM. However, the eEDM is as of yet immeasurably small and as such an upper limit derived from the experimental value is of interest. This can be determined from the statistical uncertainty of the value.

The eEDM measurement is inherently statistically limited, and the statistical uncertainty σ_d that can be achieved for polar diatomic molecules is given by [17]

$$\sigma_d = \frac{\hbar}{E \cdot A \cdot P(E) \cdot \varepsilon \cdot T \cdot \sqrt{n}}, \tag{1.2}$$

where E is the external applied electric field (below saturation level, i.e.: in the case of BaF, $E < E_{\text{sat}} \approx 8.3$ kV/cm), A is the molecular enhancement factor (sometimes shown as $E_{\text{eff}} = E \cdot A$), $P(E)$ is the molecular polarisation factor (which is a function of the electric field) [18], ε is the total measurement efficiency, T is the interaction time, and n is the total number of uncorrelated atoms or molecules during the time of an experiment T_{total}. Here it is assumed that the interaction time T is the same as the coherence time in the experiment. For a beam of flux dn/dt, where dt is a general time variable and dn is the number of uncorrelated particles in that time, n can be replaced with $(dn/dt) \times T_{\text{total}}$. The total measurement efficiency depends on many experimental parameters, such as the percentage of molecules that are detected by the setup and the efficiency of the measurement devices [19, 20].

In order to reduce the uncertainty of the measurement, it is therefore necessary to maximise the variables in the denominator of Equation 1.2. The value of $\mathrm{E_{eff}}$ is given by the molecule, and in this experiment barium monofluoride (BaF) has specifically been chosen in part because of its value for $\mathrm{E_{eff}}$, combined with the fact that large T and n values can be achieved using a cryosource, deceleration and laser cooling. The coherent interaction time depends on the state of the molecule during the interaction. The value of n can be maximised by increasing the number of molecules in the beam and T can be increased by having longer coherent interactions with the molecules.

Several different molecules with similar properties (e.g.: ThO [21], YbF [22], HfF^+ [10, 23]) have been employed for measuring an eEDM value. There are several groups worldwide with great interest in finding new candidates for eEDM measurements [24–30]. Each of them have different advantages: for example, for some it may be experimentally simpler to create a slow beam for an increased interaction time T, some may have a higher E_{eff} value, some can also be transversely laser cooled efficiently to create a narrower beam with fewer losses and therefore increase N, and some can be trapped to increase T. In addition, molecules with 3 or more atoms can have a structure with internal comagnetometry that allows reversal of the EDM interaction without switching the direction of the externally applied fields [26]. When choosing the candidate for the eEDM measurements, these advantages are all taken into account. It is essential to probe eEDMs using multiple different atomic, molecular and ionic species to separate the sources of CP violation and experimental systematic effects, so these different experiments are complementary.

1.4 Present landscape of measurements

In 1958, the first experimental limit on the eEDM, based on calculating corrections to the Lamb shift of hydrogen [31], found an upper limit of $|d_e| < 10^{-13} e$ cm. Since then, this upper limit has been reduced by many orders of magnitude. Since the 1960s, when Sandars realised the enhancement factor provided by atoms and molecules to measure the eEDM [32], there have been many measurements of the eEDM using many different atomic and molecular beams, traps and other methods.

In the last few decades, there have been several experiments running that measure the upper limit and value of the eEDM with various setups. Some of the most common have been atomic and molecular beams, but in recent years developments with atomic, ionic and molecular trapping have allowed some projects using these methods. The most recent results of some of the groups attempting to measure the eEDM are shown in Table 1.1.

System	d_e Value (e cm)	Upper Limit (e cm) and Confidence Level	Year	Ref
Cs	$(-1.5 \pm 5.5_{\text{stat}} \pm 1.5_{\text{sys}}) \times 10^{-26}$	1.2×10^{-25}, unstated	1989	[33]
Tl	$(6.9 \pm 7.4) \times 10^{-28}$	1.9×10^{-27} at 90 %	2002	[34]
YbF	$(-2.4 \pm 5.7_{\text{stat}} \pm 1.5_{\text{sys}}) \times 10^{-28}$	1.2×10^{-27} at 90 %	2011	[22]
ThO	$(4.3 \pm 3.1_{\text{stat}} \pm 2.6_{\text{sys}}) \times 10^{-30}$	1.1×10^{-29} at 90 %	2018	[21]
HfF^+	$(-1.3 \pm 2.0_{\text{stat}} \pm 0.6_{\text{sys}}) \times 10^{-30}$	4.1×10^{-30} at 90 %	2023	[10]

Table 1.1: Most recent results of searches for the eEDM using various atoms and molecules, showing the value measured along with the upper limit found with its associated confidence level. Also shown is the year at which these measurements were performed, showing that both the upper limits and the value have reduced by several orders of magnitude over time.

A cryogenic beam of ThO in combination with stimulated Raman adiabatic passage (STIRAP) while switching electric fields was used to set the previously best limit on

the eEDM value [21]. Our experiment uses BaF, also proposed for eEDM searches for embedded molecules in a solid rare-gas matrix such as neon or argon [24, 25]. In such a matrix, the polar molecules have a fixed orientation so the electric field direction is not required to be switched. eEDM experiments using YbF created in a supersonic source similar to this work have also been undertaken with results shown in Table 1.1. Upgrades of this experiment are ongoing to improve the precision by 2 to 3 orders of magnitude [35].

As technologies such as trapping have developed, new limits for the eEDM have been found. Results using trapped HfF^+ ions have, at the time of writing, the best limit on the eEDM [10]. The technique allows interaction times of up to 3 s to be achieved. In addition, as the field of polyatomics develops, molecules that have more complex structure with three or more atoms, such as BaOH and YbOH [36], are beginning to be investigated [27, 37, 38].

1.4.1 Further reading from the eEDM collaboration

This work was undertaken within a collaboration and as such other theses and published work can be used in combination to have a full picture where it is relevant. The advantage of the NL-eEDM collaboration's approach is that in addition to its sensitivity to the eEDM, BaF molecules can be created in a cryogenic source, laser cooled and decelerated in a Stark Decelerator to provide a bright, slow and cold molecular beam [39].

The BaF molecules are created in a supersonic source which is described in a paper and Parul Aggarwal's thesis [40, 41]. The lifetimes of the excited states used in this thesis have been studied [42]. Hyperfine structure taken from spectroscopy results given in this thesis have been compared to calculations in a paper to benchmark calculated molecular constants [43]. The molecules travel through an interaction zone inside a magnetic shield, which is the subject of Thomas Meijknecht's thesis [18]. The data acquisition created for running, pulsing, controlling and measuring many parameters of the experiment is detailed in Anno Touwen's thesis [44]. The calculations of the optical Bloch equations that can be compared to the experimental results of the coherent state transfer are described in Alexander Boeschoten's thesis [45]. These calculations have been compared to experimental results in order to understand the systematic effects that can take place in a paper currently circulated as a pre-print [46]. In addition, Chapter 2 of [46] shows the calculations for BaF molecules in electric and magnetic fields. Conclusions of these works are given in Chapters 3 and 5 where necessary to provide the context in relation to the results given here.

Further developments include highly intense sources (Maarten Mooij's thesis and articles [47–49] and Kevin Esajas's thesis [50]), deceleration to standstill and trapping of molecules using a decelerator (Artem Zapara's thesis [51], and Parul Aggarwal's thesis [41] and articles with Yanning Yin [52]), manipulation of the Baf beam using an electrostatic hexapole (Anno Touwen's thesis and articles [44, 53]), calculations of molecular constants to understand and support laser cooling (Yongliang Hao's thesis and articles [54, 55]), calculations of molecular properties to estimate eEDM enhancement effects (Pi Haase's thesis and publications [15, 56]) and calculations of the excited state hyperfine structure of BaF (Malika Denis's article [43]).

1.5 Thesis overview

The focus of this thesis is on the experimental work undertaken towards an eEDM experiment within the NL-eEDM collaboration using a supersonic beam of BaF molecules. Spectroscopy of many low-lying states of the BaF molecule has been undertaken and the results are shown. The optical systems used to create, measure and readout the spin precession process are described, and the results are discussed. The quantification of specific possible systematic effects in our experiment are investigated and compared to calculations using the optical Bloch equations. The structure of this thesis is as follows:

Chapter 1 has given a general introduction to eEDMs and the context within which the collaboration carried out their work.

Chapter 2 gives details on the NL-eEDM collaboration's experiment including why BaF was chosen, a discussion of what is required to build an eEDM experiment, details on the BaF molecule and a discussion of the setup that has been built, and outlook of the experiment.

Chapter 3 discusses the optical setup and lasers used in the experiment, along with how they are used in the different sections. Information is given for how the molecule is manipulated and measured using optical systems and laser beams. The optical methods used to enable the coherent state transfer for the spin precession measurement are described. The molecules fly through an interaction zone with a high electric field inside a magnetic shield and the results of the steps taken to setup and control the measurements are shown.

Chapter 4 shows the results of spectroscopy of the BaF molecule. This chapter describes the vibrational, rotational and hyperfine splittings for low ground and excited states of the BaF molecule, along with transition frequencies necessary to address specific states optically.

Chapter 5 The results of the spin precession measurement are shown with the interference spectra. By varying specific parameters of the optical setup such as frequency or power, the results can be combined with calculations using the optical Bloch equations to understand and quantify possible systematic effects.

Chapter 6 discusses the overall conclusions and impact on future work in combination with other work from the eEDM collaboration.

Chapter 2

An eEDM sensitive search using BaF

Here, the essence of the NL-eEDM collaboration is introduced. The experiment uses barium monofluoride (BaF) molecules, which have enhancement effects on the measurement of the eEDM that have been calculated. The quantum structure including the particular states and transitions used in this experiment are discussed. The concepts that are central to the measurement of the eEDM are introduced such as the differential measurement method and spin precession of a superposition state.

An introduction to the control of the asymmetry and quantification of systematic effects is given. A coherent state transfer methodology is given and a description of the experimental setup that has been built during this work is shown. For some parts of the collaboration, a full description can be found elsewhere and is therefore beyond the scope of this thesis. For example, the homogeneous magnetic and electric field region created by the interaction zone device is the focus of [18], and the optical Bloch equation and quantum state calculations are the focus of [45]. For these topics, an explanation of the relevant experimental infrastructure and conclusions of calculations and experiments are given.

2.1 The BaF molecule for an eEDM measurement

Certain molecules are used to measure the eEDM due to their molecular structure providing an enhancement factor in the electric field strength that the electron undergoes (see Section 1.2). It is important for there to exist multiple experimental searches using different species, so that the parameter space for eEDM predicting theories can be more extensively mapped [15, 57]. One molecule that possesses this previously mentioned enhancement effect is BaF, where the ground state $X^2\Sigma^+(v = 0, N = 0, F = 1)$ state is used [39].

While the BaF molecule has a smaller enhancement effect than some other eEDM enhancing molecules, it has some advantages that make it an attractive candidate for an experiment. It is a neutral molecule that can be produced in a cryogenic source [47–49] with a large molecule number output and slow velocity. In addition,

its molecular structure means it can undergo Stark deceleration [39], laser cooling [54]and manipulated using an electrostatic hexapole [44, 53].

2.1.1 Electric field enhancement effects of BaF

In molecular systems such as BaF, the single valence electron experiences enhanced electric field sensitivity due to close lying rotational levels with opposite parity [15]. Those states are therefore strongly mixed in external fields. The linear Stark shift induced is the measurement signal used to extract the eEDM itself.

The permanent molecular EDM that is measured also has a contribution from the PT-odd (meaning that there is both a parity and a time-reversal symmetry violation) scalar-pseudoscalar (S-PS) interaction between the electrons and nucleons, which is also enhanced by the molecular structure. To extract a limit on the eEDM, the molecular enhancement factors W_d (for eEDM magnitude) and W_s (for S-PS interaction magnitude) have recently been calculated [15]. Both of these are required to be understood in order to extract the eEDM, and measurements of multiple species with different W_d/W_s ratios are essential to separate the linear combination of these two effects that a single energy shift measurement can provide.

The experimental observable of W_d and W_s depends on the polarisation factor P of the particular state during a coherent interaction time T. The results of a calculation of P for different rotational levels are shown in Figure 2.1. A typical field strength in the experiment of 10 kV/cm gives the $N = 0$ state a polarisation factor of 50 %, while for other rotational states the effect is smaller.

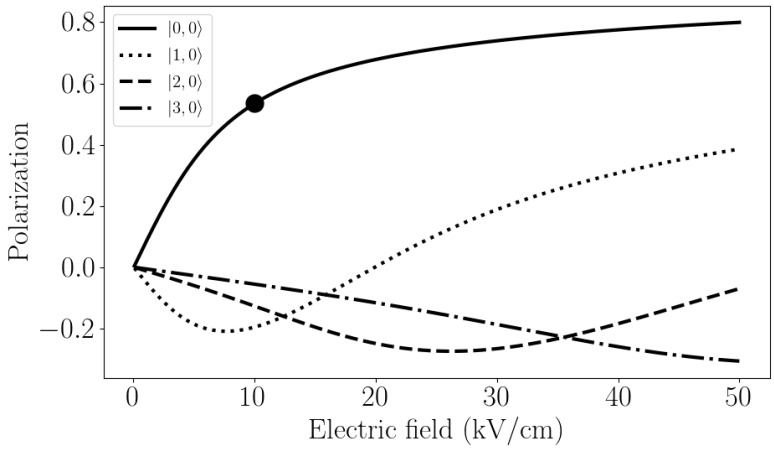

Figure 2.1: The polarisation curves $P(E)$ for the $M_N = 0$ components of the lowest four rotational levels of the $X^2\Sigma^+(v = 0)$ state in BaF, labelled using their states in zero externally applied field and in the format $|N, M_N\rangle$. The typical experimental electric field strength of 10 kV/cm is shown as a point on the $N = 0$ line. Figure taken from [15].

2.2 Concept of experiment

2.2.1 Differential measurement to extract energy difference

Following the discussion in Chapter 3 of [45], effects such as the eEDM and the S-PS interactions give the P,T-violating EDM of a molecule $D^{\not P,\not T}$. In the eEDM experiment, energy differences in magnetic sublevels of the $X^2\Sigma^+(v = 0, N = 0)$ ground state of the BaF molecule are measured. This energy difference between the $F = 1, m_F = \pm 1$ magnetic sublevels in electric and magnetic fields is given by

$$\Delta W(\hat{E} = \pm\hat{B}) = 2(\mu B \pm D^{\not P,\not T}E), \tag{2.1}$$

which shows that the energy shift is defined not only by the EDM, but by a Zeeman shift due to the magnetic dipole moment of the system. This gives a large background that is difficult to separate from the much smaller eEDM as $\mu B \gg D^{\not P,\not T}E$. This is overcome by doing a differential measurement. By flipping the direction of the magnetic field with respect to the electric field, which constitutes a P or T transformation, and subtracting one energy difference from the other:

$$\Delta W(\hat{E} = \hat{B}) - \Delta W(\hat{E} = -\hat{B}) = 4D^{\not P,\not T}E. \tag{2.2}$$

The only contribution that remains is due to the symmetry violating effects. In the experiment, it is more practical to flip the electric field direction because a magnetic field reversal involves magnetisation of magnetic material in the proximity of the experiment, which is associated with hysteresis. The experimental concept under T and P transformations is shown in Figure 2.2. The hyperfine structure in zero magnetic or electric fields is given by ω^0_{HFS}. * The addition of an electric field means that the F, M_F states do not remain pure basis states, but the labelling is kept for clarity. The tensor Stark shift $\omega_{\mathrm{tensor}} \gg \mu B \gg D^{\not P,\not T}E$, and is discussed in Sections 2.8 and 3.3 of [45]. Its shifts are shown in Figure 2.3.

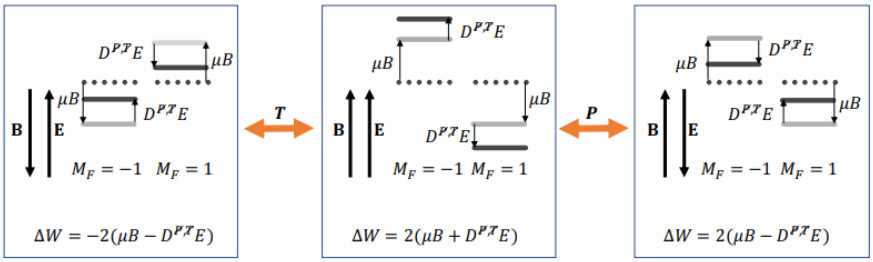

Figure 2.2: Principle of the NL-eEDM experiment. The energy difference between two magnetic substates, $\Delta W = W_{M_F=-1} - W_{M_F=1}$ is measured for electric and magnetic fields parallel and anti-parallel. The Zeeman shift is far larger than the shift from an eEDM, ie: $\mu B \gg D^{\not P,\not T}E$. Not to scale. Figure and caption taken from [45].

*The value of ω^0_{HFS} is measured with Hz precision in the process of the spin precession (Chapter 5) and is in agreement with the measured value presented in Chapter 4.

2.2.2 Spin precession and readout

Additional energy levels are included in the description of the experimental procedure. The involved states are described in [45], which will be referred to within this section. Figure 2.3 shows the relevant states in a particular electric and magnetic field configuration, which includes the $F = 0$ and $F = 1, m_F = 0$.

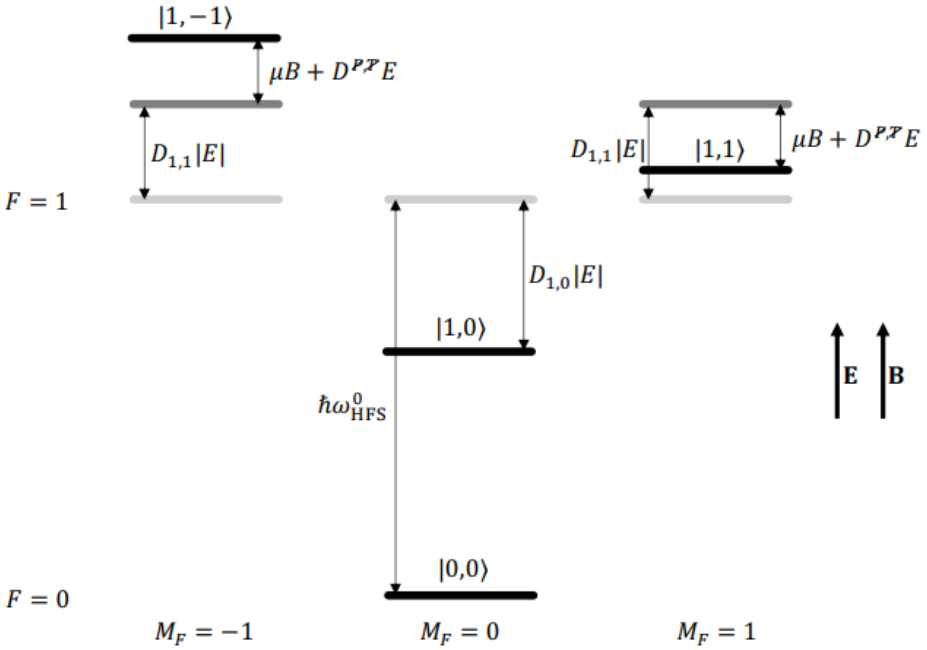

Figure 2.3: Energy levels of the ground state $X^2\Sigma^+(N = 0, F = 0)$ and $(F = 1)$ in electric and magnetic fields, with notation $|F, M_F\rangle$ for the levels. The tensor Stark shift is parameterised by coefficients $D_{i,j}$. In zero fields (in light grey), the $F = 0$ and $F = 1$ are split by $\omega^0_{\mathrm{HFS}} \approx 2\pi \times 65.8484$ MHz (b_F). The electric field changes the splitting between $|0, 0\rangle$ and $|1, 0\rangle$ with $D_{1,0}/\hbar = -20$ kHz/(kV/cm) and the splitting between the $|0, 0\rangle$ and the $|1, \pm1\rangle$ with $D_{1,1}/\hbar = 10$ kHz/(kV/cm) at $|E|= 10$ kV/cm (in dark grey). The magnetic field and EDM interaction break the degeneracy of the $|1, \pm1\rangle$ levels with $\mu B + D^{\mathcal{P},\mathcal{T}}E$ (in black). In an electric field there will also exist a tensor Stark shift $\omega_{\mathrm{tensor}} >> \mu B >> D^{\mathcal{P},\mathcal{T}}E$. Energies not to scale. Figure taken and caption adapted from [45].

In order to gain access to the small energy shifts at the scale of a molecular EDM, the experiment exploits interference effects. The molecules undergo spin precession within a large, homogeneous electric field region and well controlled homogeneous magnetic field in the same region [58]. The initial and the final population distribution is measured. The eEDM-sensitive signature is in the build up of the phase ϕ (see Equation 2.5) during the spin precession. By observing a phase difference, the full frequency shift due to the molecular EDM induced from the eEDM is extracted without measuring a full phase cycle. We expect an eEDM sensitivity on the phase

precession of order 10^{-5} rad in the first phase of our experiment.

The spin precession experiment is made up of different steps, the names of which are in italics for easy referencing in later sections. A description of the steps is given here, and is also be found in Section 3.4 of [45]. The middle steps are shown graphically in Figure 2.5.

The molecules arrive in the interaction zone having had a population transfer from $|F, m_F\rangle = |1, -1\rangle$ and $|1, +1\rangle$ into the $|0, 0\rangle$ hyperfine sublevel (see Section 3.4.3 for details). This step is called ***state preparation*** and takes place before the molecules are within the well controlled electric and magnetic fields of the interaction zone. In an ideal case, total population transfer would take place. The remaining population in the $|1, \pm 1\rangle$ sublevels give a background offset which reduces the fringe contrast as described in Section 5.2.2. In the following description the remaining population and therefore background offset is assumed to be 0.

Once the molecules are within the homogeneous field region, the ***first pulse*** arrives to transfer the molecules from the $|0, 0\rangle$ sublevel into a superposition described at a general time t by

$$|\psi(\mathrm{t})\rangle = \frac{1}{\sqrt{2}}(|1, -1\rangle \pm |1, +1\rangle), \tag{2.3}$$

where the bright state $|x\rangle$ (the state coupled to by the laser light) is the addition, and the dark state $|y\rangle$ (the state not coupled to by laser light due to its polarisation) is the subtraction. A full transfer to $|x\rangle$ from $|0, 0\rangle$ is called a perfect π-pulse.

The transition between $|0, 0\rangle$ and the superposition is between sublevels of the rotational state $N = 0$ and microwave frequencies equal to the hyperfine structure of the state are therefore required. Due to selection rules, a single photon optical transition cannot be used. It would be possible to directly apply a microwave frequency using a microwave horn. In the NL-eEDM experiment, the frequency is applied using a two-photon transition via a virtual excited state. A not-to-scale diagram of this process is shown in Figure 2.4. Two laser frequencies are combined in a single beam and are directed to counterpropagate antiparallel with the molecular beam (See Section 3.4.5). The laser beams are both pulsed on simultaneously to interact with the molecules at the beginning of the interaction zone [18].

After the ***first pulse***, a time period T passes as the molecules travel through the interaction zone which is called the ***precession period***. In this period the molecules interact with the homogeneous magnetic and electric fields within the interaction zone. The precession of the superposition will create different phases for the two states described after a time T by

$$|\psi(T)\rangle = \frac{e^{-i\phi/2}}{\sqrt{2}}(e^{-i\phi/2}\,|1, -1\rangle + e^{+i\phi/2}\,|1, +1\rangle), \tag{2.4}$$

where the phase difference ϕ between the two states of the superposition is given by

$$\phi = 2(\mu B + D^{\mathcal{P},\mathcal{T}} E)T/\hbar. \tag{2.5}$$

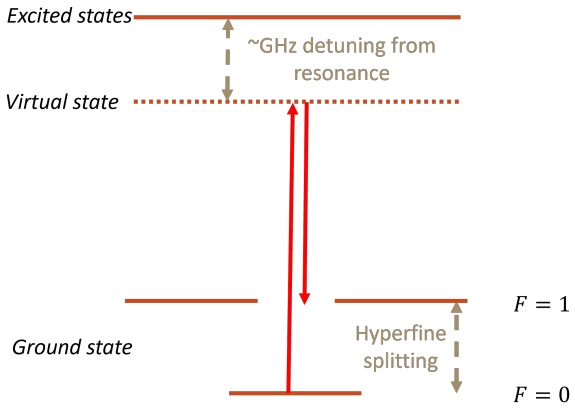

Figure 2.4: Energy level diagram showing the transitions used to undertake a two-photon transition from the $|0,0\rangle$ sublevel to a superposition of the states $|1,\pm1\rangle$. The magnetic sublevels m_F are not shown. The excited state used is the $A^2\Pi_{1/2}(J = 1/2)$ level which has two hyperfine sublevels ($F = 0, 1$). Two laser frequencies are applied with a frequency difference equal to the hyperfine splitting in the ground state $X^2\Sigma^+(N = 0, F = 0, 1)$. Not to scale.

Using an all-optical method ensures that we have excellent timing and amplitude control for the pulses, which means we have great control over the phase build up ϕ. This is discussed in greater detail in Chapter 3 and Chapter 5.

Omitting the overall phase and rewriting Equation 2.4 for the case of a π-pulse in terms of $|x\rangle$ and $|y\rangle$ after a precession time T gives

$$|\psi(T)\rangle = \frac{1}{\sqrt{2}}(e^{-i\phi/2}\,|1,-1\rangle + e^{+i\phi/2}\,|1,+1\rangle) = \cos\left(\frac{\phi}{2}\right)|x\rangle - i\sin\left(\frac{\phi}{2}\right)|y\rangle\,. \quad (2.6)$$

This shows that the state ψ oscillates between the bright and dark state over time. The Larmor frequency of this precession is given by

$$\omega = \frac{\phi}{T} = 2(\mu B + D^{\not{p},\not{T}}E)/\hbar, \quad (2.7)$$

which is equal to the splitting between the magnetic $m_F = \pm1$ sublevels in the $F = 1$ hyperfine level of the ground state.

A ***second pulse*** with identical parameters as the first ends the precession time by recoupling the $|x\rangle$ state with the $|0,0\rangle$ sublevel. As the $|y\rangle$ is not coupled to by the laser light, the part of the molecular wavefunction that has precessed into $|y\rangle$ remain in the $F = 1$ level. The description is now given as

$$|\psi(T+t)\rangle = \cos\left(\frac{\phi}{2}\right)|0,0\rangle - i\sin\left(\frac{\phi}{2}\right)|y\rangle\,. \quad (2.8)$$

By measuring the population of the $F = 0, 1$ states, which are experimentally distinguishable (see Section 3.4.1), the precession of the molecules is extracted and the phase difference between the states is obtained. This step is called the ***read out***. Keeping with the perfect π-pulse description, the probability of the molecules being in the different hyperfine levels of the $N = 0$ ground state are

$$P_{F=1} = |\langle y|\psi(T+t)\rangle|^2 = \sin^2\left(\frac{\phi}{2}\right), \tag{2.9}$$

and

$$P_{F=0} = |\langle 0,0|\psi(T+t)\rangle|^2 = \cos^2\left(\frac{\phi}{2}\right). \tag{2.10}$$

After the molecules exit the interaction zone, they enter a chamber in which the population of either the $F = 0$ or $F = 1$ sublevel is measured via an interaction with laser light (see Section 3.4.1).

2.2.3 Control of asymmetry of experiment

In order to extract the eEDM itself from the population measurement, the experiment must be repeated in two different conditions. By comparing the phase difference ϕ in the two conditions of electric field parallel and antiparallel to the magnetic field, the result is

$$\begin{aligned} &\phi_{\text{E,B parallel}} - \phi_{\text{E,B antiparallel}} \\ &= 2(\mu B + D^{\mathcal{P},\mathcal{T}} E)T/\hbar - 2(\mu B - D^{\mathcal{P},\mathcal{T}} E)T/\hbar \\ &= +4(D^{\mathcal{P},\mathcal{T}} E)T/\hbar. \end{aligned} \tag{2.11}$$

This means that the energy difference as given in Equation 2.2 is equal to the phase difference divided by the precession period T. Therefore by measuring $P_{F=0,1}$ in both parallel and antiparallel fields, while keeping all other systematic effects constant, the eEDM is extracted. In a calculation the symmetry of the experiment is guaranteed, with the directions of the magnetic and electric fields defined as parallel and antiparallel. The inherent nature of an experiment is such that there will always exist some non-zero angle between the two directions. It is also possible that the directions change over time in long or slow drifts, or that the magnitudes of the fields change over time, or that the magnitude of the field in one direction is different to the field when flipped. All of this must be accounted for in order to make an estimation of the possible precision and therefore the limit measured in an eEDM experiment.

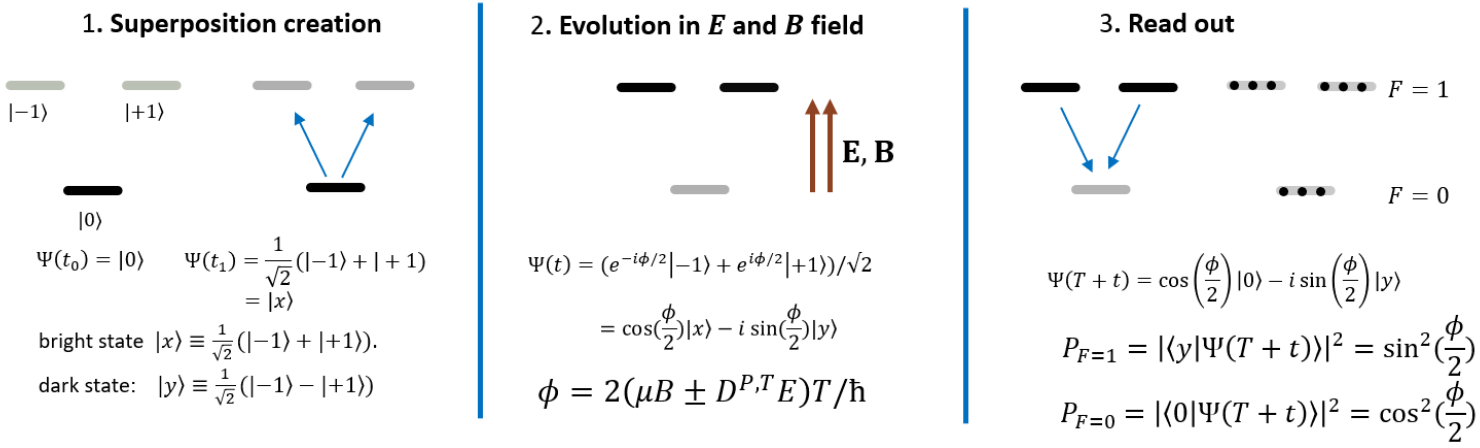

Figure 2.5: The molecules arrive having undergone ***state preparation*** and are all in $F = 0$. The ***first pulse*** arrives and creates the superposition which transfers the molecules from $F = 1$ into a superposition of the sublevels in $F = 1$. This superposition evolves in the electric and magnetic fields for a time called the ***precession period***. The superposition is collapsed by the ***second pulse*** which distributes the population of molecules across the $F = 0, 1$ states depending on the conditions during the superposition. The populations can then be measured in the ***readout*** stage. The arrows shows the transfer of population and the thick black line shows a population sate, while the thick grey line shows an unpopulated state. Complete transfers of population are assumed for the ***state preparation*** stage and the coherent state transfer into the superposition by the ***first pulse***. Figure taken from [45].

2.3 Requirements for an eEDM experiment

2.3.1 Quantum mechanical description of the molecule in E and B fields

In the NL-eEDM experiment, the BaF molecule will be used in in electric and magnetic fields. A quantum mechanical description is therefore needed in the form of an effective Hamiltonian, a basis set and a set of molecular constants. The eigenstates and energies of the molecule in a combination of magnetic and electric fields have been worked out and are discussed in Chapter 2 of [45].

The Stark shifts and Zeeman shifts that take place when a molecule is affected by magnetic or electric fields shift the energies of the quantum states and substructure. The splittings and shifts that take place in one of the fields is well understood, but the combination of two fields is the condition in which the experiment is run. The direction and magnitudes of the fields changes the splitting between the magnetic sublevels important to the experiment. The tensor Stark shift has been calculated under different magnetic field conditions.

2.3.2 Molecule production

Pulses of molecules that travel through the setup can be created in different ways with various benefits or disadvantages. The two types of molecule production methods used in the NL-eEDM experiment are cryogenic sources for SrF [41, 52] or BaF [47], and a supersonic source [41, 42].

In a cryogenic source, a cell is cooled to $\mathcal{O}(10)$ of Kelvin by flowing a pre-cooled buffer gas like helium or neon through it. Molecules are created by ablation products from a solid target mixing with elements carried by the buffer gas while in a plasma state. Collisions with the buffer gas thermalise the hot plasma, and the mixture exits the cell through an aperture in a molecular beam pulse. This technique has been used for atomic beams since 2009 [59] and was first implemented for molecule production in 2011 [60]. Cryogenic sources can produce molecules that are slower and more numerous than supersonic sources. In the NL-eEDM experiment, the cryogenic source is combined with a 4 m long travelling wave Stark Decelerator to produce a slower beam of molecules that can be probed for longer periods of time [52]. This will provide a longer coherent interaction time τ. In addition, laser cooling is currently being implemented to achieve a narrow velocity spread and increase the number of molecules that will reach the interaction zone. This combination will create a slow, cold and bright source of molecules.

While the source development is ongoing, the NL-eEDM experiment has been constructed using a supersonic source of BaF molecules [40]. Sources using supersonic expansion produce molecular beams with a small velocity spread, and relatively high population in the experimentally useful lowest energy states. As the velocity spread is small and the molecules travel at a faster velocity, the molecules stay within a small enough diameter that many molecules are interacted with via laser beams of at most a few cm diameter. Small velocity spreads are essential to maintain a high molecule number of the meter scale experiment, rather than having many losses through col-

lisions with the sides of the vacuum chambers or other internal apparatus. The supersonic source used in the experiment is discussed in detail in Section 3.1.

The supersonic source is connected to vacuum chambers with windows through which the molecules are probed using beams of laser light. These chambers are connected in series and then via a set of bellows to the interaction zone and to the rest of the experiment as is shown in Figures 2.8 and 3.9.

2.3.3 Interactions with molecules

The understanding of atomic and molecular interactions with light is a particularly well established field [61–63] which includes techniques such as absorption spectroscopy, microwave spectroscopy and Raman spectroscopy. Photons are collected using different types of photodiodes depending on the frequency of the light, and for smaller signals with low background photomultiplier tubes on single-photon counting mode are used.

In the NL-eEDM experiment, molecules are observed and measured using laser induced fluorescence (LIF). LIF is collected by photomultiplier tubes (Section 3.3.7) using single photon counting to observe the light emitted by molecules after interactions with laser light. Laser light is used to determine the frequencies of transitions, to probe populations (Section 3.4.1), and to do hyperfine and rotational optical pumping (Sections 3.4.3 and 3.4.4). In addition, the coherent state transfer is induced entirely optically (Section 2.2.2), unlike in other experiments where it is induced with direct RF fields [10, 22], or using STIRAP with beams perpendicular to the molecular beam [21, 64].

2.3.4 Control and measurement of systematic effects

In a real experiment, the two experimental conditions of the parallel and antiparallel magnetic and electric fields cannot be applied simultaneously. There will therefore be finite changes in parameters such as laser beam power and frequency, as well as the magnetic and electric field directions and magnitudes. Characterisation of these is essential to understanding the spin precession signal. It could be possible that there is a bias during one electric field direction measurement set, which would lead to an extracted signal that includes a 'false' eEDM offset. In order to characterise the changes that possible systematic biases would have on the signal, necessary parameters have been stepped or scanned rather than simply kept constant or averaged.

Our experiment is the first in the field to use laser light pulses counter-propagating to the molecular beam to induce the coherent state transfer. This provides greater control over timings and means that π pulses are applied more consistently across the all the molecules due to the to optimal timing they experience. The frequency between the two laser beams applied for the coherent state transfer is stepped in order to characterise the shape of the spin precession signal under different conditions. In this way not only the most steep part of the $\sin^2\left(\frac{\phi}{2}\right)$ curve is measured, although this is the phase with the most sensitivity to the eEDM signal.

Chapter 4 of [45] describes how the optical Bloch equations (OBE) of an eight-level system are used to model the interaction of the molecules with the laser fields under

different experimental conditions. By comparing the experimental results with the calculations, possible systematics are characterised and their effects estimated, and if necessary, accounted for. Examples of this are given in [46], and will be further developed in Chapter 5.

The essential part of the comparison with calculations and experimentally changing parameters is two-fold. Firstly, the experiment remains sensitive to the eEDM while these parameters are changed, with a loss of statistics on the order of less than 10 % as discussed in [46]. Secondly, different systematic effects create identifiable changes in the signal shape that are therefore understood on an individual level and disentangled from each other by fitting to an analytical description. We can observe, for example, changes in the magnitude of the magnetic field have a different signal shape change than that from a change of electric field. In addition, we can use the OBE description to calculate the experimental sensitivity to different parameters individually. This is also discussed in Chapter 5 of [45].

This thesis will use the calculations and conclusions found in [45] where necessary to compare and aid the understanding of the experimental results, while focusing on the process of obtaining and interpretating the signals from the experiment. The optical setup and processes are described in Chapter 3.

2.3.5 Description using optical Bloch equations

The OBE are well suited for describing a superposition within the $X^2\Sigma^+(v = 0, N = 0)$ ground state given by [†]

$$|\psi\rangle = \alpha\,|1,1\rangle + \alpha'\,|1,-1\rangle + \beta\,|1,0\rangle + \gamma\,|0,0\rangle\,, \tag{2.12}$$

where the notation $|F, m_F\rangle$ is used to describe the levels. This superposition is created using a two-photon off-resonant transition via the $A^2\Pi_{1/2}$ excited state. This description is shown in Figure 2.6.

For a perfect π-pulse, the two-photon detuning is at resonance

$$\delta = \omega_{PS} - \omega_{\mathrm{HFS}}(E) = 0, \tag{2.13}$$

and the timings and intensities of the lasers P and S are set up such that

$$\Omega_{PS} t = \pi, \tag{2.14}$$

where Ω_{PS} is the two-photon Rabi frequency, which depends on the intensity of the two laser pulses used for coherent state transfer, and t is the length of time for the applied laser pulse in both P and S. Assuming an initially empty population in $|1, \pm 1\rangle$, a π-pulse would completely transfer the population from $|0, 0\rangle$ to the superposition state ψ, with coefficients $\alpha = \alpha' = \frac{1}{\sqrt{2}}$ and $\beta = \gamma = 0$. This means that the only two states involved in the superposition are the hyperfine magnetic sublevels $F = 1, m_F = \pm 1$.

Under experimental conditions a perfect π-pulse is not realisable. By comparing experimental results to OBE calculations, individual parameters are identified which could have a systematic effects that change the conditions from a perfect π-pulse.

[†]Description adapted from [45, 46].

In the realistic general case, an incomplete population transfer will take place from $|0,0\rangle$ to $|1,\pm1\rangle$, and the magnetic sublevels $|1,0\rangle$ and $|0,0\rangle$ will have non-zero coefficients β and γ. A second pulse of laser light from P and S arrives with identical Rabi frequency Ω_{PS} and pulse length t and the spin precession phase ϕ is extracted by a measurement of the population P_i in either the $F = 0$ state or $F = 1$ state.

In the case of two perfect π-pulses, the population after the spin precession is $P_{F=1} = \sin^2\frac{\phi}{2}$. In an incomplete transfer (e.g. $\delta \neq 0$), an additional phase $\theta = \delta \cdot T$ will build up from coherence between the superposition state and the two-photon laser field, where T is the period between the start of the first pulse and the start of the second.

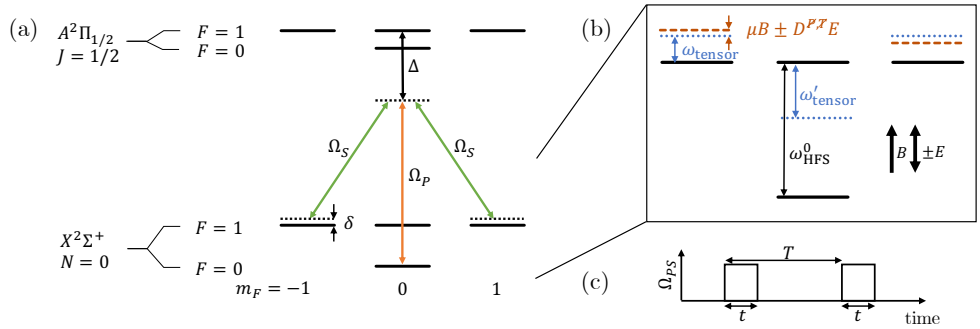

Figure 2.6: (a) The $X^2\Sigma^+(v = 0, N = 0)$ ground state and the electronically excited state $A^2\Pi_{1/2}(v = 0, J = 1/2)$ with hyperfine structure. The levels are coupled by two laser fields, labeled by Ω_S (green) and Ω_P (orange), with orthogonal polarisation, typical detuning $\Delta = 1$ GHz from the $X^2\Sigma^+ - A^2\Pi_{1/2}$ resonance, and two-photon detuning $\delta = \omega_{PS} - \omega_{\text{HFS}}(E)$ of several kHz from two-photon resonance, where $\omega_{\text{HFS}}(E) = \omega^0_{\text{HFS}} + \omega_{\text{tensor}}(E)$. (b) The $X^2\Sigma^+(v = 0, N = 0)$ sublevels of the ground state in electric and magnetic fields. The hyperfine splitting in absence of external fields ω^0_{HFS} is around 66 MHz and the tensor Stark shift for the $m_F = \pm1$ levels, $\omega_{\text{tensor}}(E)$, is around 10 kHz. The tensor Stark shift for the $m_F = 0$ level, ω'_{tensor}, is twice that of ω_{tensor} with opposite sign. The eigenstates and energies in external fields are determined by diagonalisation of an effective molecular Hamiltonian (e.g. [65]). (c) The timing sequence of the laser-light pulses with Rabi frequency Ω_{PS}, where typical pulse lengths are $t = 80$ μs and the pulse separation period is $T = 1$ ms. Energy levels and timings are not to scale. Figure and caption adapted from [46].

The population P_i depends on several independent parameters:

Detunings δ and Δ (including Doppler shifts),

Rabi frequencies for the Raman process $\Omega_{P/S}$,

Laser light polarisations $\hat{e}_{P/S}$,

Phase differences between the two laser-light pulses $\Phi_{P/S}$,

External fields $\vec{E}$ and $\vec{B}$

Lengths of the pulses t, the period between the start of the first and the second pulse T

And the initial state ρ_0.

This can be written as an equation, i.e.:

$$P_i = P_i(\delta, \Delta, \Omega_{P/S}, \hat{e}_{P/S}, \Phi_{P/S}, \vec{E}, \vec{B}, t, T, \rho_0). \tag{2.15}$$

There are eight levels involved in the OBE description (see Figure 2.6). A density matrix ρ contains this system as well as the populations P_i and the coherences. The OBE is given by

$$\frac{\partial \rho}{\partial t} = \frac{1}{i\hbar}[H(t), \rho] + L_{\text{relax}}(\rho), \tag{2.16}$$

so that P_i can be obtained, where $H(t)$ is the Hamiltonian includes the Zeeman and Stark effects and couplings with the laser fields. Spontaneous decay to the ground state is included via L_{relax} as well as losses to other levels other than the 8 involved in the description. This equation is constructed and solved in MATLAB as a function of the parameters in Equation 2.15 as a numerical solution. Incoherent effects, light shifts, the hyperfine levels and imperfect polarisation of laser light have been included in the description.

2.3.6 Magnetic fields

In order to optimise the Zeeman splitting between the $m_F = \pm 1$ sublevels, the magnetic field needs to be small ($\mathcal{O}(nT)$), stable in time, and spatially homogeneous. The magnetic field inside the shield is created such that the phase build up is $\phi = 2\mu|B|T/\hbar = \pi/2$ in order to maximise the eEDM sensitivity. To do this we have built a magnetic shield [18] with five layers of μ-metal to create a homogeneous field region for the molecules to traverse, see Figure 2.7. The innermost μ-metal layer has a length of 130 cm and a diameter of 50 cm. Within and coaxial to this cylinder, a newly developed double cosine Θ coil (length 100 cm, diameter 30 cm) has been designed, which generates a $B_x = \mathcal{O}(10\text{ nT})$ with 2 % relative precision in space. With the used power supplies, the fields generated by the double cosine coil achieve better than pT resolution. The double cosine coil permits an order of magnitude higher and therefore easier to control currents than for a single cosine coil. In addition, a double coil has no wires across the beam.

The external compensation coils and shield together are designed to reduce the earth's magnetic field of $|B|_{\text{earth}} \approx 70$ μT by six orders of magnitude to $|B|_{\text{shielded}} = 70$ pT. Time variation from the outside of the shield in comparison to the inside is reduced by six orders of magnitude, with a relative time variation of $< 10^{-4}$. At a working point of 10 nT, this relative time variation corresponds to 1 pT [18].

The magnitude of the fields is not the only consideration of the magnetic fields for the NL-eEDM experiment. The orientation of the electric and magnetic fields changes the transitions that can be made. This will be discussed in Section 5.1.2.

2.3.7 Electric fields

The eEDM is enhanced in an electric field as discussed in Section 2.1.1. An electric field that is several orders of magnitude larger than the fields used in our experiment does not improve the precision available as this enhancement does not increase linearly with electric field. Therefore a field must be chosen that is experimentally possible to create homogeneously and reliably in a lab environment, which gives enough precision for a useful eEDM-limit extraction.

Within the innermost cylinder of the magnetic shield a cylindrical glass vacuum chamber with a pressure below 10^{-7} mbar has been installed [18]. It contained two parallel indium tin oxide (ITO)-coated glass plates which are separated by 4 cm. Each plate has a length of 75 cm and width of 10 cm. They are mounted vertically such that an electric field E is (anti-)parallel to the magnetic field B within the shield, which is in the $\hat{x}$-direction. Electric fields have been applied up to $E = 5$ kV/cm with a homogeneity of $\Delta E/E < 10^{-4}$.

2.3.8 Interaction zone

The region where the molecules are probed in a homogeneous combination of electric and magnetic fields is called the Interaction Zone. The dimensions of the fiducial volume are a length of 50 cm and diameter of 4 cm. The entire setup of the Interaction Zone is shown in Figure 2.7.

2.3.9 Experimental setup

The setup of the first stage of the NL-eEDM collaboration is shown in Figure 2.8, along with the region labels A-D that are used throughout the text of this thesis. BaF molecules created by a supersonic source [40] in Region A travel towards Region D. The molecular pulse undergoes rotational optical pumping and hyperfine state preparation in Region B before arriving in the electric field interaction zone which is located inside a 5-layer mumetal magnetic shield in Region C. The molecules interact with laser beams that counterpropagate with the molecular beam direction within the interaction zone. Finally the molecules exit the interaction zone and are detected using laser induced fluorescence in Region D.

The setup shown as parts A-D in Figure 2.8 is not the only experimental setup. The many laser frequencies and beams involved in the experiment at different points along the molecular pulse's timing are essential. The lasers and optical devices are

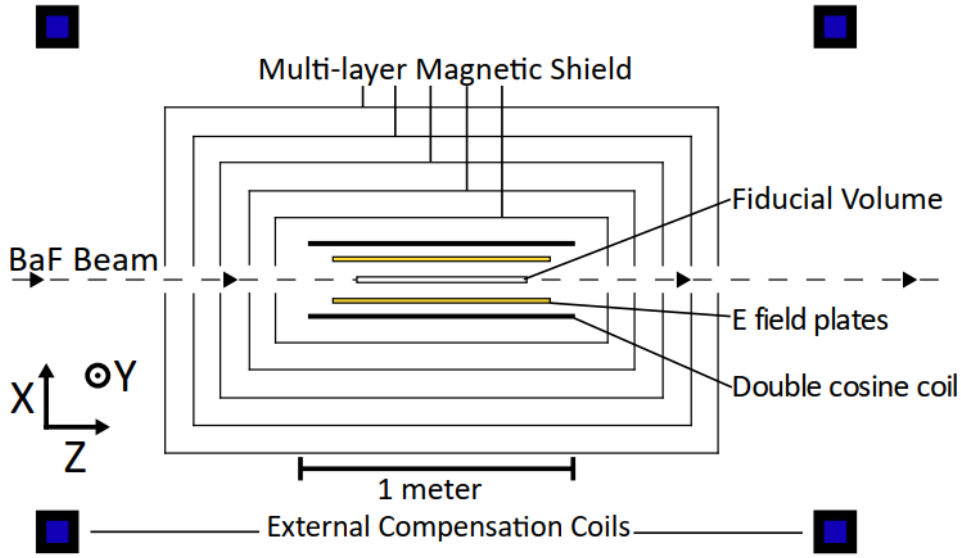

Figure 2.7: Interaction zone: an environment with electric and magnetic fields for eEDM sensitive searches. Figure and caption from [18].

detailed in Sections 3.2 and 3.3. The laser frequencies are controlled by a wavelength meter, discussed in Section 3.3.6. All timings and measurements are collected in the combined DAQ system which is discussed in Section 3.4.6.

2.3.10 Data acquisition

The requirements in the experiment are that any device that takes data is connected into a single data stream. A tree file using Cern's ROOT code package [66] has been implemented and the data treatment works synchronously at the 10 Hz rate of the experiment. This value is only limited by the rate achievable for the supersonic source, rather than electronics of the data acquisition system itself. We have tested at rates of up to 40 Hz but operate at 10 Hz for ideal stability of the source. Devices are synchronised such that different data types from different devices are combined.

More technical specifics are given in Section 3.4.6 and a detailed description of the data acquisition system (DAQ) is found in [44].

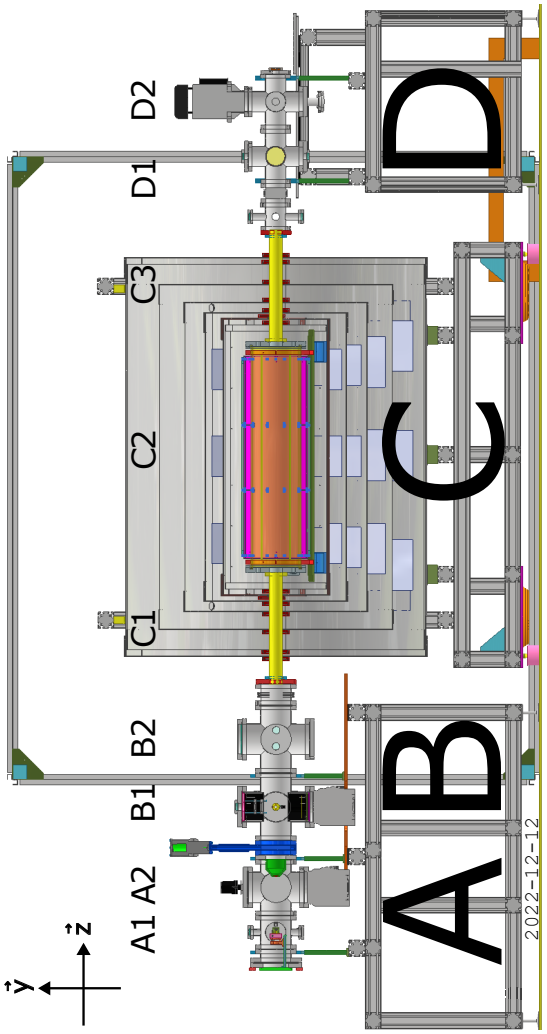

Figure 2.8: Conceptual setup diagram showing a side view of the NL-eEDM experiment, with the magnetic shield cut out to see the layers of mu-metal and the interaction zone. The regions of the experiment are labelled with letters A-D. A: ablation takes place at A1 and the supersonic source creates pulses of BaF molecules and Ba atoms which travel from left to right through the setup. B: At B1 the molecule number is probed for normalisation. B2 has two optical windows. In the first window, the molecules undergo hyperfine state preparation. In the second, the Ba atoms from the source are probed to test wavelength meter drift. C: At C1 the molecules enter the magnetic shield. C2 is called the interaction zone, where well controlled electric and magnetic fields are applied. In this region, two laser pulses arrive and interact with the molecules. These laser pulses enter the experiment from a vacuum window at Region D and counter-propagate against the molecular pulse velocity. The final population distribution is probed in Region D. The coordinate system is shown in the top left. The figure has a perspective taken from the $-\vec{x}$ direction. Figure taken from [18].

2.4 The BaF molecule

While in Section 2.1 the use of BaF as a candidate in an eEDM search was discussed, here the structure of the $^{138}Ba^{19}F$ molecule is investigated with a focus on the particular energy levels that are relevant for an eEDM experiment. A recent description of the understanding of the molecular structure of BaF is given in [41], so only the essential points relevant for the understanding of this thesis will be summarised here.

The ground electronic state is $X^2\Sigma^+$, the neglected first excited state is $^2\Delta$, and the second excited state is $A^2\Pi$. Only the first and last states are relevant to experiment, and will be given in more detail in the next sections.

2.4.1 The ground $X^2\Sigma^+$ state

The ground $X^2\Sigma^+(v = 0, N = 0, F = 1)$ state is made up of vibrational v levels and within these, rotational N levels starting from $N = 0$. The frequency splittings for these substructures are around 10 THz for vibrational splittings, 10s of GHz for rotational splittings, and $\approx$ 100 MHz for hyperfine splittings. Each N level has two $J = N \pm 1/2$ levels, with the exception of the $N = 0$ which has only $J = 1/2$. Each J level has a hyperfine structure given by two $F = J \pm 1/2$ levels. The rotational and hyperfine structure is shown graphically in Figure 2.9. These F levels have Zeeman sublevels with multiplicity $2F + 1$, which are degenerate without applied magnetic fields. The lowest vibrational levels and rotational levels are of most interest to the experiment.

On the right of Figure 2.9, the hyperfine splitting of the $X^2\Sigma^+(v = 0, N = 0)$ is shown with the two $F = 0, 1$ levels. The spin precession sequence of the eEDM experiment takes place within the substructure of the $F = 1$ level. There are three sublevels $m_F = 0, \pm 1$ within $F = 1$ that in a magnetic field undergo a Zeeman shift.

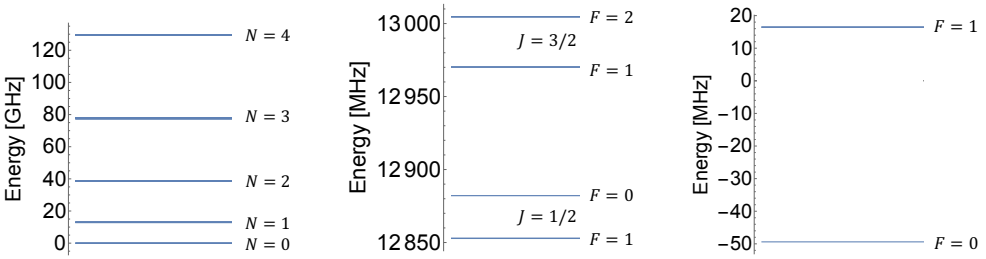

Figure 2.9: Left: The rotational structure of the ground $X^2\Sigma^+$ state for the lowest vibrational level $v = 0$. Middle: The internal hyperfine structure of the $N = 1$ rotational level. Right: The internal hyperfine structure of the $N = 0$ rotational level. Figures from [45].

2.4.2 The excited $A^2\Pi$ state

The excited $A^2\Pi$ state has additional fine structure states due to the non zero spin-orbit interaction. Therefore there exists energy levels $A^2\Pi_{1/2}$ and $A^2\Pi_{3/2}$. These have vibrational structure v with $\mathcal{O}(10\text{ THz})$ splitting and rotational structure J with $\mathcal{O}(10\text{ GHz})$ splitting. In addition, Λ-doubling (which takes place due to an interaction of the angular momenta from the nuclei rotation and electron orbitals) for these states means that each J rotational level has two states with opposite parity. For the $A^2\Pi_{1/2}$ excited state these parity levels are split for low J by $\mathcal{O}(100\text{s MHz})$, whereas for the $A^2\Pi_{3/2}$ state, low J parity levels are only split by $\mathcal{O}(10\text{ kHz})$. The rotational levels also have hyperfine substructure which decreases in frequency for higher J, starting from 10s of MHz.

The lifetimes of the two $A^2\Pi$ excited states were measured [42] to be $\tau = 57.1(3)$ ns for $A^2\Pi_{1/2}$, and $\tau = 47.9(6)$ ns for $A^2\Pi_{3/2}$. This discussion is additionally given in Chapter 4 in Parul Aggarwal's thesis [41].

2.4.3 Transitions used in the *e*EDM experiment

In the eEDM experiment, specific transitions are used and therefore those energy levels must be investigated. The transition linewidths, frequencies and hyperfine structure of both ground and excited states must be known to between $\mathcal{O}(\text{MHz})$ and $\mathcal{O}(\text{Hz})$ precision.

Before the interaction zone, the molecules undergo optical pumping out of the $X^2\Sigma^+(v = 0, N = 0, F = 1, +)$ state via the $A^2\Pi_{1/2}(v = 0, J = 1/2, F = 1, -)$ excited state. The population of the $X^2\Sigma^+(v = 0, N = 0, F = 1, +)$ state is probed via the $A^2\Pi_{3/2}(v = 0, J = 3/2, F = 1, -)$ excited state. This takes place after the spin precession in the interaction zone.

Normalisation of the number of molecules is implemented by probing one of the ground $X^2\Sigma^+(v = 0, N = 1, 3, 5)$ sublevels that are highly populated, via a sublevel of the $A^2\Pi_{3/2}(v = 0)$ excited state. Transitions from these ground states are used as they do not have any decay from the excited state to the even N ground states used in the eEDM experiment due to the parity selection rules.

Additional optical pumping is implemented from the $X^2\Sigma^+(v = 0, N = 2)$ state before the interaction zone in order to increase the population in the $X^2\Sigma^+(v = 0, N = 0)$ ground state. This takes place before the molecules undergo the hyperfine pumping.

The $X^2\Sigma^+ \rightarrow A^2\Pi_{1/2}$ transition has a longer wavelength ($\approx$ 860 nm) than the $X^2\Sigma^+ \rightarrow A^2\Pi_{3/2}$ transition ($\approx$ 815 nm). This means that when detecting fluorescence light at these frequencies, higher quantum detection efficiencies are achieved for light using the $X^2\Sigma^+ \rightarrow A^2\Pi_{3/2}$ transition due to the technology of photomultiplier tubes (PMTs), see Section 3.3.7. Both transitions are required for different functions in the experiment (see Sections 3.4.1 to 3.4.5).

2.5 Conclusion

In the precision measurements field, many theories expanding or extending the standard model of particle physics can be restricted by measurement of particular parameters. For these parameters, such as the eEDM, a suitable system gives enhancement factors that mean that measurement can be many orders of magnitude more precise. In addition, studying multiple complementary systems with different methodologies means that each investigation will have independent systematic effects and possibly different theoretical parameters that mean the theoretical eEDM value can be further restricted, even if additional measurements do not restrict the value of the eEDM itself. In the NL-eEDM collaboration, the focus is on measurements using the BaF molecule as part of this series of independent measurements that can be combined to ascertain which theories can be limited or restricted.

We have developed a strategy to obtain an eEDM measurement, and built a working experimental setup that can measure and identify various possible systematic effects that could otherwise lead to a 'false' eEDM measurement. The requirements of the basic setup of the experiment has been described with details of the molecule production, the interaction of molecules with laser light, and the data acquisition process. A differential measurement method is taken such that the eEDM value is the only value that is not cancelled out between two electric field orientations that we switch between, if all other parameters are kept constant.

In order to keep the other parameters as close to constant as possible, we have designed an interaction zone where the magnetic and electric fields are kept constant. In addition, by varying some parameters and comparing to calculations with the OBE, changes in the data during experimental runs are quantified in order to reduce potential systematic effects.

Chapter 3

Optics and experimental Setup for an eEDM experiment

A sensitive eEDM experiment using molecules crucially depends on careful control of the populations of various molecular states throughout the entirety of the measurement. The particular transitions of interest must therefore be understood to a precision that matches the experimental requirements, including their hyperfine structure and their behaviour in external electric and magnetic fields. In order to investigate this to a sufficient accuracy, spectroscopy has been undertaken and is shown in Chapter 4.

Here we describe the systems that have been designed and set up to measure an eEDM. This includes the production of molecules, the optical systems created to control and measure the molecules, and the results of these processes. The essence of the information presented here is that this is not a list of tools or devices, but describes the essential steps of the experiment and the correspondingly measured results.

The molecular pulses created in the supersonic source travel through the vacuum system of the experiment. A diverse laser system is required for such an experiment to address particular states for objectives such as spectroscopy and identification of states, optical pumping and population probing. A potential eEDM signal is extracted by inducing spin precession of the molecules and its detection. In our eEDM experiment, the observation of spin precession is achieved by entirely optical methods using laser light pulses within a wavelength range extending from $815 - 860$ nm.

Multiple laser systems have been set up, encompassing different frequency ranges that are required for the experiment. Here we will discuss the various systems, their uses, and identifications. In addition, the optical devices employed across the experiment are described. Their functions include laser light transportation, pulse creation, and laser induced fluorescence collection. The polarisation, power and wavelengths of the laser light used in the experiment are controlled and the methods behind these are discussed. The laser light is created in a dedicated shielded and temperature controlled laboratory called the "Laser Lab", and transported via optical fibres, of typical length 20 m, to the molecular beam in the "EDM Lab". *

*The Laser Lab is a temperature and access controlled separated room in the building adjacent

The crucial experimental functions employed to obtain spectroscopy and spin precession information are described, with an explanation of the normalisation and background removal signal process employed. Optical setup diagrams showing how each of the crucial steps are implemented are shown. In addition, the data acquisition requirements and processes are reported. The timings employed in this pulsed experiment are discussed.

For a sensitive experiment, optical pumping is required before the molecules arrive in the interaction zone, including rotational population transfer for a signal increase as well as hyperfine state cleanup. The method and results of this are shown. Furthermore, laser pulses are required in the experiment with very high timing precision. The methods used to convert CW laser beams to custom pulse patterns are also described.

3.1 Production of molecules in a supersonic source

The BaF molecules are produced in a supersonic source, which has been characterised and described in great detail [40, 41]. The source uses a rotating 3 mm wide Ba target. A jet of Ba atoms is sputtered off the wheel's surface and the atoms are seeded into a carrier gas of 2% SF_6 and 98% argon. The source creates BaF molecules along with a variety of other systems such as different isotopes. A pulsed beam is achieved by an Even-Lavie valve with a time gate of ≈ 35 μs operated at an adjustable backing pressure (used at between 2-20 bar). The source has a variable repetition rate set to 10 Hz and a rotational temperature of 3.5 K. The molecules fly through the setup at a velocity of 610(4) m/s, with a velocity spread of 32.9(2) m/s at 8 bar backing pressure, giving a relative translational velocity spread of $\Delta v/v = 0.054(9)$ and a translational temperature of 5.2(1) K. The time variance of the TOF of the beam at 8 bar is 51.2(4) μs [40, 41]. In recent experiments, repetition rates of up to 40 Hz were tested and best source stability was found in 10 Hz.

The molecular beam pulse passes through a skimmer (diameter 5 mm) 28 cm after the exit of the Even-Lavie valve, in order to enabled differential pumping for achieving a background pressure of $<$ mbar downstream. The central part of the produced BaF beam is exploited by the experiment. The source has been measured to produce 6×10^8 BaF molecules per pulse per steradian in the $X^2\Sigma^+(v = 0, N = 1)$ state [40].

The supersonic source has now been connected to the rest of the NL-eEDM setup as shown in Figure 2.8. In the combined configuration, certain settings of the supersonic source such as target position, backing pressure and laser ablation position have been optimised in order to maximise and stabilise the number of molecules that travel in a pulse through the whole experiment. For example, the backing pressure used is generally around $1 - 2$ bar rather than 8 bar, and therefore the parameters such as rotational temperature as well as velocity/ velocity spread are slightly different.

The ablation process of the supersonic source means that the inside of the vacuum chamber before the skimmer becomes coated with opaque debris, including the window through which the ablation laser light enters. As the experiment is run for a long time, the window eventually significantly reduces the ablation power that can pass into the vacuum chamber, and consequently the number of molecules produced

to the also temperature and access controlled NL-eEDM laboratory "EDM Lab".

and signal achieved reduces. To combat this, a new valve was attached that means that the vacuum window is internally blocked except for the part that the laser light passes through, and the window can be easily rotated to access new sections that are not coated in the debris.

3.1.1 Velocity of BaF molecules

The effect that pressure has on the velocity of the molecules is seen in Figures 3.1(a), 3.1(b) and 3.2. The backing pressure was manually changed to different values with a needle valve. The measurement order was taken as follows: 4, 8, 15, 2 and finally 4 bar again. At each backing pressure, the molecules were probed using laser induced fluorescence at two different locations B1 and D1. The positions are measured to be 640(10) mm and 3820(10) mm respectively from the gas nozzle that the gas is released from the valve at the supersonic source.

The fluorescence is collected by photomultiplier tubes (PMTs) and sent to an oscilloscope from which the centre of the peak was read off. The setups for laser induced fluorescence are discussed in Section 3.4.1 and Section 3.4.2. This data is also recorded in the data acquisition for use in situations where the velocity or timing is specifically required to be known to greater precision.

Figure 3.1(a) shows the arrival time measurements for location B1, while the arrival time measurements for D1 are shown in Figure 3.1(b). The differences between these plots are taken and then the measured distance difference (3180(14) mm) is divded by the time differences to find the molecular velocity. These are shown for the different backing pressures in Figure 3.2. The amplitude and shape of the TOF of the molecules also changes for different backing pressures, which cannot be seen in these plot. This is recorded in the DAQ.

The errors in the velocity α_{velocity} are propagated by

$$\alpha_{\text{velocity}} = \sqrt{(\frac{\alpha_{\Delta T}}{\Delta T})^2 + (\frac{\alpha_{\Delta d}}{\Delta d})^2}, \tag{3.1}$$

where the uncertainty on the time difference ($\alpha_{\Delta t}$) is given by

$$\alpha_{\Delta T} = \sqrt{\alpha_{T_{B1}}^2 + \alpha_{T_{D1}}^2}, \tag{3.2}$$

where T_{B1} and T_{D1} are the arrival times measured at positions B1 and D1 respectively. The uncertainty for the distance difference ($\alpha_{\Delta d}$) is given by

$$\alpha_{\Delta d} = \sqrt{(\alpha_{d_{B1}})^2 + (\alpha_{D_{d1}})^2}, \tag{3.3}$$

where $\alpha_{d_{B1}}$ and α_{d_D1} are the uncertainties of the distance measured for positions B1 and D1 respectively.

If the pressure of the experiment changes during an eEDM measurement run, we would therefore observe this as a change in velocity of the molecules. We constantly monitor the TOF of the molecules during experiments using a gating system set around the

arrival time at Region D of the apparatus. This is further discussed in Section 3.4.1. If the TOF is shifted so much that the gate timings mean that some or all of the laser induced fluorescence is missed by the DAQ, this would read in the experiment as a reduction in signal that could otherwise be attributed to a false eEDM. Instead, this is measured and is reconstructed by observing the velocity of the molecules from their TOF.

In addition, observations show that the number of collected photons and therefore the number of molecules does not change significantly with a change of backing pressure, in conditions of more than 1 bar.

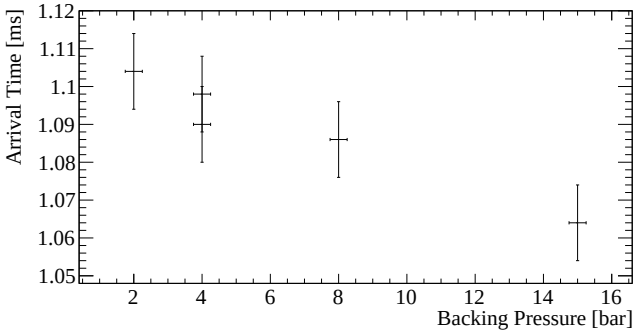

(a) Position B1

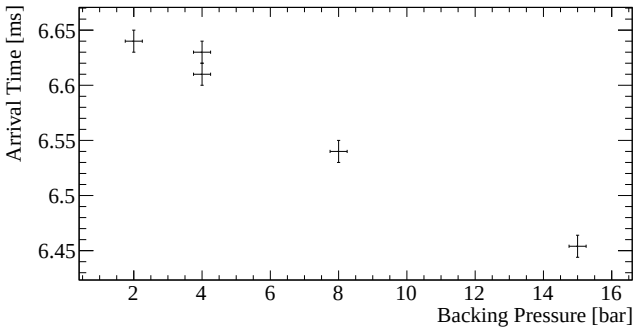

(b) Position D1

Figure 3.1: The arrival time of BaF molecules from the supersonic source at positions B1 and D1 under different backing pressures. The arrival times get shorter for higher backing pressures as the velocity of the molecules increases. The arrival time was measured twice for the backing pressure of 4 bar. Data taken 16th June 2023. The arrival time values at B1 are smaller than at D1 and the plots do not cross the origin, so the error bars on the arrival time axis appear to be larger although they are identical and come from the uncertainty in measurement.

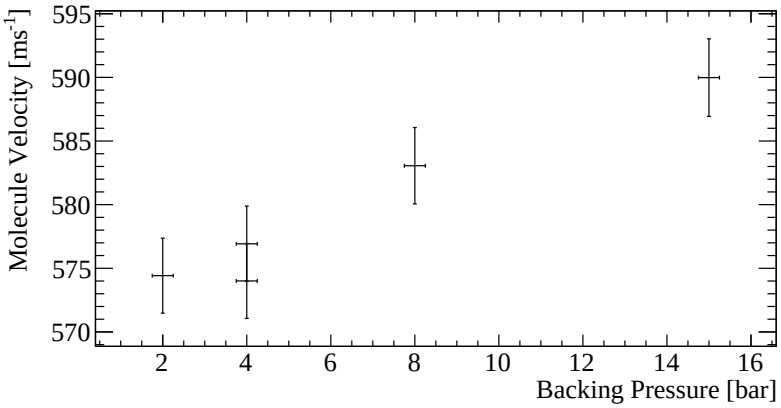

Figure 3.2: Molecular velocity versus time from the data shown in Figures 3.1(a) and 3.1(b). Higher backing pressures give a larger molecular velocity. The molecular velocity at 4 bar was measured twice and the results agree within their uncertainties. The propagation of the error bars for the velocity measurement is discussed in the text.

3.1.2 Width of molecular beam

In Figure 3.3, the diameter of the molecular beam at different interaction points of the experiment is shown. The origin point of the experiment is fixed as the exit of the gas nozzle, and the angle θ that is formed downstream between this and the edges of the 5 mm wide circular skimmer, 280 mm away, which is calculated by

$$\theta = \arctan\left(\frac{5\text{ mm}/2}{280\text{ mm}}\right). \tag{3.4}$$

This angle is used to calculate the beam's width at other distances along the experiment's z-axis where the distance is measured to the nearest cm. This is the case for the positions B1 and B2, where laser beams enter the vacuum chamber through a window to interact with the molecules.

Positions C_α and C_β are defined as the position of the molecular beam pulse at the beginning of the two laser pulses. One intersects with the molecules when they are at the beginning of the homogeneous electric and magnetic field region in the interaction zone, and one intersects at the end. The timings are 3.3 ms and 4.3 ms after the laser ablation. Using a molecular beam velocity of 576 ms^{-1}, the diameter at positions C_α and C_β are calculated in the same way as at B1 and B2.

The beam passes through various vacuum chambers including a glass tube with an internal diameter of 232 mm, which is wider than the molecular beam at all points so does not cut off any of the molecules from passing through. The electric field plates are 400 mm apart and are centred around the middle of the interaction zone. In Thomas Meijknecht's thesis [18], there is a discussion of the beginning and end points of homogeneous electric field conditions, and this is what is relevant in the eEDM experiment. The mapping of the electric field conditions enables the determination

of the location of the field plates.

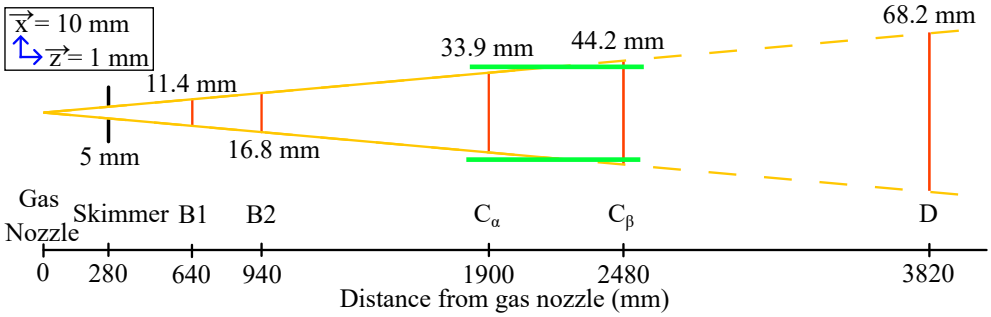

Figure 3.3: Diagram showing the geometric maximum possible width of the molecular beam at the interaction points of the experiment. The beam widths are all calculated using an angle of θ (see Equation 3.4) from the gas nozzle and assuming the molecular beam begins with a constant velocity from the end of the nozzle. The distances are all measured to the nearest cm. The distances for the positions C_α and C_β are calculated using a beam velocity of 576 ms^{-1} and arrival times of 3.3 and 4.3 ms respectively. Along the bottom is a number scale with each position from the gas nozzle exit given in mm. The 5 mm diameter circular skimmer is shown as the two thicker black lines. The molecular beam is shown in yellow and the diameter at each interaction position is shown along with a red line within the beam. The electric field plates are shown as the thick green lines. They are 4 cm apart, which is smaller than the calculated diameter of the beam at position C_β, which means that some of the molecules will be cut off. The diameter given at position D is assuming no molecules are lost, and is larger than the real diameter of the molecular beam. The diagram is to scale with the scales shown by the blue arrows in the top left corner. The $\vec{x}$ axis of the experiment is 10× more zoomed in than the $\vec{z}$ axis for plotting purposes.

3.2 Laser systems

Multiple optical frequencies are required in our experiment. Therefore, various different laser systems are used to fulfill the necessary roles and tasks. A variety of powers, frequencies and stabilities are required. In general we have MHz linewidth requirements. All lasers used in this experiment are continuous wave, and pulses are created using pulse-shaping optics such as acousto-optical modulators and appropriate driving electronic pulses, after the light has been emitted from the laser.

A summary of the lasers used in the experiment and their individual uses in the apparatus and their utilised wavelengths is given in Table 3.1. The name used is the actual name used in the DAQ system to identify the frequencies measured by the wavelength meter.

Name	**Function**	λ **(nm)**	**Brand and type**
Freq1	Normalisation	815	Coherent MBR 110 Ti:Sa
Freq2	Hyperfine pumping	860	ECDL (Thorlabs)
Freq3	Rotational pumping	860	Coherent MBR 110 Ti:Sa
Freq4	Population probing at D	815	Toptica DL-Pro Diode
Freq5	Superposition pulses	860	Toptica Amplified Diode
Freq7	Ba spectroscopy	795	Home-built Diode

Table 3.1: Table showing the frequency identifiers of the individual lasers used in the experiment along with their uses in the eEDM experiment. Information about the laser type and their typical wavelength range is also given. ECDL stands for external cavity diode laser.

3.2.1 Titanium Sapphire lasers

Tuneable over $650 - 1100$ nm, Titanium Sapphire (Ti:Sa) lasers are very well-suited for use in spectroscopy to find, identify and measure different states of atoms and molecules. The power of the laser light directly out of the laser head is typically $200 - 500$ mW. The typical stability of the locked laser over time is shown in Figure 3.4(a), where the plot has a standard deviation of 2.63 MHz.

The experiment employs the use of two Ti:Sa lasers with different frequency ranges to drive transitions from the $X^2\Sigma^+$ ground state to both the $A^2\Pi_{1/2}$ (Freq3) and $A^2\Pi_{3/2}$ excited states (Freq1). Freq1 is pumped by light from a Sprout-G laser and is made up of a MBR 110 Coherent Laser Group/ Microlaser Optical Systems laser box and a MBR E-110 Control box. Freq3 uses the same type of Ti:Sa laser head and control box, and is pumped using light from a Coherent 0178-281-50 10W Verdi-v10 Ddps Diode Pumped Solid State Laser.

Both lasers are used for spectroscopy to extract the hyperfine structure for lower lying ground and excited states of BaF, as well as identifying frequencies for particular states (see Chapter 4).

3.2.2 Diode lasers

Both homebuilt and commercial diode lasers are used in the experiment for different uses. The home built diode lasers are tuneable over a range of a few hundred MHz, and provides light with power of mW. These are used for hyperfine pumping (Freq2) and doing spectroscopy of Ba atoms when necessary.

The frequency of one of the home-built diode lasers which is used for the hyperfine pumping out of the $(N = 0, F = 1)$ sublevel of the ground state is plotted versus time while being locked to the wavelength meter (see Section 3.3.6) for 5 hours. This data is plotted versus time in Figure 3.4(b). The standard deviation of the histogram is 1.11 MHz.

Another diode laser used in the experiment is a commercially available Toptica DL-Pro laser at 815 nm with 60 mW power (Freq4). It is used for the final population probe after the spin precession has taken place. Similar plots to Figure 3.4(b) for Freq4 are shown in the context of the wavelength meter locking in Figures 3.5 to 3.7. The standard deviation of this laser frequency locked for the same five hours is 0.24 MHz.

3.2.3 Diode lasers amplified

For higher power ($>$ 1 W) uses, the Toptica Photonics Amplified Tunable Single-Mode Laser System (780 - 940 nm) laser is used. The laser control boxes include voltage outputs that are used for external uses or for a power amplifier within the laser.

The power amplified diode laser with a frequency defined in the data acquisition as Freq5 is used to setup and readout the spin precession of the molecules within the interaction zone. The laser itself is continuous wave in output, but its output is pulsed using acousto-optical modulators as is described in Section 3.4.5.

The locked laser frequency versus time is plotted in Figure 3.4(c) and has a standard deviation is 186 kHz. This is significantly smaller than the home built diode (shown in (b)) and the Ti:Sa (shown in (a)). At approximately 2.5 hours, the doors to the laser lab were opened repeatedly and noise from people walking around the using the lab is measured. The lasers relocked themselves very quickly (within 2 s), and the measurement allows for a simple data cut to be applied.

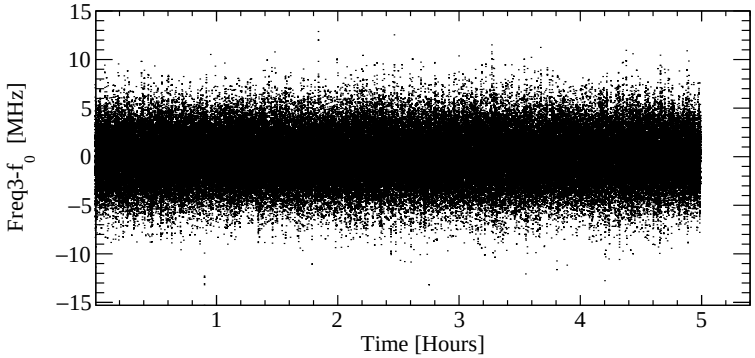

(a) Frequency Freq3 from a Titanium Sapphire laser versus time, offset by $f_0 = 348.627727$ THz. The standard deviation is 2.63 MHz.

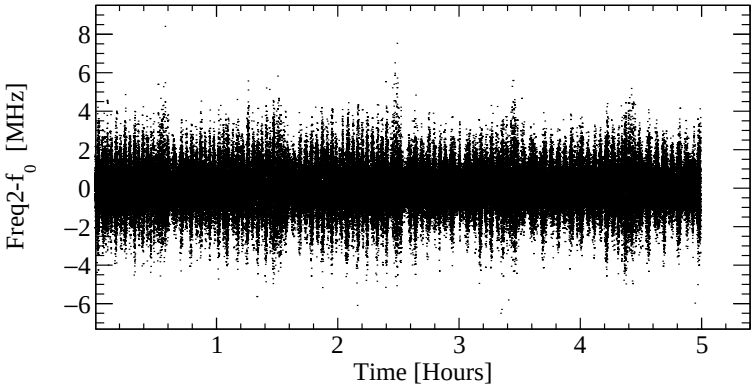

(b) Frequency Freq2 from a home-built diode laser versus time, offset by $f_0 = 348.666429$ THz. The standard deviation is 1.11 MHz.

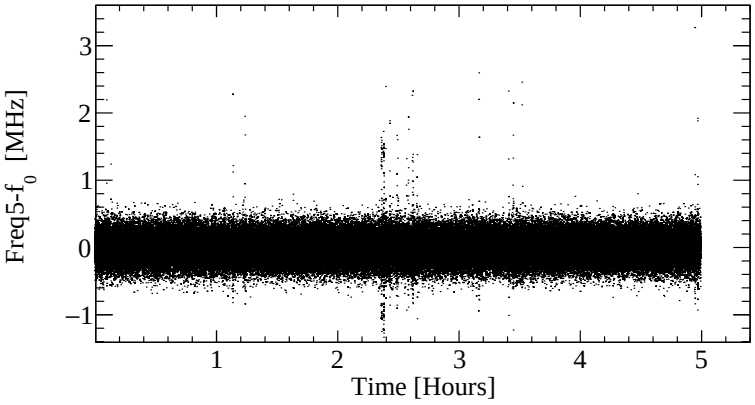

(c) Frequency Freq5 from an amplified Toptica Diode laser versus time, offset by $f_0 = 348.665043$ THz. The standard deviation of the data is 186 kHz.

Figure 3.4: Frequencies of different lasers locked and measured by the same wavelength meter in parallel and collected in a single datastream (See Section 3.3.6) for 5 hours on the 25th of June 2022. The observed spikes at for example around 2.5 hours are due to the door to the lab being opened and the lasers relocking. Each plot has a different frequency scale.

3.3 Optical tools and devices

Various optical devices to create, split and frequency control laser light are utilised to provide the optical signals required in the experiment. Light from the laser induced fluorescence is collected and measured, as well as the power of laser beams themselves and their frequencies.

3.3.1 Optical fibres

It is not necessary to create laser light physically next to the experiment. By sending light through optical fibres to the experiment, the geometry of the experiment can easily be kept the same while different laser frequencies are sent through the fibres. This also means that parts of the experiment are developed or varied in a different room to sensitive equipment such as the magnetic shield, reducing sources of noise and possible systematic effects.

Single mode optical fibres have been installed to connect the two labs, through which laser light is transmitted with negligible intensity losses over a distance of 10s of meters. Fibre launchers (Thorlabs Aspheric FibrePort Collimators PAF2-5B/7B) are used to send light in and out of fibres. A series of mirrors directs free space laser light into the fibre launchers, and lenses are used to correct the beam width and to ensure a collimated beam enters the fibre. In this way the intensity of the beam that exits that fibre is maximised. The insertion losses of laser light depends on the mode of the laser light. If the light is a Gaussian mode, up to $\approx 80\%$ transmission through the fibre is expected. This transmission is much less for laser light that is non Gaussian, such as that from some laser diodes.

Light power is lost in an optical fibre at around $\mathcal{O}(1$ dB per km). Typical fibre lengths used in our labs (up to 20 m) are not long enough to have significant power losses. We see excellent stability with these optical fibre setups.

3.3.2 Polarisation control

Polarisation maintaining single mode optical fibres are widely commercially available. These have the benefit of outputting the same polarisation of light that is input, as long as the light is aligned with their birefringent axes. However, this means that if the polarisation of the input light changes or if a fibre is physically moved or twisted, the output power of the fibre can change too. In our experiment we have found best results when controlling the polarisation of light after delivery with an non-polarisation maintaining optical fibre.

The polarisation of light exiting a non-polarisation maintaining single mode optical fibre is controlled manually by inducing stress on the fibre via a gentle twist. Devices are commercially available which work by squeezing an optical fibre with a series of paddles, such as FiberControl's manual fibre polarisation controller FPC-3. These devices allow maximisation of a desired polarisation outputting the fibre, which can then be used in an experiment.

The polarisation of free space light is controlled using waveplates (which rotate the polarisation of light), polarisers (that only permits light with a certain frequency com-

ponent through) and polarising beam splitters, which split light into two orthogonal frequency components. Such optical pieces have a dependency on the input angle, wavelength of the light, and the ambient temperature of the lab.

Dielectric mirrors affect the polarisation of light, so gold or silver plated mirrors are used at points for which the polarisation is required to be stable and controlled. Optical windows also have birefringency under stress, for example when installed in a vacuum system. In our experiment this remains constant when reversing the electric field direction, and so will not have an effect on a potential eEDM result.

3.3.3 Fibre splitters and combiners

Laser light is manipulated in both free space and while it is travelling within an optical fibre. Optical fibre splitters and combiners are used to overlap multiple laser light sources, or laser light is split into specific power ratios. Such devices are widely commerically available and are used for robustly overlapping and splitting laser light beams that are already travelling within optical fibres.

3.3.4 Fibre coupled attenuators

For additional power control, we can attenuate the power of a laser beam while it is travelling within an optical fibre. A voltage is applied which dictates the stress (and hence birefringence) applied to the fibre and therefore attenuation, which may not be a linear process. Thorlabs 780-980 nm 780HP Fiber Attenuators are connected to the voltage outputs from laser controller boxes. Increasing the voltage applied means more attenuation of the power of the laser beam. We see good stability in power by using these devices.

3.3.5 Acousto-optical modulation

Fine frequency offset control is often required, as well as the ability to block the beam going to the experiment. This is achieved with great flexibility by using acousto-optical modulators (AOMs, IntraAction). In addition, the power of the beam is controlled by changing the power provided to the AOM device.

These devices take an RF electrical input and convert it into an acoustic wave that travels through a transparent material (usually crystal or glass). This standing wave interacts with a laser light beam passing through the material, and splits the power of the beam into the original (the 0th order) and additional nth order beams that exit the crystal at angles that depend on the frequency of the RF input. Each nth order beam has an angle which is an integer multiple of the deflection of the first order. The distribution of power among the different diffracted orders depend on the angle of the material and the power of the applied RF input. The spatial separation means that nth order beams are independently used, rather than having to work with them in addition to the 0th order beam. The underlying physics principle is the addition of the momentum of the optical and RF phonons.

Splitting a light beam from a single laser into components that enter different AOMs, and then recombining their 1st order beams while blocking the 0th order beams

means that customisable frequency and power control is achieved, for example MHz level frequency differences are achieved to address typical hyperfine splittings seen in the molecule. This process is utilised in the production of the superposition within Region C of the apparatus (see Figures 2.8 and 3.20(a)).

The power of the nth order beams depends on the power of the RF input of the AOM. Therefore for experimental uses where power control or light switching is required, AOMs can provide a flexible solution. The electric signal is customised using waveform generation and switches, and amplified so that enough power is provided for the AOM.

Pulses of light can also be created using AOMs by pulsing the RF signal. If the RF input is switched off, all the nth order beams disappear on a timescale determined by the speed of light in the AOM medium and the light beam diameter (i.e. $\mathcal{O}$(ns). The total power returns to the 0th order beam. In this way nth order beams are created with the same pulse shape as the applied RF pulse envelope, as well as the ramping on and off times of the AOM device itself. The particular AOMs chosen to be used in the experiment have ramping times of tens of ns. This was previously implemented when measuring the lifetimes of the $A^2\Pi_{1/2}$ and $A^2\Pi_{3/2}$ excited states [42].

3.3.6 Wavelength meter

Wavelength meters (WLM) are widely used to measure the wavelength of laser light using interferometry. In our case, we use a HighFinesse WS8-2 wavelength meter [67] which in combination with a HighFinesse 8 channel Photonic Crystal Switch can measure up to 8 laser light wavelengths. The WLM switches between the 8 different inputs in quick succession depending on the switching rate and capture times. Switching between the devices takes around 10 ms, so when locking 5 lasers simultaneously, a sample of each laser is taken approximately every 50 ms. The feedback loop capabilities of the WLM are therefore slower than this. The closed-loop locking bandwidth is sub-Hz.

In addition to measurement of frequency, this device is equipped with a proportional– integral– derivative (PID) controller which enables frequency control. We use this PID controller to simultaneously control the frequency of up to 8 lasers. Older versions of HighFinesse WLMs have been investigated [68, 69] and found to have a resolution of 200 kHz and an absolute frequency accuracy over the full operational range of 2 MHz.

In Figure 3.5, a Toptica DL-Pro laser is locked to the WLM for 5 hours and is measured by the same device. The measured frequency is plotted as a histogram in Figure 3.5. The standard deviation of the locked laser frequency is 240 kHz.

The root mean squared (rms) of the frequency distribution using different averaging times is shown in Figure 3.7. The plot shows that in the time scales of interest, between 1-1000s, the behaviour is as expected for a successfully locked laser. The resolution of the WLM itself limits the averaging that is possible. The device is specified to have a 200 kHz resolution in a single readout, which matches the standard deviation shown in Figure 3.6. The plot shows that averaging over many readouts allows a higher resolution to be gained. Plots such as Figures 3.5 to 3.7 do not contain information about the potential drift of the WLM itself.

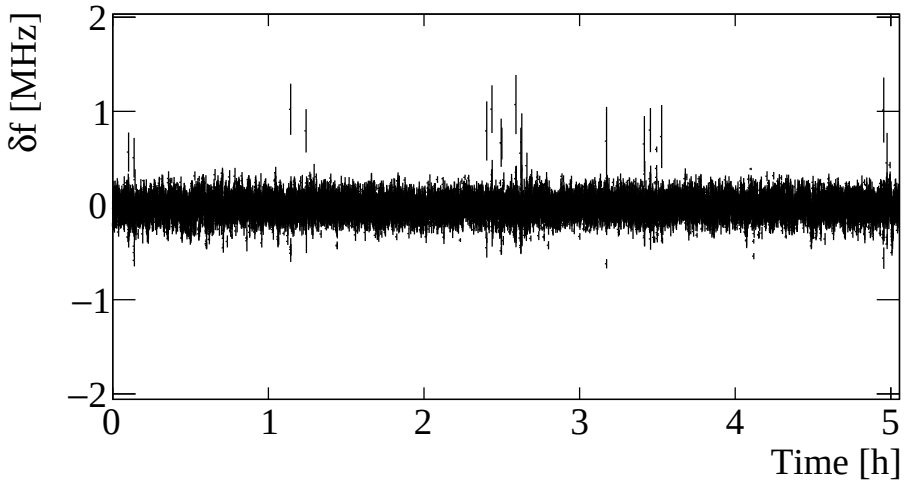

Figure 3.5: A Toptica DL-Pro laser frequency (Freq4) plotted versus time for 5 hours on the 25th of June 2022. This data was taken in parallel with the data shown in Figures 3.4(a) to 3.4(c). Short term frequency shifts that appear as outliers in this plot are associated with noise in the lab like opening doors. The laser relocks itself on a timescale of a few seconds in these conditions. We therefore avoid walking into or around the lab while running the experiment and exclude corresponding data in the analysis.

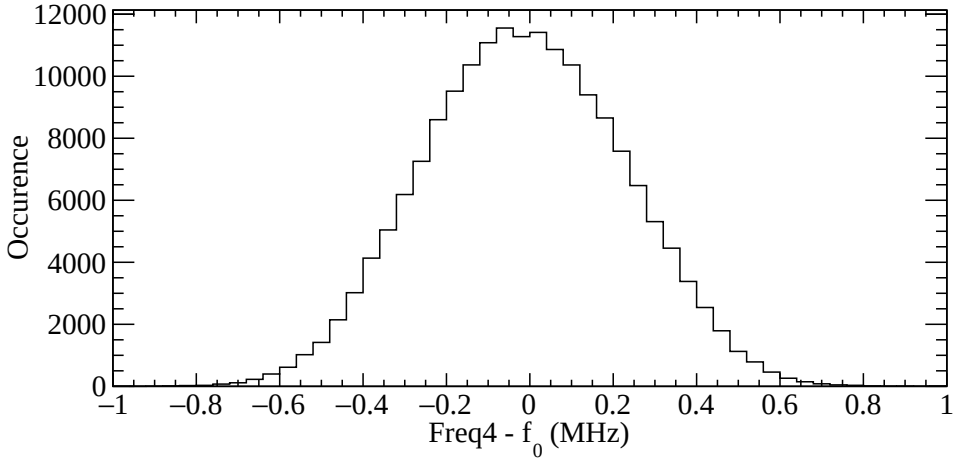

Figure 3.6: Histogram of Freq4 locked to the wavelength meter for 5 hours on the 25th June 2022, as measured by the device. Data is shown versus time in Figure 3.5. The vertical axis shows the number of times that frequency bin was measured (occurrence). The horizontal axis is offset by the locking frequency $f_0 = 367.632167$ THz. The standard deviation of the histogram is 0.24 MHz.

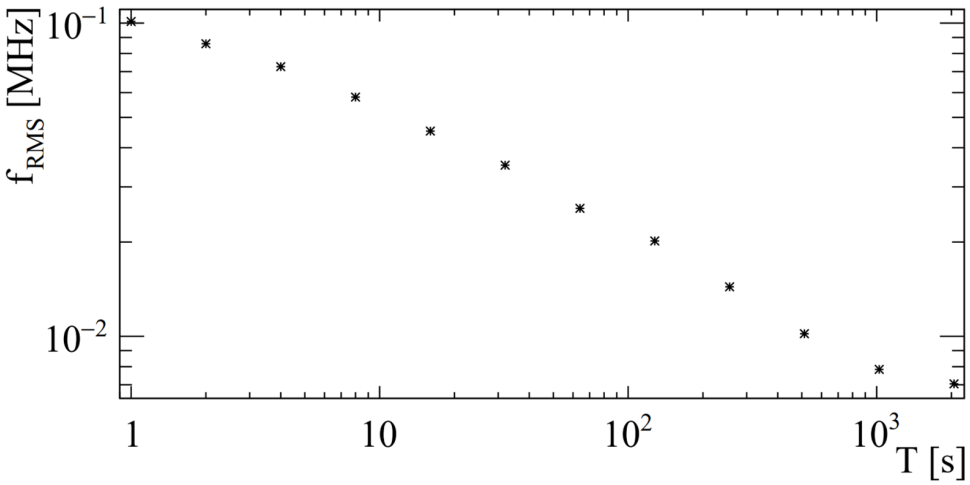

Figure 3.7: The root mean squared (rms) of the frequency distribution versus the averaging times used for the same data shown in Figures 3.5 and 3.6, for 5 hours. The first data point uses averaging of 1 second, and the frequency distribution has an rms of around 100 kHz. Averaging the data for longer reduces the root mean squared, until the resolution of the wavelength meter itself limits the reduction in the width of the distribution at at order of magnitude around 10 kHz at around $T = 10^3$ s.

3.3.6.1 Wavelength meter drifts

The frequencies of all the laser light used in the experiment are controlled by the WLM. They are also measured using the same device, which is not locked to an external frequency reference. In this configuration it would be possible for the WLM's frequency determination to drift due to environmental factors while the frequencies are locked, which would lead to a drift in the absolute frequency which would not be measured.

A measurement run of the experiment begins with spectroscopy to calibrate the frequencies of the laser light. Once the measurement run has begun, the frequency is not scanned again. Since all frequencies measured by the WLM will have drifted the same amount, one frequency is used to calibrate the WLM by measuring a particular hyperfine transition component. The linewidths of these transitions are typically a few MHz, and the peak frequency is estimated using a scan of approximately 5 MHz to a fraction of a MHz. It has been observed that the WLM did not need to be recalibrated when external factors such as the outside temperature and pressure were stable, and when this was necessary the drifts were < 5 MHz for a timescale of days and weeks. For example, a drift of < 10 MHz is observed between the spectra shown in Figure 3.15(b) and Figure 3.18 which were taken around 2 weeks apart.

For the population probes at Regions B and D (see Figure 2.8) using Freq1 and Freq4 (see Sections 3.4.1 and 3.4.2), the linewidths of the transitions means that only drifts of > 1 MHz would lead to a significant drop in statistics. Since both E-field directions are measured on timescales of less than 30 s, a possible false eEDM signal

is suppressed.

The optical pumping that takes place in Region B using Freq2 (see Section 3.4.3 and Freq3 (Section 3.4.4) uses high powers so the linewidths of the transitions with power broadening are ≈ 10 MHz, which means that the frequency is allowed to drift further without it affecting the measurement, making the optical pumping robust against frequency drifts than population probing.

Freq5 is used for the counterpropagating laser light pulses, which are approximately 1 GHz off resonance from the transition (see Section 3.4.5). Frequency shifts at the scale of MHz at such a high detuning change the light shift only very minimally ($\ll$ kHz), and this effect also depends on the power and power imbalance of the two beams (See Section 3.4.5).

The effect that these shifts have on the overall experiment in the context of a false eEDM measurement is discussed in detail in Chapter 5.

The stability of the WLM reading is shown by undertaking fluorescence spectroscopy of the $X^2\Sigma^+(N=0, F=1) \rightarrow A^2\Pi_{3/2}(J=3/2, F=1)$ transition over 12 hours as shown in Figure 3.8(a). Assuming the molecular transition frequency is unchanging, any drifts observed would be due to the measurement method using the WLM. The horizontal axis is the direct reading of the WLM which can undergo drifts due to temperature and other environmental variations. The colour scale shows the number of counts observed, from blue being the least counts to red being the most. The variation in the number of counts over time is due to the variation of molecules that are created by the supersonic source. The drifts over these timescales are < 0.5 MHz.

In Figure 3.8(b), the frequency of the peak over time is shown by applying fits to individual spectra using variable time bins. The frequency drift of the WLM is measured to be less than 1 MHz over the more than 12 hours of measurement time. The larger error bars after around 5 hours of running time are due to a reduction in statistics discussed in Section 3.4.2. If such frequency drifts were a limiting factor in the eEDM measurement precision, techniques such as frequency combs can be implemented in combination with a WLM to control and measure frequencies with an improvement of orders of magnitude.

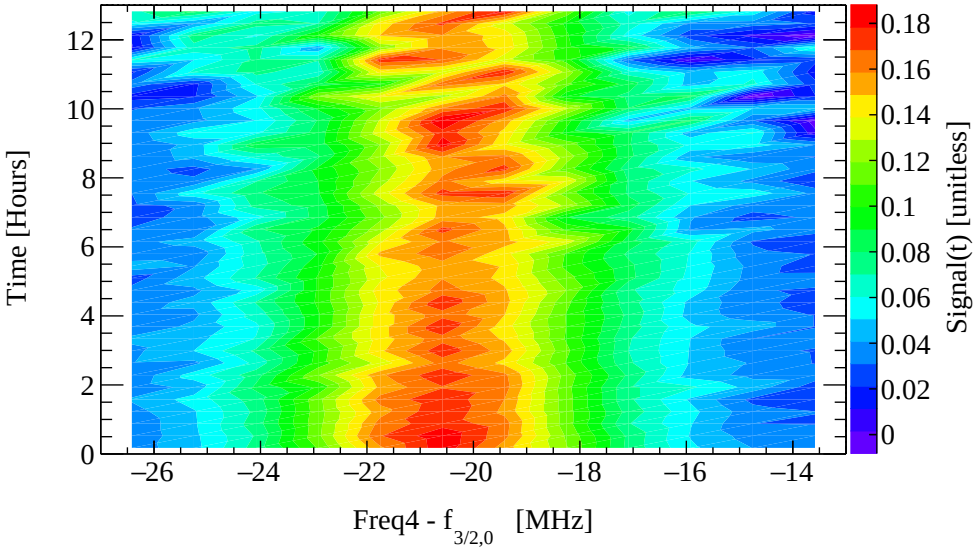

(a) 2D histogram showing spectroscopy of the $N = 0 \rightarrow J = 3/2$ transition in BaF taking place over more than 12 hours, with an offset on the horizontal axis $f_0 = 367.63214$ THz. Data taken on the 15th of December 2022. The colours (see legend) shows the fluorescence signal measured at D (see Figure 2.8) which has undergone processing in background subtraction and normalisation that is discussed in Sections 3.4.1 and 3.4.2. The plot indicates that frequency drifts of less than 500 kHz away from the initial frequency f_0 are observed over timescales of 12 hours. A zoomed out version of this plot is shown in Figure 3.15(b).

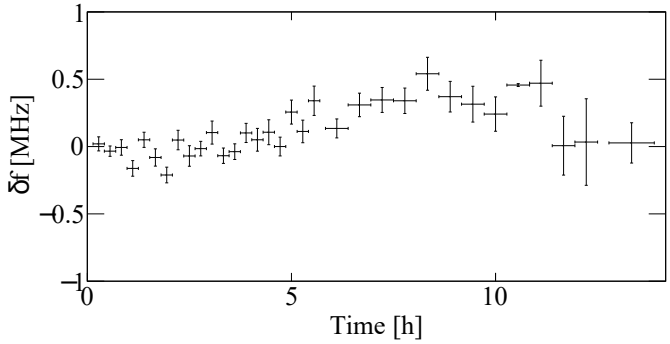

(b) The data shown in (a) is cut into variable bin sizes and a fit is applied to the spectrum in each bin individually. The centre of the peak in each fit is plotted versus the time at which the data was taken. The vertical error bar is the uncertainty in the frequency, and the horizontal error bars represents the measurement period. Over the first 5 hours the wavelength meter has drifted less than 0.3 MHz. As the time increases, the error bar of the frequency measurement increases as statistics decrease. The frequency drift of the wavelength meter stays within 1 MHz for the entire measurement.

Figure 3.8: Data taken on the 15th December 2022.

3.3.7 Photomultiplier tubes

In the eEDM experiment, light from laser induced fluorescence is collected using photomultiplier tubes (PMTs). These devices are used in single photon counting mode and to measure the associated timings. The signals are processed in electronic gates with a set length and delay time.

PMTs with a reasonable quantum efficiency are ideal for shot-noise limited light detection. The signal-to-noise in photon-counting conditions is superior when using a PMT versus other types of light collection. The viability of replacing PMTs with avalanch photodiodes was investigated [70] and found to not reach the shot-noise limit. For larger signals devices that use integrated timings are required, so photodiodes are preferable. The Thorlabs FGA04 InGaAs photodiode has a quantum efficiency of around 86% at 860 nm.

The eEDM experiment uses 4 PMTs in different locations (see Figure 3.3): one at Region B1 observing the normalisation signal, one at B2 for potentially monitoring the measured frequency of the Ba intercombination line to measure the WLM drift, and two at D on opposite sides of the vacuum system to increase the amount of photons collected from the LIF for the population probe.

The two PMTs at Region D are Thorlabs PMT1001/M 'Non-Cooled Multialkali PMT with Built-in Amplifier' [71]. The PMT type is a Hamamatsu Extended Red Multialkali H10721-20 [72]. The integrated transimpedence amplifier is for detection of signals from DC to 80 MHz. The quantum efficiency from 230 - 929 nm is $> 15\%$. The photocathode's active area has $\oslash 8$ mm.

At Region B, the Hamamatsu H7421-50 photon counting head 'Metal package PMT' with a GaAs photocathode and thermoelectric cooling [72] has been installed. It has a spectral response between 380 and 890 nm and a quantum efficiency of 12% at peak wavelength (800 nm) and has an effective area of diameter 5 mm.

For both of these PMT types, the sensitivity in mA/W of the photocathode drops approximately 2 orders of magnitude between $850 - 900$ nm. The laser light that is lower in wavelength has a significantly better detection rate by the PMT (see Appendix B). For this reason the light used for population probing and detection is set to frequencies probing the $X^2\Sigma^+ \rightarrow A^2\Pi_{3/2}$ transition (≈ 815 nm), rather than the $X^2\Sigma^+ \rightarrow A^2\Pi_{1/2}$ transition at 860 nm.

3.3.8 Light Collection from LIF

In order to reduce the background counts from scattered light entering the PMTs, the vacuum chambers are all painted with black paint (AZ Technology MLS-85-SB) which absorbs scattered background photons from detection laser light. The reflectance of the paint for light of wavelengths between 400-1000 nm is between 0.02 and 0.03. This UHV compatable black paint has been used for low-earth orbit space flights [73] and needs to be applied in a spray paint procedure in order to achieve an even layer and therefore optimal performance.

The PMTs have a particular active area which refers to the region of the photocathode that is sensitive to photons undergoing the photoelectric effect. The dimensions of the active area of a particular PMT used for measurements of laser induced fluorescence are taken into account when building a lens setup for that particular PMT. Lenses are used to collect a specific fiducial volume with a large solid angle. The light from this volume is then directed through a series of mirrors or lenses to be focused onto the active area of the PMT.

In order to increase the total efficiency ε in Equation 1.2, it is vital to maximise sensitivities of detectors. Other devices have higher sensitivities but do not work reliably in low signal conditions or have photon counting capabilities, such as photodiodes. Once the signal is large enough, for example with enhancement from optical pumping, devices other than PMTs would improve this efficiency, such as avalanche photodiodes.

3.3.9 Photodiodes

Photodiodes are used throughout the experiment for different laser beam power detection. The electrical signal is processed and calibrated by the data acquisition of the experiment to measure the power of the laser beam. It is important to use particular types of photodiodes for different functions. They must work for the near infrared wavelengths used in the experiment, and if the laser beam is pulsed, they must be fast enough to accurately measure the power. In our experiment, either InGaAs or Si photodetectors are utilised as they have a high responsivity for the wavelengths used.

Two Thorlabs DET36A/M Si Biased photodiode detectors are used to measure the power of the two polarisation components at Region D. The device is designed for detection of light between $350 - 1100$ nm and has a typical rise time at 632 nm of 14 ns. The photodiodes are connected to the DAQ to record that the pulse shapes and power recorded. The pulses are ≈ 100 μs long.

Other devices used to measure the power of the light include Thorlabs FGA04 [74], which uses an InGaAs pin and has a responsivity of around 0.7 A/W at the 860 nm used. The photodiode is mounted in an FC bulkhead connector to easily connect to optical fibres. The photodiode is connected to an optical fibre monitoring the power of the two polarisation components that are not sent to interact with the molecules. The light is pulsed and the average voltage is recorded in the DAQ while being displayed on an oscilloscope near the inputs of the fibres. This monitors the polarisation change of the two components as well as overall power changes of the laser.

The power of the CW beam, used for measuring the population in the ground $F = 1$

state, is monitored using a Thorlabs Si FDS1010 Photodiode [75]. The detector has a wavelength range of $350 - 1100$ nm, a rise/fall time of 65 ns and an active area of 100 mm^2. Reflected and scattered light near an aperture is measured. The responsivity of the photodiode at the 815 nm wavelength used is around 0.6 A/W.

3.3.10 Optical setup of the NL-eEDM experiment

Figure 3.9 shows the fast beam experimental setup, with the Regions A-D and the optical process that takes place in each region. Each laser system used is required to be simultaneously locked and running to interact with each molecular pulse as they pass from Region A to D.

The molecular beam pulses are created in Region A (Section 3.1). The number of molecules is normalised by probing the population in the $N = 1$ or 2 sublevel in Region B1 (see Section 3.4.2). The same fibre (Fibre A) also contains light from the rotational optical pumping setup discussed in Section 3.4.4. This pumping increases the number of molecules available in the $N = 0$ rotational ground state.

In Region B2 there are two optical windows into the vacuum chamber. In the first, hyperfine pumping takes place to maximum the number of molecules in the $N = 0$ ground state (see Section 3.4.3). The molecules fly through the magnetic shielding and electric field plates in Region C and interact with the pulses that enter the chamber at the back of the experiment in Region D (see Section 3.4.5). Finally the population of the $F = 0$ or $F = 1$ sublevel of the $N = 0$ ground state is probed in Region D. Data taken from the PMT here is additionally used to remove the background levels (see Section 3.4.1). The fibre labels given match the naming convention used in the experiment labs.

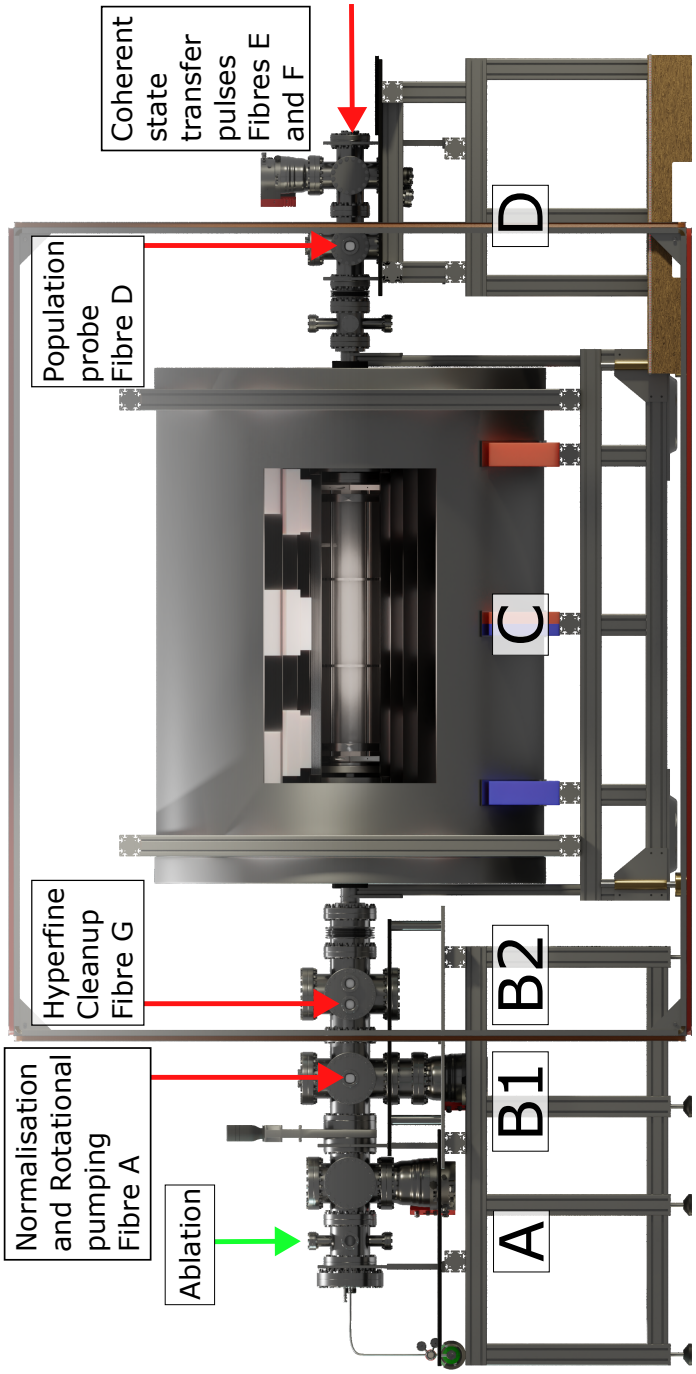

Figure 3.9: Fast Beam setup diagram here showing Regions A-D and highlighting the optical techniques used at each region and the optical fibres used to transport the laser light towards the molecules. The setup diagrams for the laser light input into the optical fibres are shown in the following sections of this chapter. Figure adapted from those found in [44].

3.4 Crucial experimental functions for the sensitive eEDM measurement

The $X^2\Sigma^+(N = 0) \rightarrow A^2\Pi_{3/2}(J = 3/2)$ transition plays a crucial role in the experiment, providing the information for the spin precession signal (see Equations 2.9 and 2.10). The spectrum is shown in Figure 3.10. The population of the $N = 0, F = 0$ level is proportional to the amplitude of the resonance at 26 MHz and the resonance at -22 MHz shows the population in the $N = 0, F = 1$ level. The precision is determined by the photon counting statistics, background signal level and the fluctuations of the molecular beam pulse flux.

In this section, the ways that the laser and optical systems are implemented to interact with the molecules in the NL-eEDM experiment are described. A number of experiments are performed simultaneously as shown in Figure 3.9 and here each setup and its results are presented. The steps to convert photon counts from a PMT to an uncertainty based on counting statistics is described.

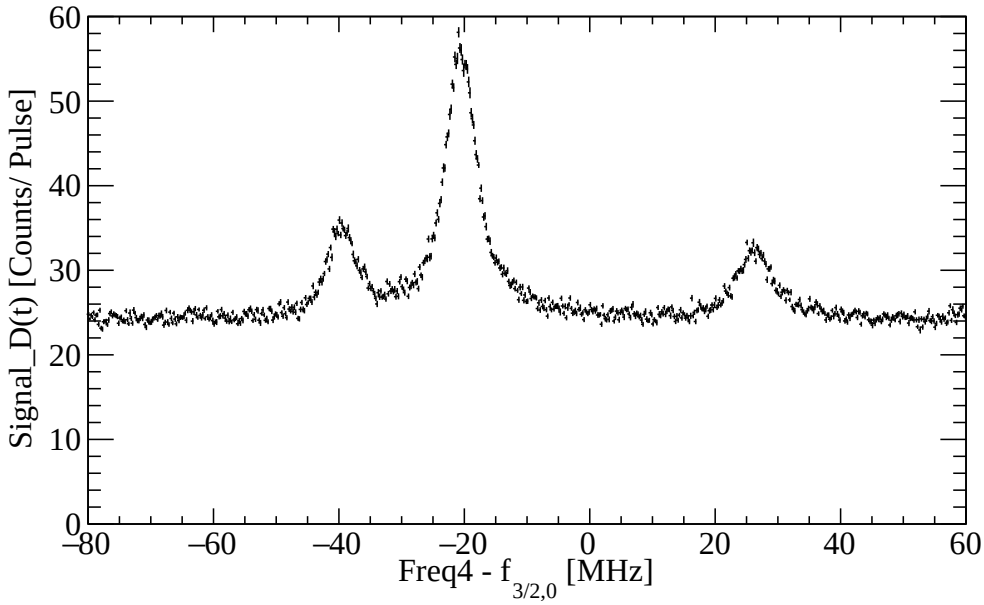

Figure 3.10: Resonance fluorescence of the $X^2\Sigma^+(N = 0) \rightarrow A^2\Pi_{3/2}(J = 3/2)$ transition. The eEDM experiment requires the ratio of the middle and far right amplitudes. The process of extracting this spectrum is described in this section.

3.4.1 Population probing and background removal at Region D

The optical setup diagram for the light creation is shown in Figure 3.11. Light at Freq4 (815 nm) is fibre-coupled. A fibre splitter sends part of the light to a WLM which is used to lock the frequency of the light. The rest of the laser light in the fibre is attenuated (Thorlabs 780-980 nm 780HP Fiber Attenuator) in order to control the power that is sent to the molecules. Fibre D transports the laser light from the Laser Lab to Region D of the experimental setup in the EDM lab.

The light enters the vacuum chamber through a optical window and intersects with the molecules 3.82 m after the gas nozzle of the supersonic source. The molecules arrive in Region D $\approx$ 6 ms after the trigger for the gas pulse release through the nozzle. The molecular beam has a diameter of $>$ 6 cm in this region from expansion (see Figure 3.3). The probe laser beam is expanded, collimated and then passes through a slit of 2 mm $\times$ 1 cm. This ensures that the light interacts with many molecules with a small Doppler shift ($\approx$ 3 MHz) while minimising the fluorescence region that will be imaged by the PMT. The LIF is collected and measured in the data acquisition system.

A set of two 10 cm diameter lenses of focal length f = 150 mm are placed outside the vacuum chamber window, where the light is collimated in between, giving an effective 75 mm lens system. They are 18 cm away from the interaction of the laser beam with the molecules. The light is then collimated by a f = 30 mm lens to go through an optical filter (Thorlabs FBH800-40 800 $\pm$ 20 nm with transmission 98.8%

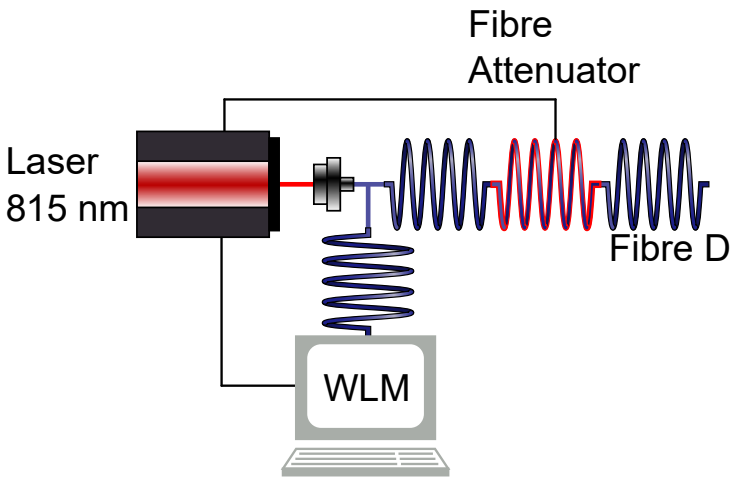

Figure 3.11: Freq4: Optical setup diagram showing the creation of the light used for probing the population at D. The light from a laser (red line) is directed into an optical fibre and then split using a fibre splitter. The frequency is controlled by a wavelength meter. The rest of the power is sent through a Thorlabs 780-980 nm 780HP Fiber Attenuator (red) which is connected to a voltage output from the laser control box. This light is then sent through Fibre D to interact with the molecules inside the vacuum chamber in Region D (see Figure 3.9).

at 815 nm or Thorlabs FBH860-10 860 ± 5 nm with transmission 97.5% at 860 nm) that reduces the background level by blocking light at other frequencies [76]. The light is then focused to maximise the number of photons that are collected by the diameter= 8 mm active optical area of the PMTs. The geometry yields a detection solid angle of $\frac{\Omega}{4\pi} \approx 2 \times 10^{-2}$. The total detection efficiency (including the fractional detection losses from each surface) is 1.4×10^{-3}.

This optical setup is implemented on two vacuum windows opposite to each other on the horizontal plane, in order to increase the number of counts collected. The PMTs used are two Thorlabs PMT1001/M devices in photon counting mode.

The probe laser light power is measured by a FND100 photodiode located perpendicular to the laser beam before it enters the vacuum window. Scattered light from the aperture that the laser beam passes through arrives at the photodiode and the signal is then converted and sent to the data acquisition.

Due to scattered photons from the probe laser light at Region D, the photon collection by the PMT in this region measures background levels that are similar in magnitude to the amplitude of the peaks measured by the PMT in spectroscopy. The background counts are not dependent on the presence of the molecules, but depend on the intensity of the laser involved in the LIF process. This background signal is independently determined using a time window when no molecules are present by the same PMT.

The LIF at Region D is collected by a Hamamatsu PMT with 14 consecutive timing gates each of length $\mathrm{L_{gate}}$ and starting delay $\mathrm{D_{gate}}$ after the initial trigger. The set values are shown in Table 3.2. These times are customisable, and the gate lengths are set as

$$\mathrm{L_{gate}} = 256 \times \frac{1}{\mathrm{Freq_{clock}}}, \tag{3.5}$$

where the frequency of the clock $\mathrm{Freq_{clock}}$ is 5 MHz as set by a Rigol waveform generator DG4162. The clock frequency is measured by the data acquisition. By using multiple consecutive gates, a plot of the time of flight (TOF) of the molecules is constructed to measure the velocity spread of the molecular pulse. The velocity is determined by the arrival time of the molecules as measured by the TOF, and changes in the backing pressure can be observed via changes of velocity. In addition, a gate of $\mathrm{L_{BG}}$ and delay $\mathrm{D_{BG}}$ is used, which is in between molecule pulses so the light from the LIF will not be present. This gate is used to measure the background level. The timings are shown in Table 3.2.

Spectroscopy using LIF at Region D is shown in Figure 3.12 for the $X^2\Sigma^+(N=0) \rightarrow A^2\Pi_{3/2}(J=3/2)$ transition, along with the scaled count rate of the background level. This scaling is included to acquire a background free signal Sig_i,

$$\mathrm{Sig\_bgred}_i = \mathrm{Signal\_D}_i - \mathrm{BG} \times \frac{\mathrm{L_{gate}}}{\mathrm{L_{BG}}} \tag{3.6}$$

where the background reduced count rates $\mathrm{Sig\_bgred}_i$ are summed. $\mathrm{Signal\_D}_i$ is the number of photons counted by the PMT in each of the consecutive 14 gates numbered

by i with gate lengths L_{gate}. BG is the count rate collected by the PMT in the background collection gate which has a gate length of L_{BG}, which is much longer than the signal gates to maximise the statistical precision. To account for this gate length difference, the background rate is multiplied by the ratio of the gate length differences.

Name	**Value**
L_{gate}	51.2 μs
D_{gate}	6.25 ms
L_{BG}	10 ms
D_{BG}	7.018 ms

Table 3.2: Table showing values that are set for gate timings. Timings are digitally set with clocks referenced to the GPS stabilised Rb clock at 10 MHz with 10^{-12} long-term stability. These timings are known to better than 100 ps because of the clock frequency stability over 1 second of 10^{-10}. The value of L_{gate} originates from setting 256 clock ticks of from a 5 MHz signal from a Rigol waveform generator (DG4162). L_{BG} comes from an analogue D15 University Heidelberg gate and delay generator in the VME crate with about a 1 % accuracy.

For the eEDM experiment, the frequency is fixed so the light probes either the $F = 0$ or $F = 1$ hyperfine level in the ground state.

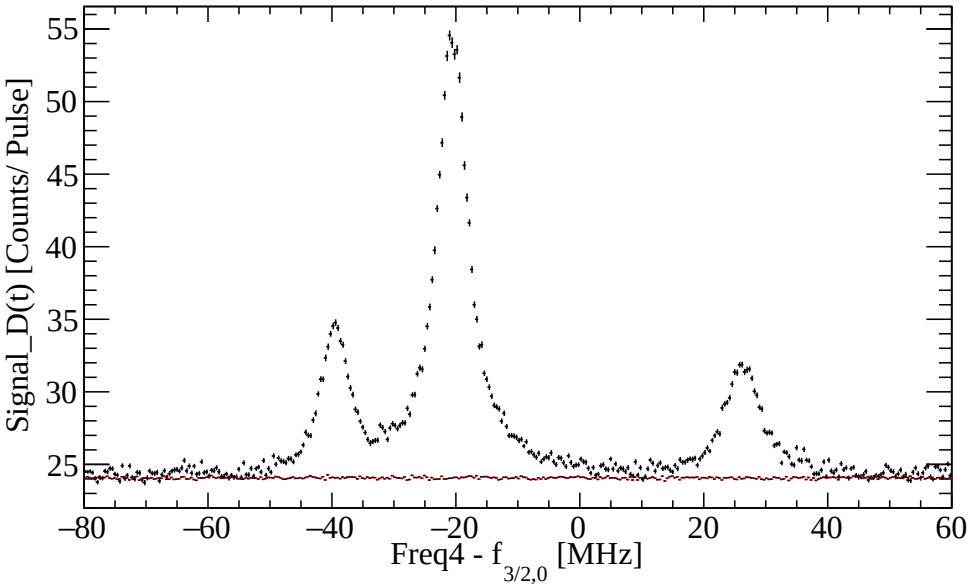

Figure 3.12: Black data points: Spectroscopy of the $X^2\Sigma^+(N = 0) \rightarrow A^2\Pi_{3/2}(J = 3/2)$ transition at position D after the interaction zone (Signal˙D(t)). In this case no optical pumping or spin precession has taken place. The frequency is measured by the WLM (Freq4) with the centroid of the transition subtracted ($f_{3/2,0} = 367.63214$ THz). Approximately 2 hours of data has been averaged and the sum of all 14 gates is plotted. Additional structure in the spectrum comes from different Ba isotopes in the beam. Red data points: the almost flat line is the background counts that have been measured by the same PMT using an additional gate at a time in between molecular pulses (BG). The value in this gate is multiplied by a factor to match the timing of the gates for the main signal. The background rate is measured to be around 25 counts per pulse. The background level depends on the power of the probing laser and comes from scattered photons. The same spectroscopy data is shown with the background subtracted versus time in Figures 3.15(a) and 3.15(b). Data taken on the 15th December 2022.

3.4.2 Normalisation of signals

The supersonic source creates pulses of BaF molecules. Molecular sources that rely on ablation of solid targets have fluctuations in the number that are created on a shot-by-shot basis [77], due in part to the rotation of the uneven surface of the metal [78], in this case Ba, that is ablated. If the Ba target is instead not rotated, the ablation will cause the number of molecules produced to completely reduce to 0 on a time scale of minutes.

Such a fluctuation of number of molecules could make it difficult to probe a change in population of molecules in a particular energy level, as it could be mistaken for an eEDM signal. It is necessary to create an experiment where the electric field direction

can be changed while the rest of the parameters are kept as constant as possible to measure asymmetry created by an eEDM signal. Therefore a normalisation process has been implemented to overcome the fluctuations.

At position B1 of the experiment, the $N = 1$ state is probed via an excited state ($A^2\Pi_{3/2}(J = 3/5, 5/2)$) using a Coherent MBR 110 Ti:Sa laser (Freq1). These excited state is forbidden to decay to the $N = 0$ ground state due to the selection rules. The signal collected as the number of photons at B is called Signal_B.

In Figure 3.13, the optical setup used to create the light for normalisation is shown. Freq1 is frequency controlled by the WLM at 815 nm. The light is sent through an AOM connected to an RF source of 197 MHz. The 1st order beam is connected to an optical fibre than is connected via fibre combiners to Fibre A.

Fibre A emits the light in free space, and this light is then directed into the vacuum chamber of the experiment at Region B1 as is shown in Figure 3.9 approximately 1 m downstream from the gas nozzle. The molecular beam has a diameter of 11.4 mm in this region (see Figure 3.3). The laser beam has a diameter of a few mm and interacts with the molecules, inducing fluorescence.

After interacting with the molecules, the laser light shines through the vacuum chamber and exits through another vacuum window back into free space. This light is collected by a Thorlabs FDS1010 photodiode to measure the power in the two beams and is connected to the data acquisition system.

An achromatic 2 inch diameter, focal length 75 mm diameter lens focuses the spontaneously emitted light onto the PMT (H7422-50 Hamamatsu or R6060-12). The collection is perpendicular to the laser beam that induces the fluorescence light. The active area has a diameter of 5 mm. A bandpass filter (800 ± 20 nm, [76]) reduces background photons being transmitted onto the PMT, and blocks the light from the rotational pumping laser beam.

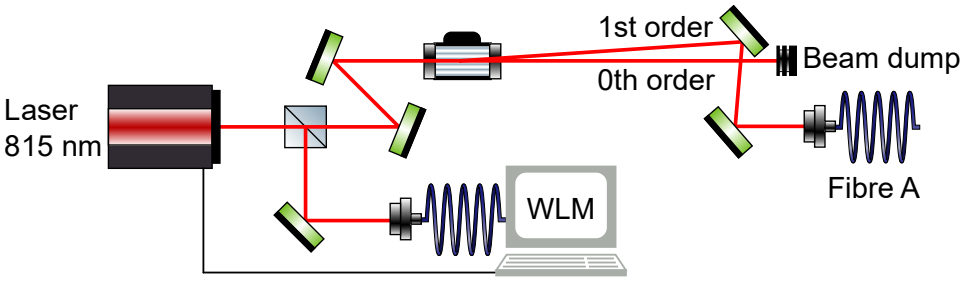

Figure 3.13: Freq1: An ECDL at 815 nm is frequency controlled by a wavelength meter. The rest of the light is directed through an AOM. The 0th order beam is blocked while the 1st order beam is directed onto an optical fibre that sends the light to interact with the molecules.

By dividing the number of photons collected at Region D by the number of photons collected at Region B for a particular molecular shot, the fluctuations in number of molecules are reduced. This is defined as

$$\mathrm{Sig}(t) = \frac{\sum \mathrm{Sig\_bgred}_i(t)}{\mathrm{Signal\_B}(t)}, \tag{3.7}$$

where the already background reduced numbers of photons in each gate $\mathrm{Sig\_bgred}_i(t)$ are summed and then divided by the number of photons measured at B, Signal_B. We have found that the photon collection at position B is almost background-free (see examples in Appendix C) so no background photons need to be removed.

In Figure 3.14, the counts per second collected at Region D are plotted versus the counts per second collected at Region B of the apparatus. The linear relationship between the count rate at Region B versus Region D is shown in the middle region. The signal at B has a lot more counts per second than the signal at D due to a combination of a narrower beam at this region and therefore more molecules are involved the interaction. The normalisation process has been studied in a bachelor project [79].

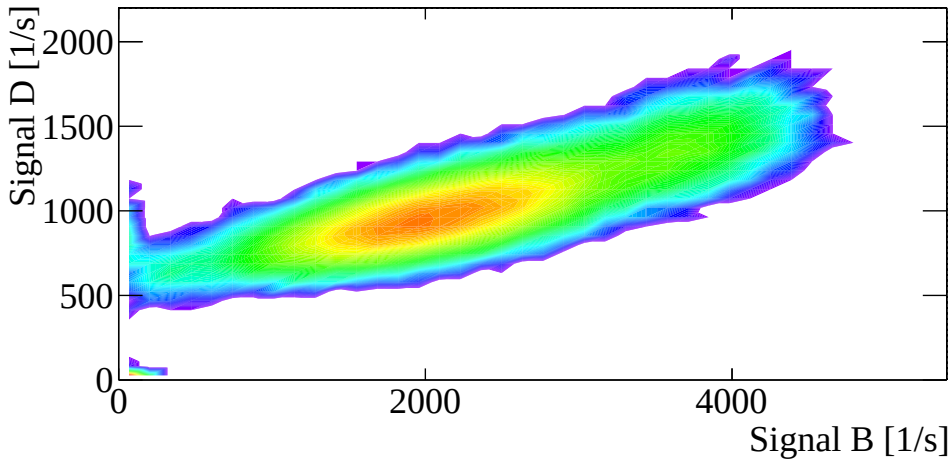

Figure 3.14: The counts per second measured at Region B are plotted versus the counts per second measured at Region D of the apparatus for each molecular shot. The colours show the number of entries in the bin of the histogram, where red is the highest and blue is the lowest. The white shows no data entries in that bin. Shows that signal at D has a linear correlation with the signal at B and can therefore be used for normalisation. At higher signal rates the data becomes less linear due to PMT saturation. When there are no counts on a particular PMT due to either a laser light frequency or power change, this is shown by such a plot. These counts can easily be filtered out to recover the normalisation curve. Measuring this curve is essential for correct normalisation. This plot shows that the background at D was approximately 600 counts per second. Data taken on the 20th June 2023.

3.4.2.1 Normalisation of a long term spectrum

In Figure 3.15(a), the spectra shown in Figure 3.15 has plotted versus time. There are observable fluctuations in the first 4 hours of the experiment and the overall number of molecules and therefore the signal counts reduce over time. Both of these are observed to be overcome in Figure 3.15(b), where the normalisation has taken place. In this case the normalisation was achieved using the $X^2\Sigma^+(v=0, N=2) \rightarrow A^2\Pi_{3/2}(J=3/2)$ transition. Both plots have already had the background counts removed, which is why the noisier parts of the signal have a negative count rate in the colour scheme shown on the right of the plots.

The statistical deviations that occur are observed to be stronger as the signal reduces. This result shows that the experiment can run for 3-4 hours without changing anything with little statistical deviation. When the signal drops much further, the background noise becomes significant.

There are sometimes shots from the source where very few or no molecules are produced. When this happens the normalisation process cannot account for the reduction in signal, as at both B and D the signal has reduced. This is shown in Figure 3.15 when the signal drops and then returns. It can additionally be observed in Figure 3.8(a), which is more zoomed in and has different binning.

In Section 3.3.6.1, the same processed data as shown in Figure 3.15 was binned into variable time bins and a fit was made to each spectrum. The fitting procedure is described in Chapter 4. In that case the frequency of the peak at each time bin was plotted in Figure 3.8(b). The extracted amplitudes from those fits are shown in Figure 3.16. For a Signal_B range between $100 - 200$ counts/shot, the normalised and background reduced amplitude at D is stable. The amplitudes extracted from the fit are between 1 and 1.5, whereas the colours shown in Figure 3.15 refer to amplitudes of between 0.15 and 0.20 for the same transition. This is because the definition of amplitude in the fit is defined as the factor that is multiplied to the Voigt parameters, which depend on both the Lorentzian and Guassian parameters. We use Cern ROOT's Voigt function in the TMath class. This is not the same as the definition in Equation 3.7.

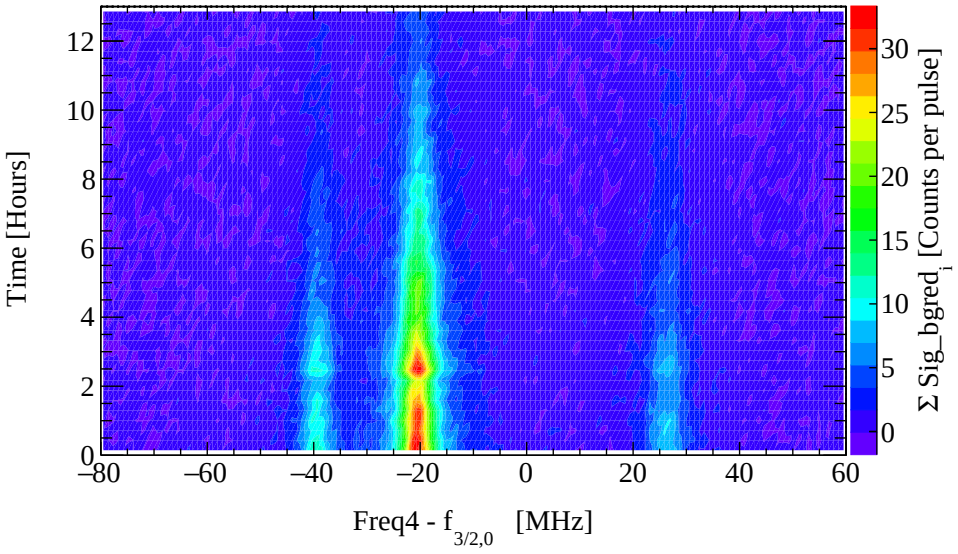

(a) Background counts have been subtracted and no normalisation has taken place. The experiment produces molecules at a high rate for around 4 hours. The raw data used in the first two hours of this plot is averaged and shown in Figure 3.12. The signal to noise ratio varies and eventually significantly reduces after a few hours.

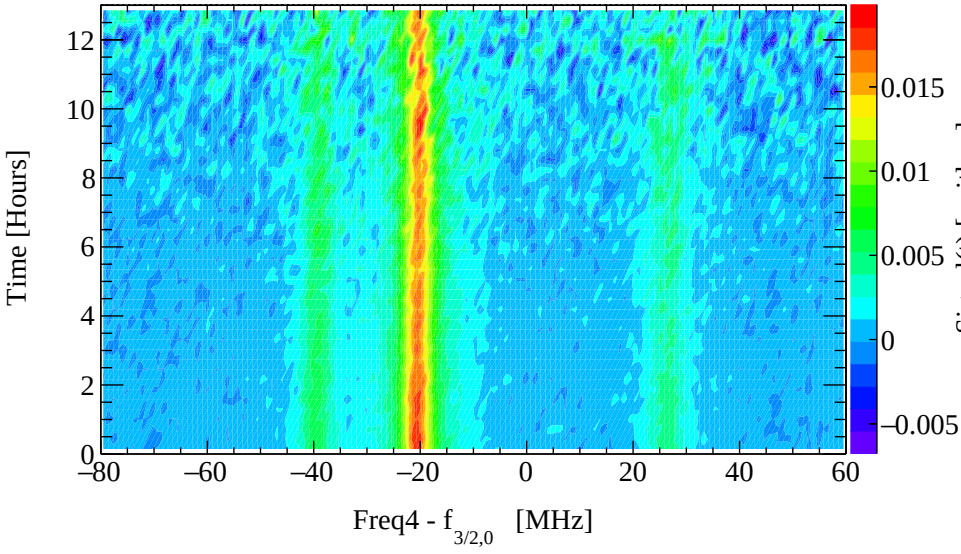

(b) With background reduction and normalisation. As the signal to noise ratio drops the normalised signal becomes noisier due to the lack of statistics.

Figure 3.15: Spectroscopy of the $X^2\Sigma^+(N = 0) \rightarrow A^2\Pi_{3/2}(J = 3/2)$ transition at position D over time, without (a) and with (b) normalisation probing the $X^2\Sigma^+(N = 3)$ ground level. The spectra frequencies are zeroed around $f_{3/2,0} = 348.63216$ THz measured by the WLM. Data taken on the 15th December 2022.

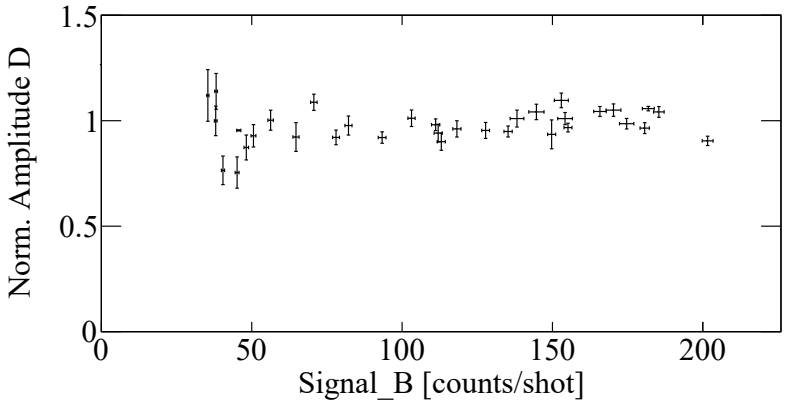

Figure 3.16: The normalised, background removed data of the spectroscopy at D shown in Figure 3.15(b) has been binned in variable time bins. The amplitude of the fit for each bin is plotted versus the signal count at B (Signal_B) in the raw data. The amplitude plotted is different to the values plotted in the colour palette in Figure 3.15 as it is defined as the area under the curve for that peak. For the smallest signal rates, the fit does not work so these are not shown. For larger Signal_B values, the error bars for the normalised amplitude at D are smaller because there are decreased statistics and the data has more noise. The horizontal error bars show the variance of the Signal_B in that bin. The frequency of each bin is also calculated in the same fit and is shown in Figure 3.8(b) versus the time of each bin. Data taken on the 15th of December 2022.

3.4.3 Hyperfine optical pumping

The eEDM experiment relies on population probing of the ground $X^2\Sigma^+(v=0,\ N=0,+)$ state. The hyperfine structure of the ground state means there are two $F=0,1$ levels. After the spin precession process and the second pulse is applied, the molecules populate one of these two hyperfine levels. If the population of one of these levels is depleted before the spin precession takes place, then all the population in that level when it is probed must be from the spin precession.

An extended cavity diode laser using a Thorlabs L850P030 diode at 860 nm is used for hyperfine cleanup of the $N=0, F=1$ level for state preparation before the molecules enter the interaction zone and undergo the spin precession. This laser is defined as Freq2 in the data acquisition.

The laser light is split, with one component sent to the WLM to control the frequency. The rest is directed via mirrors to an optical fibre labelled G that transports the light to the EDM lab. This is shown in Figure 3.17. The light is then emitted and directed to interact with the molecules at Region B2. The laser beam has a width > 4 mm and power that is sufficient to empty the the $F=1$ sublevel of the $N=0$ ground state.

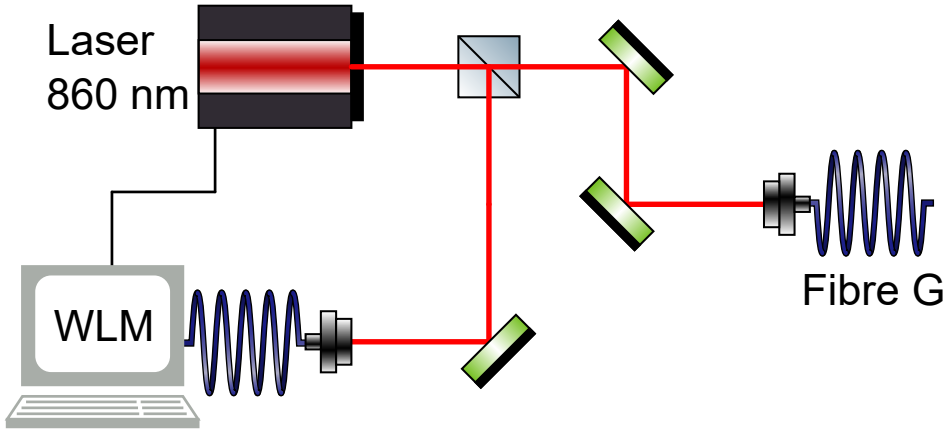

Figure 3.17: Freq2: An optical setup diagram showing the creation of light used for hyperfine pumping the molecules out of the $F=1$ level of the ground state. The laser is frequency controlled by a wavelength meter, with the rest of the light directed through fibre G to interact with the molecules.

In Figure 3.18, the $A^2\Pi_{3/2}(v'=0,\ J'=3/2,-) \rightarrow X^2\Sigma^+(v=0,N=0,+)$ transition is shown in two different circumstances: with the hyperfine population distribution that comes out of the supersonic source, and when optical pumping out of the $F=1$ state has been applied. The transition used for this optical pumping is the $A^2\Pi_{1/2}(v'=0,\ J'=1/2,F=1-) \rightarrow X^2\Sigma^+(v=0,N=0,F=1,+)$ transition. The efficiency of the optical pumping is around 80%. An increase in the population of the $F=0$ ground state is observed by the increase of the amplitude of the rightmost peak. Molecules will also decay from the excited state to the $N=2$ rotational level

of the ground state and be lost from the rest of the experiment.

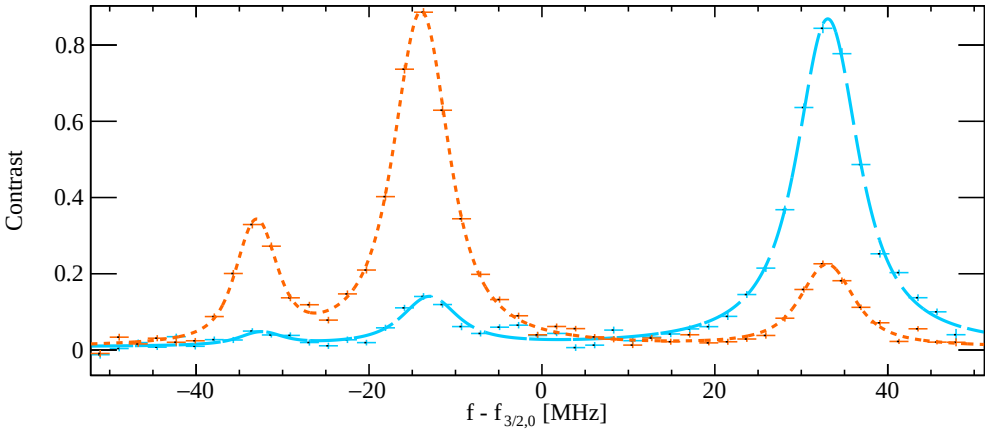

Figure 3.18: The $A^2\Pi_{3/2}(v' = 0,\ J' = 3/2, -) \rightarrow X^2\Sigma^+(v = 0,\ N = 0, +)$ transition with (blue dashed line) and without (orange dotted line) optical pumping out of the $F = 1$ ground hyperfine level with efficiency of around 80%. The horizontal axis is the wavelength meter measured frequency, and is centered around the centroid of the transition $f_{3/2,0} = 367.63216$ THz. as measured by the WLM. Data taken 2nd December 2022.

From left to right are the F level transitions $1 \rightarrow 1, 2 \rightarrow 1$, and $1 \rightarrow 0$ transitions, given in the form $|e\rangle \rightarrow |g\rangle$. The splitting between the left two peaks is the hyperfine splitting in the excited state, while the ground state hyperfine splitting is given by the difference between the leftmost and rightmost peaks.

An line has been fitted to the experimental data points as discussed in Section 4.3.3 which is shown as the dotted and dashed lines. The frequency axis is centered around the centroid of the transition, which is the difference between the two centroids of the hyperfine structures of the excited and ground states.

This optical pumping takes place before the molecules are sent to the interaction zone and undergo spin precession. The leftover molecules in the $F = 1$ ground level lead to a reduction in the contrast that is achieved, and act as a background level in population probing to test for an eEDM as discussed in Section 5.2.2.

3.4.4 Optical pumping for rotational population increase

By combining laser light with understanding of energy levels and allowed transitions, the population distribution created by the supersonic source is manipulated to suit particular experiments. Population is transferred from one sublevel of the ground state to another. This can be between vibrational, rotational or hyperfine levels.

In order to maximise the population in the N=0 ground state, rotational optical pumping is used. Population is transferred via an excited state. Without the use of additional fields, population can only be transferred from even to other even rotational states, for example $N = 2 \rightarrow N = 0$, due to parity selection rules. In the case shown in

Figure 3.19, the population is transferred from the $^2\Sigma^+(N = 2, +)$ rotational ground state to $(N = 0, +)$ via the $A^2\Pi_{1/2}(J = 1/2, -)$ excited state. This is possible as the excitation changes parity, and the spontaneous emission transfers some of the population to the $(N = 0, +)$ level with another change of parity.

In the eEDM experiment, the frequency Freq3 of one of the lasers is set at the peak shown in Figure 3.19(a). The population in $N = 0$ increases by approximately 50%. The hyperfine structure is not observed due to power broadening, which means that only one frequency is required to be applied in order to transfer population from both $N = 2, J = 3/2, F = 1, 2$ hyperfine sublevels in the ground state. The single possible transition from the level labelled $|N = 2, J = 5/2, F = 2\rangle$ (which is mixed with the level labelled $|N = 2, J = 3/2, F = 2\rangle$) does not transfer the population as the splitting is too large. If required, an AOM or EOM could be applied to create a frequency that would transfer both frequency groups simultaneously, but the mixed ground state gives a much smaller amplitude so doesn't give as large a gain in population. The same spectrum is plotted directly using LIF at low power in Section 4.3.2, where the hyperfine substructure can be observed. In that case the population of the $|N = 2\rangle$ level is probed rather than that of the $|N = 0\rangle$ which is shown in Figure 3.19(a).

In Figure 3.19(b), the frequency is set at the centre of the peak shown in Figure 3.19(a) and the population at D is probed versus time. The plotted vertical axis shows the number of counts per pulse (or shot) with the background level measured in a later PMT gate subtracted as shown in Equation 3.6 and Section 3.4.1. The drop in signal from approximately Time $= 0.4 - 1.7$ hours, when the rotational pumping frequency is far detuned from resonance, shows that when on, the rotational pumping approximately doubles the population in the $N = 0$ ground level.

The binning of the plotted histogram is 512 readout cycles, which corresponds to 51.2 seconds of measurement time. This binning has been chosen to clearly show the time scale of the noise from target rotation. In addition, over time, the overall number of molecules produced by the source reduces. Normalisation as discussed in Section 3.4.2 is applied. In this case, the experiment is run without any changes for > 2 hours before the signal halves in strength.

To rotationally transfer population from odd parity states $(N = 1, N = 3, ...)$ to the even states $(N = 0, N = 2, ...)$, a small electric field is required. The parity pairs in the $A^2\Pi_{1/2}(J = 3/2)$ are tens of kHz apart, so a small electric field can create parity mixing which allows a transition from the $N = 1$ ground state via the mixed excited state to the experimentally useful $N = 0$ ground level. Electric field plates have been inserted into the vacuum chamber at B1 to apply this rotational transfer using parity mixing.

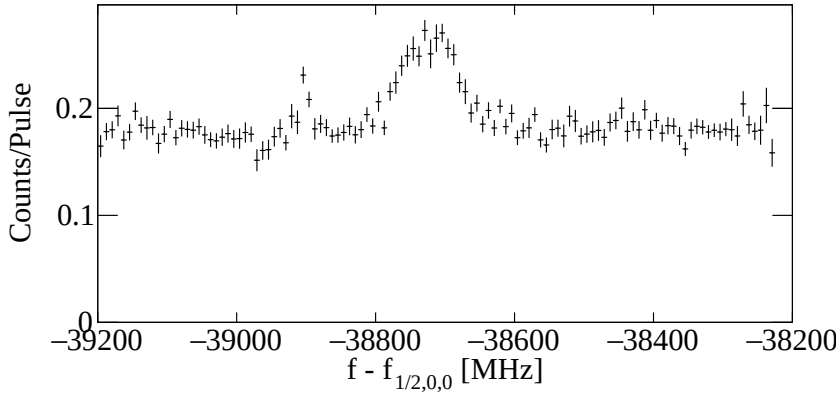

(a) The population in the $N = 0$ ground state is probed at position D, while the laser frequency Freq3 used for rotational pumping at position B is scanned across the resonance for the $X^2\Sigma^+(N = 2) \rightarrow A^2\Pi_{1/2}(J = 1/2)$ transition. The frequency is offset by $f_{1/2,0,0}$ which is the centroid of the $X^2\Sigma^+(N = 0) \rightarrow A^2\Pi_{1/2}(J = 1/2)$ transition. The vertical axis is the normalised signal Sig. At the peak (-38750 MHz) of the transition, the population in the $N = 0$ ground state increases due to the rotational optical pumping. The intensity is set high enough that the individual hyperfine structure is power broadened. The peak at -38900 MHz has a smaller amplitude as it from a labelled $\Delta J = 2$ that is experimentally possible to observe due to the F-mixing with another level (see Chapter 4). The transition is shown using LIF in Section 4.3.2.

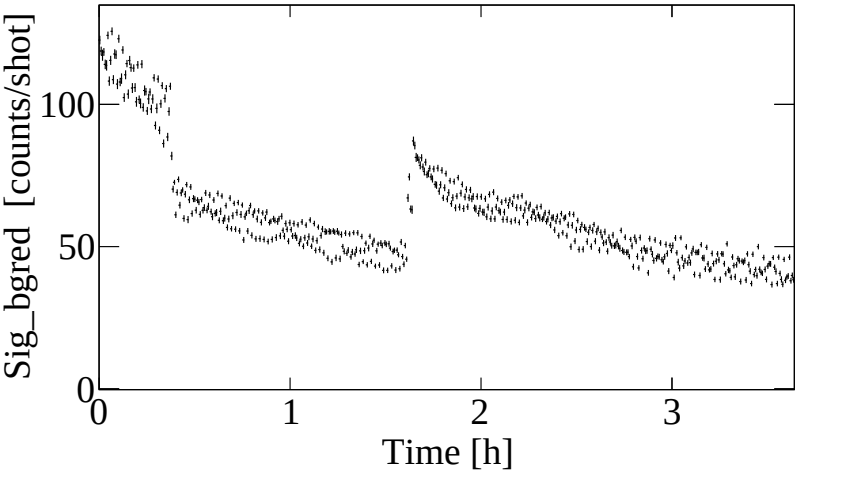

(b) The background reduced photon counts per shot Sig_bgred for the population probed at position D versus time with a bin size of 51.2 μs. At Time = 0, the rotational pumping is applied with Freq3 set to the peak frequency shown in Figure 3.19. The target rotation gives noise on the timescale of approximately a minute. At Time $\approx$ 0.4 hours, the rotational pumping frequency is changed to be far off resonance and at Time = 1.7 hours the frequency is relocked to the peak frequency and the rotational pumping resumes.

Figure 3.19: Population increase from rotational optical pumping. Data taken 20th June 2023.

3.4.5 Coherent state transfer pulse creation

The spin precession laser has a fibre optic output. The fibre is connected to a launcher, and the beam is split using a polarising beam splitter (PBS). Each of the the beams are sent through an AOM (see Section 3.3.5). The first order output beams of each AOM are then sent through optical fibres towards the experiment. This is shown graphically in Figure 3.20(a). The optical fibres are manipulated using FiberControl FPC-3 devices in order to control the polarisation of the light that is emitted.

As is shown in Figure 3.20(b), the outputs of the fibres are combined using a polarising beam splitter to have orthogonal polarisations to each other, and a frequency difference that is equal to the frequency difference of the electrical signals applied to the two AOMs. The polarisation control is such that maximum power is emitted through the PBS to the rest of the experiment. The combined beam is then expanded and everything except the central few mm radius of the expanded beam is blocked by a variable aperture. This light beam is then sent into Region D of the experiment through a window to counter propagate with the molecular pulses when they are between the electric field plates in Region C.

By pulsing the signals sent to the AOMs, the light beam is timed to interact with the molecules only when they reach the beginning and end of the interaction zone. These two pulses begin and end the spin precession of the molecules. The light can also be timed to have one long pulse throughout the interaction zone or one short pulse to undertake magnetic and electric field mapping.

High precision of the timings of the RF signals sent to the AOMs is essential. The RF signals from the waveform generators are controlled by frequency shift signals (Minicircuits ZASWA-2) which are generated by different outputs of the same waveform generators (Rigol DG4162, DG4202). The set points are saved using the experiment's DAQ. The waveform generators are triggered using the same signal sent to the ablation laser and synchronised to the Rb clock.

To measure the power and shape of the light that is pulsed to create and readout the superposition within Region C, the beam is split by a wedge and then by a polarising beam splitter that separates the oppositely polarised beams onto two Thorlabs DET36A/M Si detectors. The measurements of these photodiodes are then digitised using a 5 V, 12bit analog to digital convertor module (ADC, Caen SIS3300) [44] to detect the pulse shapes. A 3 ms time window is digitised after the Q-switch trigger of 2.621 ms (see Figure 3.22) using a time resolution of 1.28 μs. The device is synchronised to the 10 MHz rubidium clock reference. The measurement is taken for each shot at a rate of 10 Hz. The signals for one of the PMTs is shown in Figure 3.21. The leading edge of each change is a sharp change and then the trailing edge has a slower change due to the rise time of the photodiodes used.

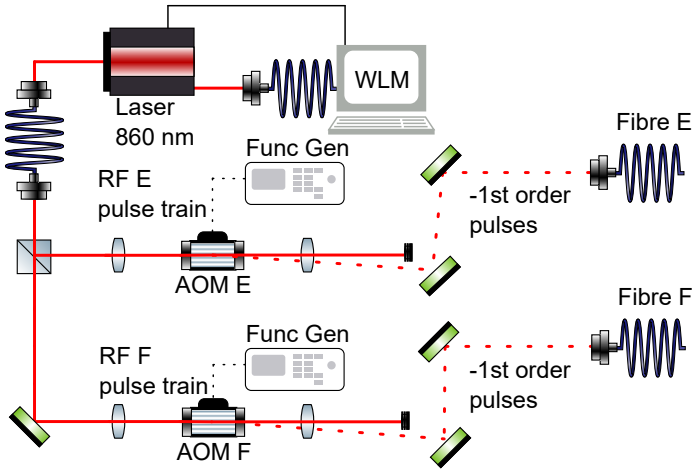

(a) Freq5: Frequency controlled laser light is split by a beam splitter into two beams, and each beam is passed through an AOM which is connected to RF pulses generated by function generators. The pulsed 1st order beams of each AOM are aligned into optical fibres E and F.

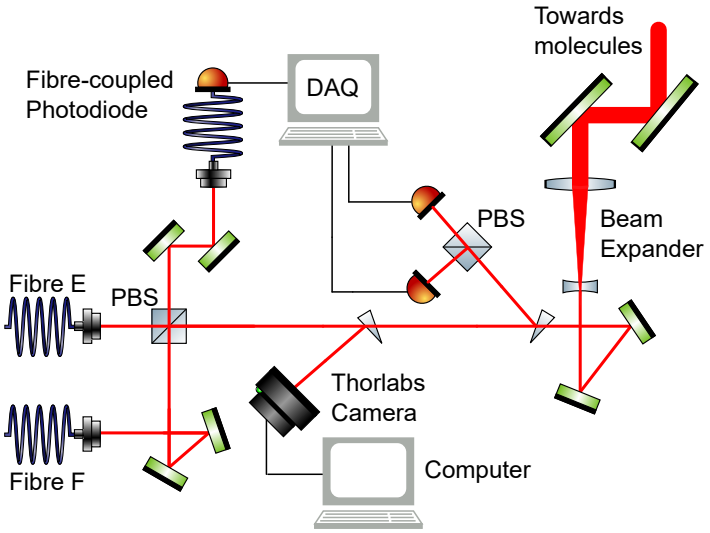

(b) The opposite polarisation components of beams E and F are overlapped using a PBS, expanded using a telescope and aligned towards the molecules. The beam is pulsed and these pulses are timed to collide with the molecules within Region C. In addition, the two other oppositely polarised beams from the PBS are sent through an optical fibre onto a fibre-coupled photodiode to check the alignment of the beams. A wedge beamsplitter sends the two beams onto a Thorlabs camera to verify their alignment and a second wedge beamsplitter sends the light through an additional PBS to measure the individual beam powers using two photodiodes.

Figure 3.20: Optical setup diagrams showing how the laser light pulses are created, how their powers and overlap are measured and how the expanded light pulses are directed towards the molecules. Not shown: polarisation control for fibres E and F to increase the power in the light that interacts with the molecules.

In addition, the two other oppositely polarised beams are directed into an optical fibre that is connected to a fibre coupled FGA04 InGaAs IR photodiode. This is used for two purposes: firstly to check the alignment of the overlap of the two laser beams; and secondly to measure the power of the laser beams in the components of the polarisation that is not directed towards the molecules. This signal must therefore be minimised to maximum the power in the laser beams that interact with the molecules in Region C. The signal from this PMT is digitised in the same way and the information is stored in the DAQ datastream.

For every shot, the raw data saves the shape of the pulses. In the processed data stream (.root file), the threshold (horizontal dashed line in Figure 3.21) is used to define the time of the beginning and end of each pulse and therefore to calculate the pulse length t and the period from the beginning of the first pulse to the beginning of the second pulse T. A zero level is defined by subtracting the intensity measured a time before the arrival of the laser light pulses. The area under the curve is calculated which is the integral of the intensity in the pulse time. In Section 5.4.2 the intensity of these pulses is changed and in Section 5.3.3 the length of time of a pulse is changed. Both of these kinds of changes are measured in the data using this technique. The length of time per bin of the measurement is the inverse of the sampling rate, so a sampling rate must be chosen that enables enough precision while not slowing the data acquisition with the size of the file.

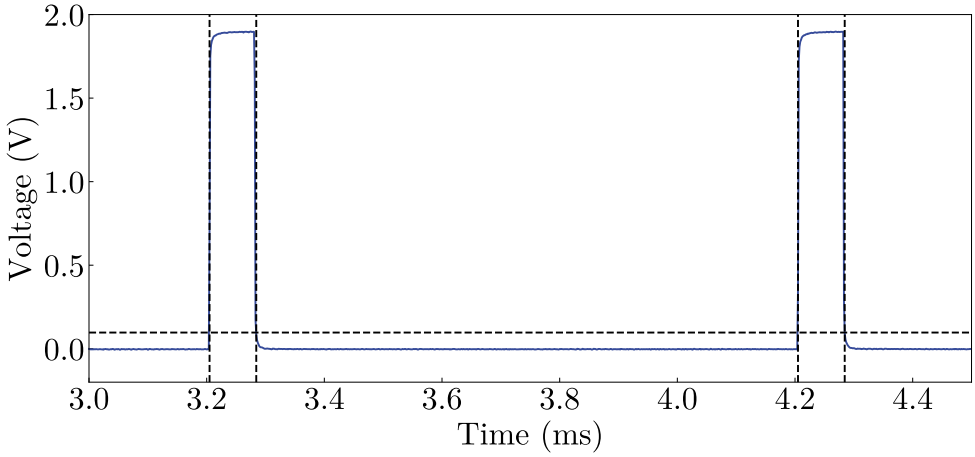

Figure 3.21: Single shot digitisation of a set of superposition creation and readout pulses measured by one photodiode. The horizontal dashed line shows the set threshold level for the pulse edges. The integrated intensity, start time and pulse length of each pulse are stored in the pre-analysed data. Figure and caption from [44].

3.4.6 Data acquisition

The requirements of the DAQ as discussed in Section 2.3.10, are that datastreams from multiple devices are obtained and combined into one datastream, with flexibility in time scales, and the ability of readout at the chosen shot frequency, which in this case in 10 Hz. Different accuracies of timescales are also used in the experiment and all must be able to be combined. The WLM software runs on a separate computer with its own data system that is also combined into the data stream. In this case the readouts are not yet in sync. For some devices such as the waveform generators we have both set frequencies and readouts. In that case the set frequencies are used of the spin precession analysis because of the step resolution available in the readouts. A full description of the DAQ system including the technical details has been written [44], in which all the variables that are controlled and measured are listed.

The DAQ system is built around two Versa Module Eurocard (VME) bus systems which each contain a CPU arbiter (MEN A19 VME) that combines datastreams from different devices. Local network connections send these two VME datastreams to a final DAQ PC. A Stanford Research Systems FS725 GPS stabilised Rb clock [80] serves as a time base for the entire experiment and has a stability of 10^{-12} at 1 second integration time.

Devices are readout and sent to one of the datastreams run on the CPUs that reside in the VME crates. Devices are also controlled by sending signals from the DAQ system to the devices. The final combined datastream is saved as raw data and as a pre-analysed datastream in a tree file using Cern's ROOT file structure. Normalisation and calibration of some of the signals are done in this analysis stage. Both online plotting and offline data analysis systems have been written in ROOT using C++.

A list of some of the variables saved by the data acquisition during the experiment is shown in Table 3.3. These variables are from many different devices but are saved into the same data stream for analysis.

Type	**Variable**		
PMT counts	PMT at B for normalisation	PMT at D for population probing	Background gate for PMT at D
Laser frequencies	Freq1-5		
Device timings	Scalar Counter index	Unix time	Time since start
Pulse digitisation	Timings (t, T)	Integrated intensities	
Detuning	Two photon detuning		
Frequency generator	Start and end and centre frequency	Scan timing	Number of steps
Intensities	Hyperfine pumping	Detection at B	Detection at D
Electric field	E field measured by HV supplies and switch state	HV Switch box monitoring	HV supply readout
B field	Cosine coil current (B_y)	Flux measurements	
Bitpattern generator	Experiment type and switch state	Experiment counter	Timings

Table 3.3: A list of some of the variables saved by the data acquisition system during an experiment run sorted by variable type. These variables originate from many independent devices and are combined into one data stream that can then be analysed both online and offline. The separate systems are synchronised using the 10 MHz Rb clock.

3.4.7 Experiment timing

The timings of the measurements, triggers and readouts are entirely customisable in the experiment and DAQ. In Figure 3.22, a diagram showing all the timings relevant to the experiment every repetition at 10 Hz is shown. The individual timings are for the functions as follows:

- The flash lamps and Q-switch are timing parameters that are sent to the ablation laser.
- EL-valve is the time that the Even-Levie valve is open for, in which the gas travels into the vacuum of the experiment. See Section 3.1.
- PMT B1 (Norm) shows the timings of the gate of the PMT at Region B1 of the experiment (see Figure 2.8), which collects Signal_B. See Section 3.4.2.
- PMT B2 (Ba) refers to the timing of the gate for the PMT setup in Region B2 of the setup (see Figure 2.8), which could be used in a future generation of the experiment for spectroscopy of Ba during the experiment run for frequency drift correction.
- Superposition shows the timings of the two pulses of RF signal sent to the AOMs to create the two coherent state transfer laser pulses that create and collapse the superposition of the molecules within the interaction zone.
- Pulse digitisation shows the period of time that the photodiode signals that probe the coherent state transfer laser pulse power is digitised. This signal is used to measured the pulse power and shapes. See Section 3.4.5.
- PMT D1 shows the gate timings for the PMT at Region D1 of the experiment (see Figure 2.8). Multiple gates are used to measure the time of flight of the molecules. See Section 3.4.1.
- PMT D1 background is the timings of another gate applied to the same PMT signal as in PMT D1, but set for when there are no molecules present to measure the PMT background level from scattered photons. See Section 3.4.1.
- Readouts VME011 and VME012 show the times that the data from the VME crate device is sent to the overall DAQ system to be combined with the data from the other devices. These time that this takes is of $\mathcal{O}(ms)$, and depends on the network communication speed. The requirement is that it must be completed before the next 10 Hz shot.
- Experiment update shows the time that, when required, the set parameters are updated, for example: when the E-field direction is switched. The field plates are charged with an RC time of 250 ms.

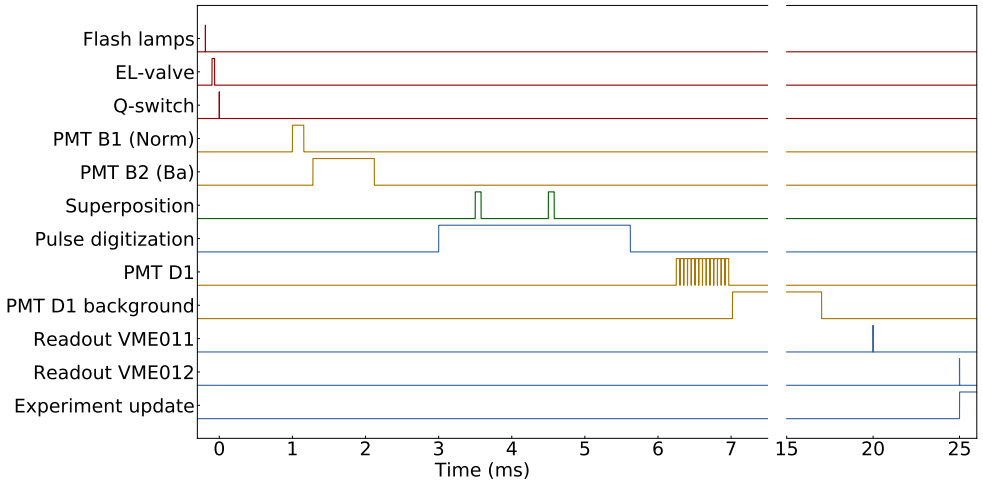

Figure 3.22: Timings of the experiment on a shot-per-shot basis. The red lines show timings used for the ablation laser process. PMT gate timings are shown with yellow lines. There are four PMT gating lines, which have delays and lengths. The PMT at D1 is gated with 14 consecutive gates of 51.2 μs each. The time of flight (TOF) is reconstructed from these gated signals. The PMT D1 background gate is 10 ms long. The superposition pulse creation and readout timings are shown in green, and the digital signals for readouts are shown in blue lines. An axis gap is shown between 7.5 and 15 ms. Timings that are not relevant to a shot-per-shot scale are not shown, and timings where only the beginning of the pulse is significant are shown as delta functions. The readouts take $\mathcal{O}$(ms). The field plates are charged with an RC time of 250 ms, which is longer than a single shot so only the start time is shown. Plot taken from [44].

3.5 Conclusion

The experimental and technical details of the optical techniques and data processing functions used in this setup have been described. Relevant optical devices, such as lasers and frequency control, have been described alongside how they are used in the experiment. The production of molecules for the eEDM experiment in a supersonic source is shown including the velocity and width of the molecular beam. The main optical systems used in the NL-eEDM experiment have been introduced and discussed, including how the population is probed, how the data is processed to remove molecule number fluctuations and background levels, and how optical pumping is implemented. A summary of the data acquisition system has been described, as well as all the timings relevant to the experiment.

Long term measurements have been performed. The frequency stability of the lasers has been shown to be better than 1 MHz in > 12 hours which is sufficient for our experiment. The flux of the molecules reduces over time which means the experiment must be reset by for example changing the ablation laser power either up or down, or moving the ablation spot on the target every ≈ 4 hours. Imperfect hyperfine optical pumping means that the $N = 0, F = 1$ ground level has some population remaining which reduces the sensitivity of the eEDM experiment. We have therefore repeated the hyperfine optical pumping process to decreases the remaining ground state $N = 0, F = 1$ population to $< 5\%$.

The setup has been built over the course of this thesis project and is now ready to undertake spectroscopy of BaF and to measure the eEDM with BaF molecules.

Chapter 4

Spectroscopy of BaF

Spectroscopy of the BaF molecule has been undertaken and the results of this will be reported on here. The vibrational, rotational and hyperfine structure of the BaF molecule is relevant for the execution of a measurement and extraction of a limit on a possible eEDM. This study addresses precise experimental determination of the hyperfine structure of states for the sensitive search for an eEDM, such as transitions which are relevant for laser cooling and readout in a spin-precession measurement [39]. These are the lowest rotational states of the $X^2\Sigma^+$ ground states and electronically excited states $A^2\Pi_{1/2}$ and $A^2\Pi_{3/2}$. In an accompanying paper the excited state hyperfine structure is compared to high-level ab initio theory calculation [43]. This chapter is in preparation for publication [81].

4.1 Previous spectroscopy work

Previous investigations employed microwave spectroscopy between rotational states $X^2\Sigma^+(v = 0, N = 0, 1, 2)$ manifold with uncertainties of order 0.04 MHz [82–84]. Hyperfine splittings for the individual rotational states were derived by comparing to a molecular Hamiltonian. BaF has been created in a cryogenic source and laser spectroscopy has resolved the ground state hyperfine structure [85]. In combination with Fourier-transform and microwave spectroscopy for $N \geq 5$ states a set of molecular constants have been extracted [83, 84]. Laser spectroscopy provided information on the electronic excitation levels with uncertainties on the order of several MHz and on Stark and Zeeman shifts [86–88]. Spin-rotational splittings in the $X^2\Sigma^+$ states were resolved while the hyperfine structure in the electronically excited state $A^2\Pi_{1/2}$ was not resolved. Recent saturated absorption spectroscopy shows the hyperfine structure for $A^2\Pi_{1/2}(v' = 0)$ with MHz uncertainty [89].

The quantitative knowledge of the vibrational, rotational and hyperfine structure of the BaF molecule is crucial for the execution of a measurement of a limit on a possible eEDM. We determined the lifetimes of the first electronically excited $A^2\Pi_{1/2}$ and $A^2\Pi_{3/2}$ states of ^{138}Ba^{19}F [42]. This study addresses the structure of these states as well as the $X^2\Sigma^+$ ground state.

4.2 Experimental setup

The supersonic source creates a pulsed BaF beam with a 10 Hz repetition rate, travelling at ≈ 600 ms^{-1} with a low transverse velocity spread [40] (see Section 3.1). The center of the beam passes through a 5 mm diameter skimmer which is mounted 28 cm from the exit valve of the gas pulses. The z axis in the lab frame is defined as the line which connects the exit valve and the centre of the skimmer.

The laser light for excitation of the molecules is provided by Titanium-Sapphire laser systems (Microlase MBR110 Ti:Saph at $780 - 850$ nm and at $840 - 990$ nm, see Section 3.2). The frequencies of the lasers are controlled by a HighFinesse WS8-2 wavelength meter (WLM) which provides for a resolution of 200 kHz and an absolute frequency accuracy over the full operational range of 2 MHz. Alternatively the frequency can be controlled by a frequency comb (Menlo Systems FC1500-250), and in that case the frequency of the beatnote of the excitation laser light with the frequency comb light is then additionally recorded. The optical power of up to mW of the laser beam is monitored after the interaction with the molecular beam by a Coherent LaserMate-Q 33-0332 power meter [90] with a silicon sensor that ranges from $400 - 1064$ nm.

In order to avoid intensity dependent broadening the light level was kept below the saturation intensity (typical intensity used was $\mathcal{O}(10 - 100\ \mu$W) per 3 mm radius beam where saturation intensity is typically few mW/cm^2). The laser induced fluorescence is collected on a H7422-50 Hamamatsu Photomultiplier (PMT) which is mounted along the y-axis of the experiment (see Figure 2.8) which is vertical in the lab frame, and therefore orthogonal to both the molecular beam and the laser beam directions. This setup provides a low-noise signal with ns time resolution [42]. An optical filter (Thorlabs FB860-10, 860 nm 10 nm transmission window, resp. FB800-40, 800 nm, 40 nm bandwidth) reduces background light reaching the PMT. The fluorescence photon rate is binned with a 25.6 μs time resolution. An optical filter (Thorlabs FB860-10, 860 nm 10 nm transmission window, resp. FB800-40, 800 nm, 40 nm bandwidth) reduces background light reaching the PMT. The power on the excitation laser, the laser frequency reading of the WLM, and a beatnote on a FGA01FC InGaAs photodiode of the excitation laser light with a frequency comb was recorded with a VME data acquisition (DAQ) (see Section 3.4.6).

The setup diagram is shown in Figure 4.1. The excitation light is delivered through one single-mode optical fibre, the input of which can be replaced with light from different lasers at various wavelengths which ensures a constant excitation geometry in the experiment. The output of the fibre is collimated to provide a beam of 3 mm diameter at the intersection with the pulsed molecular beam at Region B1 (see Figure 2.8), which is a 58 cm distance from the exit valve. The laser beam's direction is horizontal (called the x-axis in the lab frame) and is orthogonal to the molecular beam's velocity.

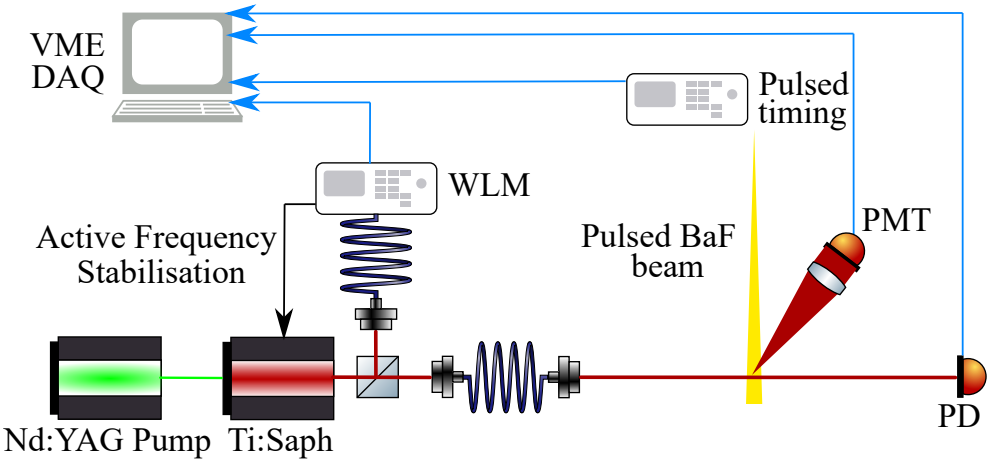

Figure 4.1: The light from a Ti:Sapphire laser is frequency stabilized by a HighFinesse WS8-2 wavelength meter (WLM), input into an optical fiber and directed to intersect with a 10 Hz pulsed BaF beam from a supersonic source [40]. The transmitted light is collected in a Coherent Lasermate-Q powermeter (PD), while fluorescence is collected with time-resolved photon counting by a photomultiplier tube (PMT). Signals from the WLM, pulse start time controller, PMT and PD are sent to the VME based data acquisition system (DAQ). The input of the fibre to the experiment can be replaced with different laser beams, allowing different transitions to be accessed while the geometry of the interaction is unchanged. Further details on the setup can be found in [39, 40].

4.3 Spectroscopy results

4.3.1 Vibrational Spectroscopy

Identifying vibrational and rotational splittings in the ground and low excited states is key in order to undertake laser cooling, which is currently being investigated in the NL-eEDM collaboration. Rotational spectroscopy has been undertaken using a laser beam scanning over more than 10 GHz for different vibrational ground and excited states. The frequencies are scanned using the internal frequency scan of the laser, while being measured by the wavelength meter.

In Figure 4.2, a selection of these scans is shown for the case $\Delta v = 0$, where multiple rotational transitions are shown for each scan. Each of the frequency axes are zeroed around the centroid of the $X^2\Sigma^+(v, N = 0) \rightarrow A^2\Pi_{1/2}(v' = v, J' = 1/2)$ transition. The centroids are the multiplicity weighted mean of the hyperfine structure. These centroids are labelled $f_{1/2,v',v}$ and their values are given in Table 4.1. The spectra are generated from the measured frequency by the WLM and number of photons recorded by the PMT during the interaction time of (start time- end time) after the recorded pulse start time. The contribution from dark counts of the PMT is negligible in these measurements (< 0.01 /ablation shot) and the rate from scattered laser light is much smaller than the resonance signal as can be observed in Figure 4.2. For each vibrational level $v + 1$ increase in Figure 4.2, the vertical axis is reduced by

half and the peak amplitudes reduce by approximately 1/3. The amplitude comes from a combination of transition strength and number of molecules in the vibrational ground state. The rotational temperature of the supersonic was previously found to be 3.5(5) K [40].

By comparing the centroid values for different $v \rightarrow v'$ transitions, the vibrational splittings in the $X^2\Sigma^+$ and $A^2\Pi_{1/2}$ states up to $v = 3$ can be extracted. These splittings are given in Table 4.2. The uncertainties of these are smaller than the centroid frequencies as there is no uncertainty from the difference to absolute frequency, unlike the centroid frequencies in Table 4.1. The measurement of the vibrational splitting between the $X^2\Sigma^+(v = 0, 1)$ states is in agreement with previous measurements [83].

Vibrational transition	Frequency Offset $f_{1/2,v1,v2}$ [MHz]
$v = 0 \rightarrow v' = 0$	348 666 427
$v = 1 \rightarrow v' = 1$	347 728 524
$v = 2 \rightarrow v' = 2$	346 787 797
$v = 3 \rightarrow v' = 3$	345 844 060

Table 4.1: Centroids of the $X^2\Sigma^+(v, N = 0, +) \rightarrow \mathrm{A}^2\Pi_{1/2}(v' = v, J' = 1/2, -)$ transition for vibrational states $v = 0 - 3$. The uncertainty (≈ 30 MHz for all levels) arises from the WLM calibration and estimates of WLM drifts over the course of the measurement.

		Vibrational Splitting T (cm^{-1})		
State	ν	This work	Previous [83]	Difference
$X\ ^2\Sigma^+$	1	465.7456(25)	465.752(2)	-0.006(3)
	2	462.1031(14)		
	3	458.4799(13)		
$A^2\Pi_{1/2}$	1	434.4638(25)		
	2	430.7207(14)		
	3	427.0002(13)		

Table 4.2: Vibrational splitting of the $X\ ^2\Sigma^+$ ground state and the $A^2\Pi_{1/2}$ excited state. Each vibrational splitting refers to the difference from the previous vibrational state, e.g. the labelling $X\ ^2\Sigma^+, \nu = 1$ here refers to the splitting from $(\nu = 0, N = 0, J = 1/2)$ to $(\nu = 1, N = 0, J = 1/2)$.

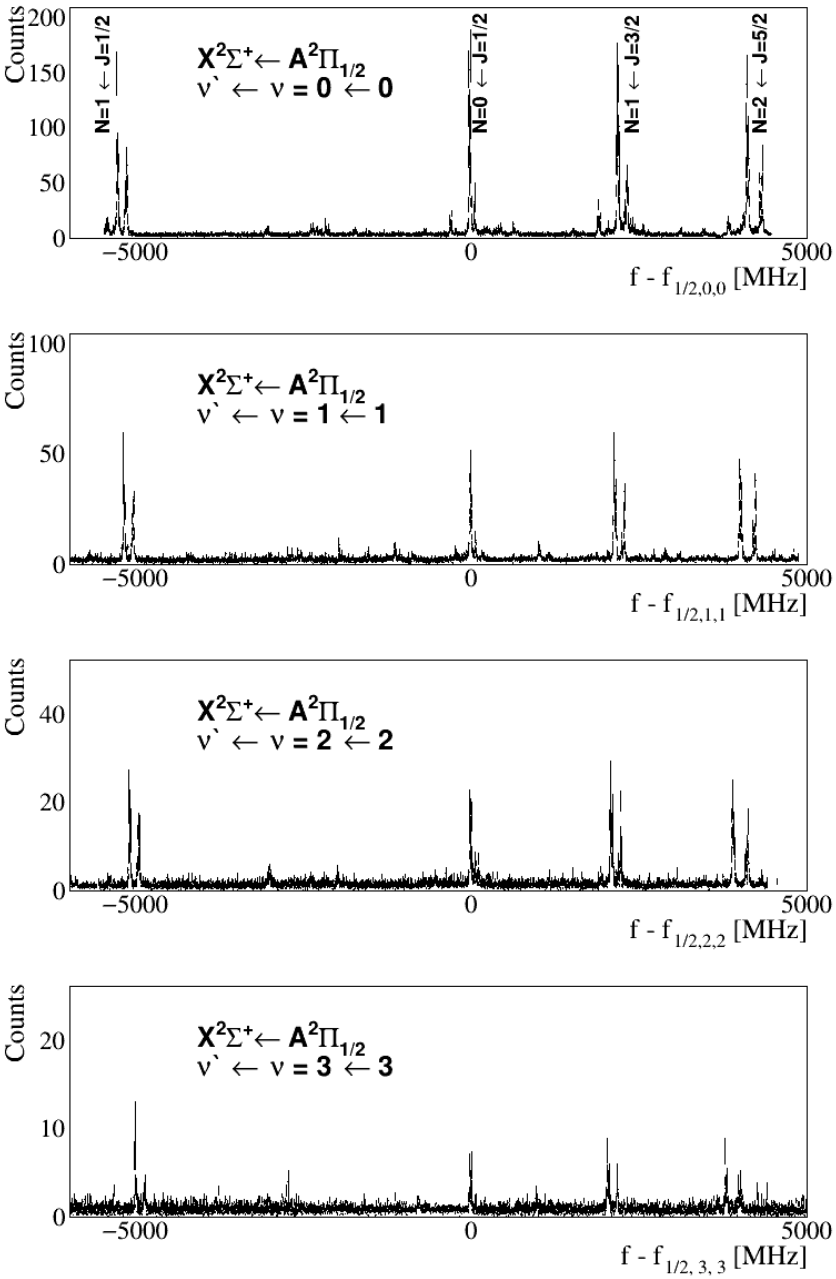

Figure 4.2: The $X^2\Sigma^+ \rightarrow A^2\Pi_{1/2}$, $\Delta v = 0$ transition for different vibrational states v. The frequency axis is the offset to the $N = 0 \rightarrow J' = 1/2$ centroid frequency for the $^{138}Ba^{19}F$ for the respective vibrational transition. The smaller unassigned resonances are due to the presence of natural abundant stable barium isotopes, in addition to ^{138}Ba in our ablated target. The vertical scale of the counts per molecular pulse is reduced by a factor 2 for each plot from top to bottom.

4.3.2 Hyperfine Spectroscopy

In order to extract the hyperfine splittings with sub-MHz precision, shorter and slower frequency scans have been undertaken with a frequency range of a few 100 MHz, or enough to cover the hyperfine components of the ground and excited state for each transition. The frequency is controlled and measured by the wavelength meter.

Hyperfine spectroscopy was conducted for various transitions from the $X\ ^2\Sigma^+(v = 0-2, N = 0-7)$ ground state levels, with resolved excited state hyperfine structure for the $A^2\Pi_{1/2}(v' = 0-2, J' = 1/2(-)\ -3/2(-))$ and $A^2\Pi_{3/2}(v = 0, J = 3/2(-)\ -5/2(-))$ excited states. A selection of typical spectra are shown in Figures 4.4 and 4.5, and relevant parts of corresponding energy level diagrams for the spectra shown in (a) of each of these plots are shown in Figure 4.3.

No background subtraction or normalisation has taken place in the shown plots Figures 4.4 and 4.5. The power of the laser beam used was minimised such that power broadening was not observable in each spectrum, which is typically less than 10% of the saturation intensity. For (b) of Figure 4.5, the power was higher to observe the spectrum for the higher N state that is less populated, which leads to a higher background rate. The intensity was not recorded in the data. The narrow spread of the velocity of the supersonic source means that there is a Doppler broadening that gives a Gaussian linewidth of < 3 MHz. The linewidths of the resonances are therefore close to the natural linewidth of each transition, which is a few MHz.

Each spectrum is plotted using the profile histogram function from [66]. Multiple frequency scans are averaged. The mean value of the counts/pulse and its RMS value for each frequency bin is plotted as the error bar. The uncertainty of the counts arises from averaging statistical fluctuations that come from the supersonic source. The bin sizes are shown as the error bars on the data points on the frequency axes.

In order to extract the hyperfine structure from the measurements, the resonance frequencies of the transitions were determined from fitting a model function against the data. Each hyperfine component is independently described by the Voigt function in the TMath package of ROOT [66], which is a convolution of a Gaussian distribution and a Lorentzian function. The amplitudes and the homogeneous linewidths are independently fitted, while the inhomogeneous linewidth has one parameter. The excited state hyperfine structure is fitted as one parameter, as it can appear multiple times as a part of other splittings. In this way, all the hyperfine components are independent variables that are included as part of the fitting parameters. The extracted splittings are given in Section 4.4.

The $X^2\Sigma^+ \rightarrow A^2\Pi$ transitions can exhibit up to seven lines due to the hyperfine splitting in the ground and excited states, and the selection rules. Excited state hyperfine structures are directly resolvable up to $J' = 5/2(-)$. In Figure 4.4 (a), the hyperfine structure of the excited state is clearly resolveable and three distinct lines are observed in the spectrum. In this case there are only three lines rather than seven because of the selection rules, and because the ground state only has the two $J = N + 1/2$ levels as $N = 0$.

For each $N > 0$ state, there are two F states with the a value $F = N$ which are mixed. For the particular case of the $X^2\Sigma^+(v = 0, N = 2, +) \rightarrow A^2\Pi_{1/2}(v' = 0, J = 1/2, -)$

transition, which is shown in Figure 4.4 (b) the two $F = 2$ states within each J-level are coupled resulting in a superposition of pure J states with admixtures defined by

$$\begin{aligned}(J = 3/2, F = 2) = \\ &\alpha(J = 3/2, F = 2) \\ &+ \beta(J = 5/2, F = 2),\end{aligned} \tag{4.1}$$

and

$$\begin{aligned}(J = 5/2, F = 2) = \\ &- \beta(J = 3/2, F = 2) \\ &+ \alpha(J = 5/2, F = 2),\end{aligned} \tag{4.2}$$

with the coefficients $\alpha = 0.9858$ and $\beta = 0.1679$ [91]. This effect can be observed in Figure 4.4 (b) as the smaller amplitude peak at around -38880 MHz.

For larger J' the hyperfine splitting of the excited $A^2\Pi_{1/2,3/2}$ states becomes smaller than the natural linewidth. Furthermore, we observe that, with increasing J, intensities of transitions with $\Delta F \neq \Delta J$ decrease with respect to transitions with $\Delta F = \Delta J$ as has been previously observed in spectroscopy (for example, in [92, 93]) which is sometimes called an approximate selection rule. This is shown in Figure 4.3 by drawing thicker lines for the stronger transitions. The amplitudes of the transitions also depend on the multiplicity of the F ground state. In the case of high $N \rightarrow J'$ transitions, (i.e.: $J' > 3/2-$) only these four strong lines will be resolveable.

Part (a) of Figure 4.5 shows the transition from $X^2\Sigma^+(v = 0, N = 1, -) \rightarrow A^2\Pi_{1/2}(v' = 0, J' = 3/2, +)$, where 7 resonances are observed. The hyperfine structure of the excited state is now less than the width of the transition, leading to the overlap of the resonances observed in the plot. In addition, the so-called approximate selection rule $\Delta F = \Delta J$ [93] has become more relevant and the transitions that do not follow this rule are smaller in amplitude than the ones that do. The smaller ones are observed as 'shoulders' on the larger resonances, and the precision of the spectroscopy means that the hyperfine structure can be extracted using a fitting model.

Part (b) of Figure 4.5 shows the $X^2\Sigma^+(v = 0, N = 7, -) \rightarrow A^2\Pi_{1/2}(v' = 0, J' = 13/2, -)$ transition. For this high J-level in the excited state, the hyperfine structure is too small to resolve and the approximate selection rule applies, so we only observe 4 resonances instead of 7. Additional structure is observed between -27200 and -27000 MHz, which is from particles (other than ^{138}BaF) present in the beam having been ablated from the target of the supersonic source.

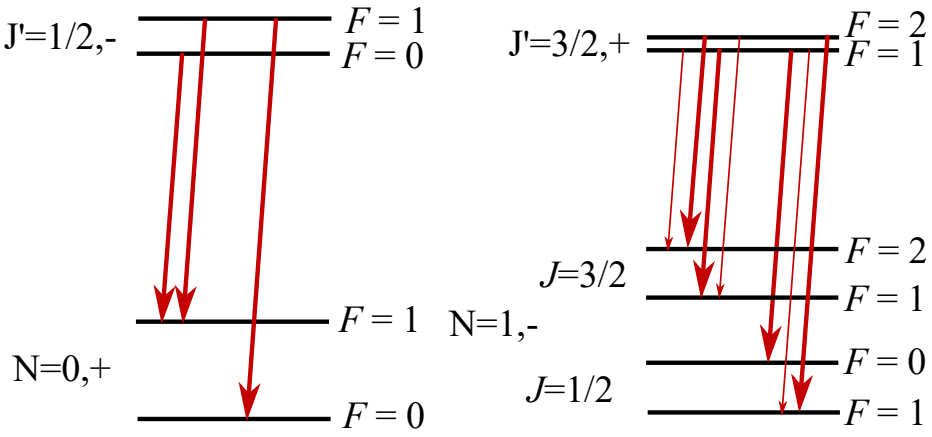

Figure 4.3: Energy level diagrams between the $X^2\Sigma^+(v = 0) \rightarrow A^2\Pi_{1/2}(v' = 0)$ rotational levels. Not to scale. Left: Energy level diagram for the transition shown in Figure 4.4 (a).
Right: Energy level diagram for the transition shown in Figure 4.5 (a), where the selection rules and hyperfine structure mean that 7 transitions are allowed. The stronger transitions due to the approximate selection rule $\Delta J = \Delta F$ are shown by a thicker transition line.

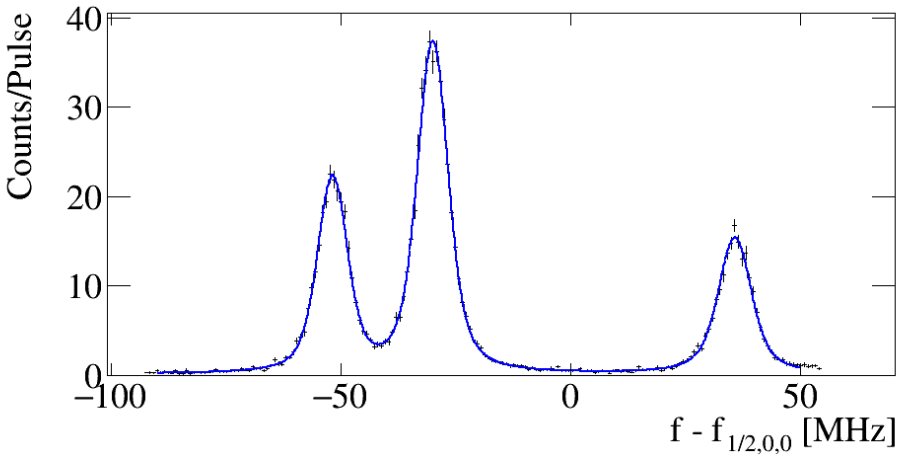

(a) $v = 0, N = 0, + \rightarrow v' = 0,\ J' = 1/2, -$

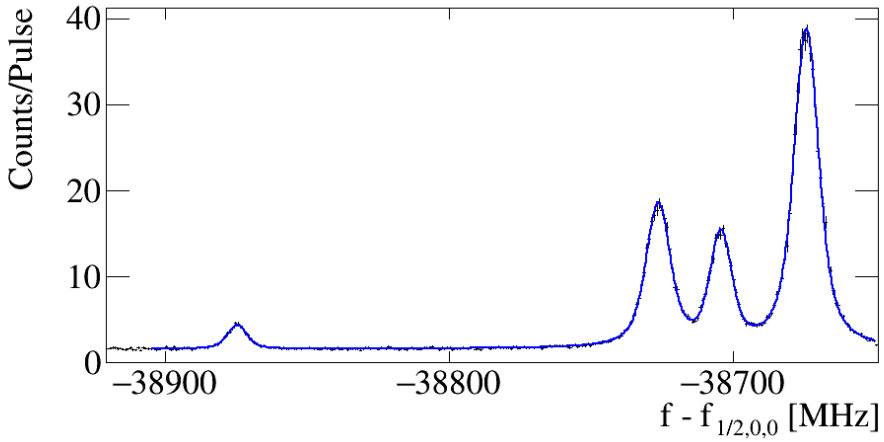

(b) $v = 0,\ N = 2, + \rightarrow v' = 0,\ J' = 1/2, -$

Figure 4.4: Spectra of $X^2\Sigma^+ \rightarrow A^2\Pi_{1/2}$ transitions. A model function (blue line) which describes each hyperfine component is fitted to the data (see Section 4.3.3). In black is a profile histogram of the count rate of fluorescence per 10 Hz pulse. Each frequency axis is offset from the $X^2\Sigma^+(v = 0, N = 0, +) \rightarrow \mathrm{A}^2\Pi_{1/2}(v' = 0, J' = 1/2, -)$ transition. The splittings extracted from plots such as these are shown in Tables 4.3 and 4.4. In (a) the laser frequency was controlled using a Frequency Comb. The energy level diagram can be found in Figure 4.3. For (b) the laser frequency was controlled by the WLM. The peak at around -38880 MHz is observed because of mixing of levels with the same F within a rotational N level.

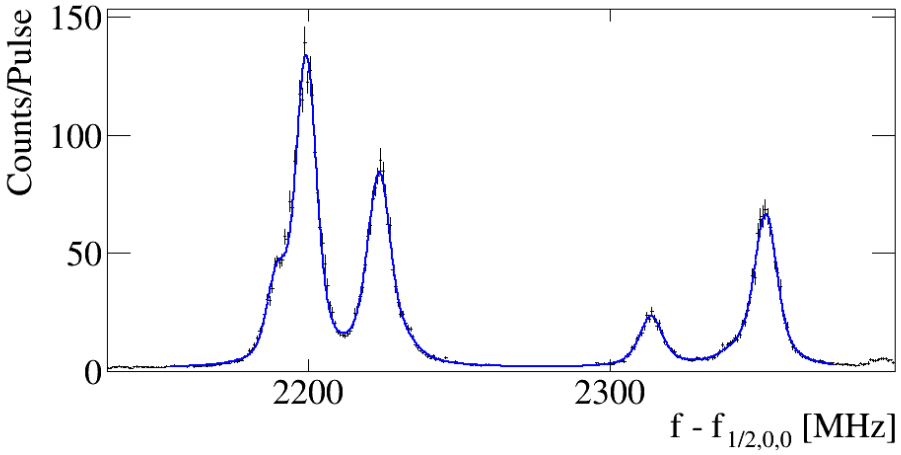

(a) $v = 0, N = 1, + \rightarrow v' = 0,\ J' = 3/2, -$

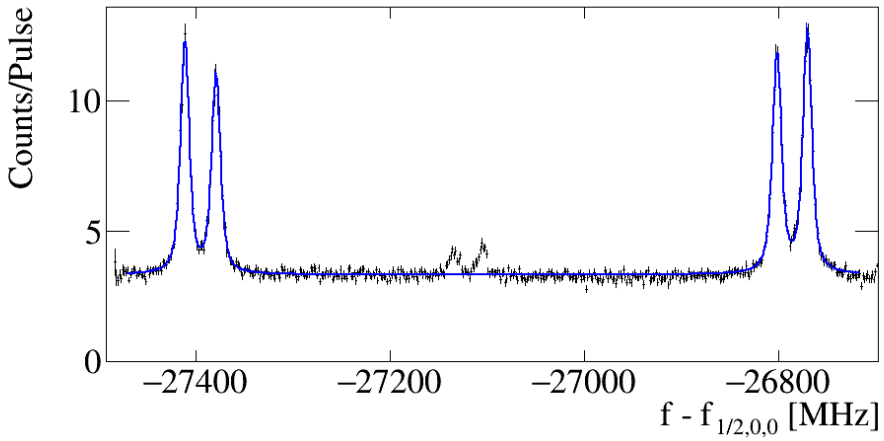

(b) $v = 0,\ N = 7, + \rightarrow v' = 0,\ J' = 13/2, -$

Figure 4.5: Spectra of $X^2\Sigma^+ \rightarrow A^2\Pi_{1/2}$ transitions. A model function (blue line) which describes each hyperfine component is fitted to the data. The splittings extracted are shown in Tables 4.3 and 4.4. In black is a profile histogram of the count rate of fluorescence per 10 Hz pulse. Each frequency axis is offset from the $X^2\Sigma^+(v = 0, N = 0, +) \rightarrow A^2\Pi_{1/2}(v' = 0, J' = 1/2, -)$ transition. The energy level diagram for (a) can be found in Figure 4.3. Comparing (a) and (b) shows how as the ground state N increases, the splitting between the two peak groups becomes larger. In addition, as J in the excited state increases, the hyperfine splitting becomes smaller and the amplitude of the $\Delta J \neq \Delta F$ transitions decreases, so instead of 7 resonances, only 4 can be observed. In (a) the inter-J splitting is also smaller due to the smaller N.

4.3.3 Model Function

In order to extract the hyperfine structure from the measurements, the resonance frequencies of the transitions were determined from fitting a model function against the data. Each hyperfine component is independently described by a Voigt profile L_i [94], which is a convolution of a Gaussian distribution $\mathrm{G}(x, \sigma)$ and a Lorentzian function $\mathrm{L}(x, \gamma_\mathrm{L})$. $\mathrm{G}(x, \sigma)$ is inhomogeneous broadening due to the transverse velocity spread of the molecules and $\mathrm{L}(x, \gamma_\mathrm{L})$ is the homogeneous width of the transition. The normalised form of $\mathrm{G}(x, \sigma)$ is given by

$$\mathrm{G}(x, \sigma) = \frac{e^{-x^2/2\sigma^2}}{\sigma\sqrt{2\pi}}, \tag{4.3}$$

where x in this general case is the detuning from the centre of the peak, and σ is the Gaussian width. The general form of $L(x, \gamma_\mathrm{L})$ is given by

$$\mathrm{L}(x, \gamma_\mathrm{L}) = \frac{\gamma_\mathrm{L}}{2\pi(x^2 + \gamma_\mathrm{L}^2/4)} \tag{4.4}$$

where here γ_L is the Lorentzian width. The convolution of these two for each line L_i is defined as

$$L_i = \mathrm{Voigt}(\gamma_\mathrm{L}, \sigma, f_{c,i}, A_i). \tag{4.5}$$

where the Voigt profile depends on the Lorentzian and Gaussian widths γ_L and σ, the centre frequency for each peak $f_{c,i}$, and the area under the curve for each peak A_i. The area under the curve and the homogeneous γ_L are independently fitted, while the inhomogeneous σ linewidth has one parameter that is used for all the resonances because the Doppler broadening is the same for all resonances of a transition. The excited state hyperfine frequency splitting is fitted as one parameter, as it can appear multiple times as a part of other splittings. In this way, all the hyperfine components are independent variables that are included as part of the fitting parameters. The spectrum is the sum over the number of different hyperfine components:

$$\text{Model function} = \Sigma_{i=1}^{N}(L_i) + \text{offset} \tag{4.6}$$

where N can be between 3 and 7 depending on the transition and the offset is the background rate on the detector. The (up to) four splittings shown in the tables for each spectrum at the end of this chapter are calculated from the differences in the centre frequencies.

4.3.4 Uncertainty of the fitted hyperfine splittings

The uncertainty in the determination of the spectral lineshape has contributions from shot noise of the detected number of fluorescence photons, variations in the number of molecules due to properties of the ablation process, and the determination of the frequency of the excitation light. The statistical resolution for the determination of hyperfine splitting of the ground and excited state was typically 100 kHz. The frequency accuracy with the frequency comb was better than 10^{-11} for a 100 ms integration time [95].

The performance of WLMs similar to the employed HighFinesse WS8-2 has been reported [68, 69]. This results in a few MHz uncertainty for frequency intervals larger than several GHz and a differential non-linearity of less than 1 MHz /200 MHz for intervals below the GHz level. In addition, the use of the supersonic source means that other molecules and atoms are present in the molecular beam, which can undergo transitions at similar frequencies to the transitions of interest, as shown in Figure 4.5 b. Transitions that overlap with the measured peak will shift the frequencies we measure with the fitting procedure.

4.4 Extracted hyperfine splittings

The hyperfine splittings that have been extracted for $^2\Sigma^+ \rightarrow A^2\Pi_{1/2}(\Delta v = 0)$ transitions are collected in Tables 4.3 and 4.4 and ordered by the transition they were extracted from. The labelling of the splittings used in the tables is shown in Figure 4.6. We resolve the hyperfine structure of the excited state up to $A^2\Pi_{1/2}(v' = 1, J' = 3/2, -)$. In Table 4.3, the transitions for which the excited state could be optically resolved are shown. The splittings from transitions with optically unresolved excited state hyperfine structure are shown in Table 4.4. In the fitting procedure, the hyperfine structure of the excited state has been set to be 0 for these transitions. The extracted splittings for the $^2\Sigma^+ \rightarrow A^2\Pi_{1/2}(\Delta v = 0)$ transition is shown in Table 4.5. In Appendix C, the spectra of all the transitions listed in these tables are shown.

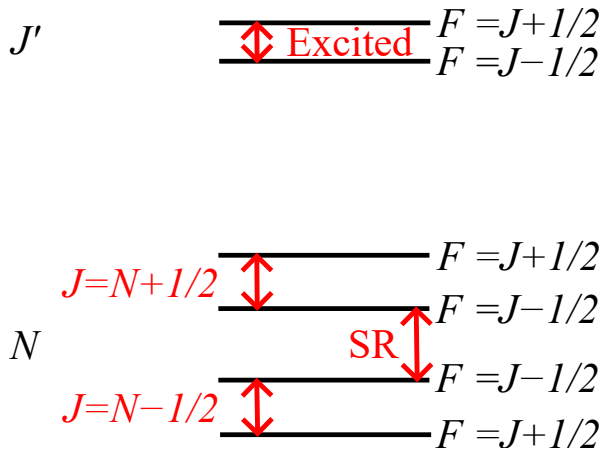

Figure 4.6: Generic energy level diagram for a transition from the $^2\Sigma^+(v, N)$ ground state to the $A^2\Pi_{1/2}(v', J')$ or $A^2\Pi_{3/2}(v', J')$ excited state. Red: the four splittings extracted from each spectrum that are given in Tables 4.3 and 4.4. There are three splittings in the ground state: the two intra-J splittings and the inter-J splitting that comes from the spin rotation coupling (SR). In the excited state there are only two lines so there is one splitting.

$^2\Sigma^+$	$A^2\Pi_{1/2}$	Splitting (MHz)					
v, N	J', p	J=N-$\frac{1}{2}$	SR	J=N+$\frac{1}{2}$	Excited	χ^2_{red}	Fig.
0, 0	1/2, −			65.86(11)	21.53(17)	1.6	C.1(a)
0, 0	1/2, −			65.71(11)	22.00(17)	1.7	C.1(b)
0, 1	1/2, +	28.1(3)	90.1(4)	34.5(1)	17.43(17)	1.6	C.2(a)
0, 1	1/2, +	27.8(4)	90.4(4)	34.16(13)	16.97(19)	1.3	C.2(b)
0, 1	3/2, +	28.1(2)	89.99(18)	34.3(2)	9.7(4)	1.8	C.3(a)
0, 1	3/2, +	28.1(2)	90.12(15)	34.13(16)	9.8(2)	1.7	C.3(b)
0, 1	3/2, +	28.3(2)	89.96(16)	35.03(18)	9.8(3)	1.9	C.3(c)
0, 2	1/2, −	30.2(1)	170.36(14)		22.06(7)	1.0	C.4(a)
0, 2	1/2, −	30.28(13)	170.4(3)		21.96(15)	1.2	C.4(b)
0, 2	3/2, −	28.4(7)	168.6(7)	34.7(4)	7.6(5)	1.3	C.5(a)
0, 2	3/2, −	27.5(6)	169.4(6)	35.2(3)	8.0(1.2)	1.5	C.5(b)
0, 2	3/2, −	26.9(5)	169.7(4)	35.5(3)	8.3(5)	1.5	C.5(c)
0, 2	3/2, −	28.7(6)	168.3(6)	34.9(4)	7.8(5)	1.3	C.5(d)
0, 2	3/2, −	27.8(9)	169.6(1.0)	33.9(4)	7.2(8)	1.3	C.5(e)
1, 1	1/2, +	26.6(7)	91.7(7)	34.1(2)	17.2(3)	1.3	C.7
1, 1	3/2, +	27.9(4)	90.6(5)	32.8(4)	9.0(5)	1.3	C.8
1, 2	3/2, −	29.9(1.3)	167.4(1.2)	34.7(3)	7.6(8)	1.3	C.9

Table 4.3: The extracted splittings and their uncertainties from fitting the model function as described in Section 4.3.3, organised by transition. For example, the first line shows the $^2\Sigma^+(v = 0, N = 0) \rightarrow A^2\Pi_{1/2}(v = 0, J' = 1/2, -)$ For these transitions, the excited state hyperfine structure is resolvable. The given uncertainties have been scaled using the reduced ${\chi_{\text{red}}}^2$. Each splitting also has an additional systematic uncertainty from the wavelength meter of 0.1 MHz per 20 MHz as discussed in Section 4.3.4. The splittings are all given under the subheading ΔF and the first three of these columns refer to the three splittings of the ground state, where SR is the spin rotation splitting or the inter-J splitting (see Figure 4.6). For the $N = 0$ ground level, there is only one splitting because there are only two F levels rather than four. For the $N = 2 \rightarrow J = 1/2$ transition, the $J = N + 1/2$ splitting is not probed. The final splitting column shows the hyperfine splitting of the probed level of the $A^2\Pi_{1/2}$ excited state. All transitions are $\Delta v = 0$ transitions. A selection for transitions have been probed multiple times to show the repeatability of the experiment in different conditions.

$^2\Sigma^+$	$A^2\Pi_{1/2}$	Splitting (MHz)					
v, N	J', p	J=N-$\frac{1}{2}$	SR	J=N+$\frac{1}{2}$	Excited	χ^2_{red}	Fig.
0, 2	5/2, −	29.3(2)	170.2(3)	33.4(3)	-	1.5	C.6(a)
0, 2	5/2, −	29.48(17)	170.0(3)	33.7(3)	-	1.7	C.6(b)
0, 2	5/2, −	29.2(3)	170.4(3)	33.9(3)	-	1.8	C.6(c)
0, 2	5/2, −	29.1(3)	170.9(3)	32.6(3)	-	1.8	C.6(d)
0, 3	5/2, +	32.78(16)	250.18(17)	28.76(17)	-	0.9	C.10
0, 3	7/2, +	36.02(17)	249.91(18)	28.46(16)	-	1.5	C.11(a)
0, 3	7/2, +	35.98(13)	250.98(12)	28.35(11)	-	1.0	C.11(b)
0, 4	7/2, −	32.47(11)	334.50(12)	30.63(12)	-	1.3	C.12
0, 7	13/2, +	31.2(2)	577.1(2)	32.1(2)	-	2.2	C.13
1, 4	9/2, −	34.0(1.0)	328.4(1.1)	29.5(1.3)	-	2.1	C.14
1, 5	11/2, +	34.3(9)	414.0(7)	25.5(7)	-	0.9	C.15
1, 6	13/2, −	33.8(6)	496.5(1.3)	29.7(1.5)	-	1.1	C.16
2, 3	5/2, +	32.3(5)	249.5(5)	29.7(4)	-	1.2	C.17
2, 4	7/2, −	32.0(5)	331.5(5)	30.1(4)	-	0.9	C.18

Table 4.4: The extracted splittings and their uncertainties from fitting the model function as described in Section 4.3.3, organised by transition. For these transitions, the excited state hyperfine structure is not resolvable in the spectra so the parameter in the model function has been set to be equal to 0 in the fitting regime. The given uncertainties have been scaled using the reduced ${\chi_{\text{red}}}^2$. Each splitting also has an additional systematic uncertainty from the wavelength meter of 0.1 MHz per 20 MHz as discussed in Section 4.3.4. The splittings are all given under the subheading ΔF and the first three of these columns refer to the three splittings of the ground state, where SR is the spin rotation splitting or the inter-J splitting. $N \pm 1/2$ For the $N = 0$ ground level, there is only one splitting as it has only two F hyperfine levels. For the $N = 2 \rightarrow J = 1/2$ transition, the $J = N + 1/2$ splitting is not probed. The final splitting column shows the hyperfine splitting of the probed level of the $A^2\Pi_{1/2}$ excited state. All transitions are $\Delta v = 0$ transitions. A selection for transitions have been probed multiple times to show the repeatability of the experiment in different conditions.

$^2\Sigma^+$	$A^2\Pi_{3/2}$	Splitting (MHz)					
v, N	J', p	$J = N - \frac{1}{2}$	SR	$J = N + \frac{1}{2}$	Excited	χ^2_{red}	Fig.
0, 0	3/2, −			65.85(5)	19.14(4)	1.8	C.19
0, 1	3/2, +	27.9(2)	89.0(2)	34.4(2)	18.8(1)	2.8	C.20
0, 2	5/2, −	30.57(6)	169.22(4)	33.11(6)	12.19(5)	1.5	C.21

Table 4.5: The extracted splittings and their uncertainties from fitting the model function as described in Section 4.3.3, organised by transition. For these transitions, the excited state hyperfine structure is resolvable. The given uncertainties have been scaled using the reduced ${\chi_{\text{red}}}^2$. Each splitting also has an additional systematic uncertainty from the wavelength meter of 0.1 MHz per 20 MHz as discussed in Section 4.3.4. The splittings are all given under the subheading ΔF and the first three of these columns refer to the three splittings of the ground state, where SR is the spin rotation splitting or the inter-J splitting (see Figure 4.6). For the $N = 0$ ground level, there is only one splitting because there are only two F levels rather than four. The final splitting column shows the hyperfine splitting of the probed level of the $A^2\Pi_{3/2}$ excited state. All transitions are $\Delta v = 0$ transitions. Some of the same splittings are shown in Tables 4.3 and 4.4 for different transitions.

4.4.1 Ground state $X^2\Sigma^+(v = 0, N = 0, +)$ hyperfine structure

For an eEDM search with BaF, the ground state is of particular interest [46]. For the $X^2\Sigma^+(v = 0, N = 0, +) \rightarrow \text{A}^2\Pi_{1/2}(v' = 0, J' = 1/2, -)$ transition, the frequency of the laser light was controlled using the frequency comb, and measured using the WLM. The ground state hyperfine structure was measured to be 65.86(11) and 65.71(11) MHz (see Table 4.3) when scanning the frequency comb up or down in frequency respectively. Figure 4.4 (a), shows one of these spectra. The differential non-linearity of the WLM (see Section 4.3.4) for the two scans is shown in Figure 4.7 to be of $\mathcal{O}(100\text{ kHz})$ over a 100 MHz range. The same ground state hyperfine splitting was also measured using the $X^2\Sigma^+(v = 0, N = 0, +) \rightarrow \text{A}^2\Pi_{3/2}(v' = 0, J' = 3/2, -)$ transition to be 65.85(5) MHz as shown in Table 4.5. The value previously reported in literature is 66.25(4) MHz [24, 82], but has not been directly measured.

Precise RF signals used to couple the ground state hyperfine $N = 0,\ F = 0, 1$ levels are described in Chapter 5 and [18, 46]. This technique is not affected by the systematic effects of the WLM or additional structure from other atoms or molecules with similar transition frequencies. In Section 5.4.2, the hyperfine splitting is measured to be 65.848714(40) MHz, in excellent agreement with our laser spectroscopy results.

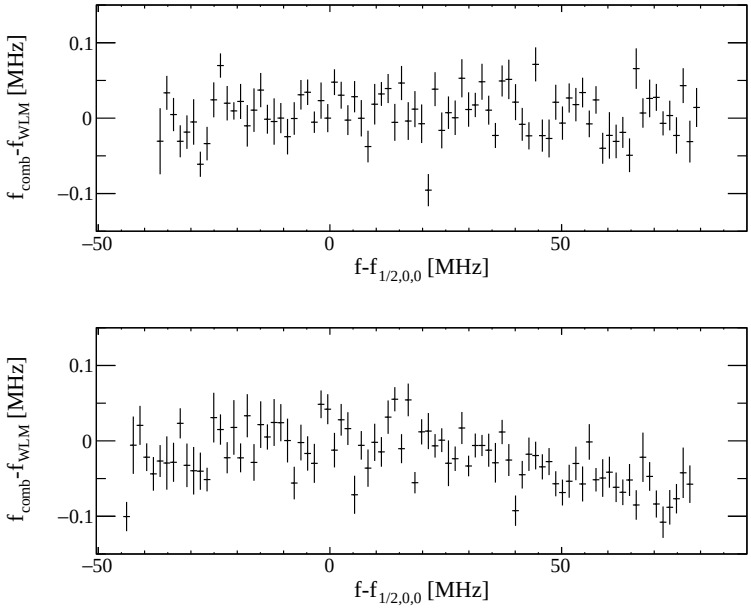

Figure 4.7: The differential non-linearity of the WLM is shown over a 200 s frequency scan by controlling the laser frequency with the frequency comb and measuring it with the wavelength meter. The difference between the set value and the readout of the WLM is plotted against the WLM frequency. The error bars on the horizontal axis are the bin size of the data plotted. The error bars on the vertical axis arise from the readout resolution of the WLM (200 kHz). These frequency scans were recorded while acquiring spectra Figures C.1(a) and C.1(b) respectively. The deviation over the frequency scan is shown to be less than 100 kHz. This systematic effect on the hyperfine structure is consistent with the values given in Tables 4.3 to 4.5. Data taken on the 19th November 2020.

4.5 Conclusion

Laser spectroscopy of BaF molecules with enough spectral resolution to observe hyperfine splittings in ground and excited states provided accurate information on the energy levels and transitions which are employed in an experiment searching for a permanent eEDM. We demonstrate that the use of a Frequency Comb or redundant measurements overcomes possible systematic effects originating from the WLM frequency control.

Essential vibrational and rotational splittings have been extracted for states required in laser cooling. The supersonic beam and low background light collection setup permits analysis on different energy scales, resulting in improved resolution on the vibrational, rotational and fine structure and optically resolved hyperfine structure in the ground and excited states. An excellent agreement is found with previous determinations of the vibrational structure [83, 86]. The transitions were observed for different vibrational states $v = 0, 1, 2, 3$ and rotational state $N = 0, 1, 2$, which is shown in Figure 4.2 for several $\Delta v = 0$ transitions. The ground and excited state vibrational splittings between v levels are extracted from measurements of $\Delta v = 0$ with $\Delta v = \pm 1$ transitions (Table 4.2). The transition frequencies between the centroids of the $A^2\Pi_{3/2}(v' = v, J' = 1/2, -)$ and the $X^2\Sigma^+(v, N = 0, +)$ states have been extracted and are shown in Table 4.1.

The hyperfine and inter-J splittings obtained from transitions between many rotational levels between the $X^2\Sigma^+(v, N)$ ground state and the $A^2\Pi_{1/2}(v' = v, J')$ excited state levels are shown in Tables 4.3 and 4.4. In Table 4.5, the hyperfine and inter-J splittings from transitions between a sample of rotational levels of the $X^2\Sigma^+(v, N)$ ground state and $A^2\Pi_{3/2}(v', J')$ excited state. The extracted parameters are now known sufficiently accurately for the needs of the NL-eEDM experiment.

Chapter 5

Using spin precession to map systematic effects

The NL-eEDM experiment depends on a coherent state transfer between the $|F = 0\rangle$ and the $|F = 1, m_F = \pm 1\rangle$ sublevels of the $|N = 0\rangle$ ground state that is undertaken entirely optically. The essence of this technique is that not only can the eEDM be extracted, but possible systematic effects are individually identified and quantified within the same experiment as previously discussed in [46].

In this chapter, the building blocks described in Chapter 2 to create an eEDM are integrated with the specifics of the optical experimental design (see Chapter 3) to create a working eEDM experiment. We discuss the experimental results of the optical coherent state transfer with and without the use of the interaction zone to create a homogeneous magnetic and electric field environment. The extraction of possible systematic effects is shown and the route to an eEDM extraction using this technique is shown. The effect of the orientation and magnitude of magnetic fields on the energy levels that are probed and the subsequent Zeeman shifts are investigated without the magnetic shield. A wide range of frequencies both below and above the transition frequency for a single-photon transition were probed in order to investigate the light shift effects on the two-photon transition frequency.

With the addition of the interaction zone, longer coherence times of up to $T = 2$ ms can be achieved. The use of a model function to compare the experimental results to the calculations using the optical Bloch equations is explained [45, 46].

For the many parameters of the experiment, ideal working points have been established through measurement. These working points were then changed in order to understand the dynamics of the possible systematic effects in the experiment. Various examples of this are given such as pulse lengths, intensities, and electric and magnetic fields.

5.1 Features of two-photon transitions without the interaction zone

Careful control over the magnetic and electric field magnitude and orientation has been achieved using the interaction zone, as discussed in Sections 2.3.6 and 2.3.7. Without this device, the Zeeman shifts cause the $m_F = \pm 0, 1$ sublevels of the $F = 1$ hyperfine level to be split. In the case of a parallel magnetic field to the laser beam's direction of propagation, the $m_F = 0$ sublevel will be included in the superposition created by the two-photon transition. In order to characterise these effects, a coherent state transfer experiment was performed without the interaction zone such that magnetic fields could be applied without magnetising the magnetic shielding itself. The results demonstrate why an interaction zone is required. Large Zeeman splittings are investigated and the effect of magnetic field orientation on the population of the sublevels are shown.

In Region B1, electric field plates have been installed and the population in the $X^2\Sigma^+(v = 0, N = 0, +, F = 1)$ level is probed in Region B2. The electric field was set to be 0 V/cm. The setup diagram (Figure 5.1) does not include the coils used to apply a magnetic field in the probed region. Unlike the current setup shown in Figure 2.8, in this case the coherent state transfer was applied using laser light beams perpendicular to the molecular pulse's velocity.

The use of an aperture limits the effective pulse length time ($t \approx \mu$s) in comparison to what is achieved with the interaction zone, and because the superposition precession takes place over a $\mathcal{O}$(mm), field inhomogeneity is not as important. These experiments explore the energy level shifts that take place due to a combination of Zeeman and (tensor) Stark effects. A description of how the three $|F = 1, m_F = -1, 0, +1\rangle$ sublevels are affected in a combination of electric and magnetic fields is given in [45].

5.1.1 Observation of Zeeman splitting

Large enough magnetic fields to produce MHz level $m_F = \pm 1$ sublevel splittings have been applied and the results are shown in Figure 5.2. The magnetic field has been created with orientation control [18]. In the case of applying a magnetic field B_y, which is perpendicular to both the velocity of the molecular beam and the horizontal laser fields, the Zeeman splitting is observed.

The orientation of the magnetic fields in comparison to electric field and molecular beam direction matters as well as the magnitudes of the fields. In the case that a magnetic field is only applied in the direction B_x (see Figure 5.3), which is parallel to the laser beams used for the two-photon transition and the population probe, Zeeman splitting between these states is not observed due to the directional dependence of the Zeeman effect [97], which is shown in Figure 5.3. This means that the magnetic field directions are as perpendicular as we can measure with this method. Coherence is shown by the widths of the peaks which is limited by $1/(2\pi t)$.

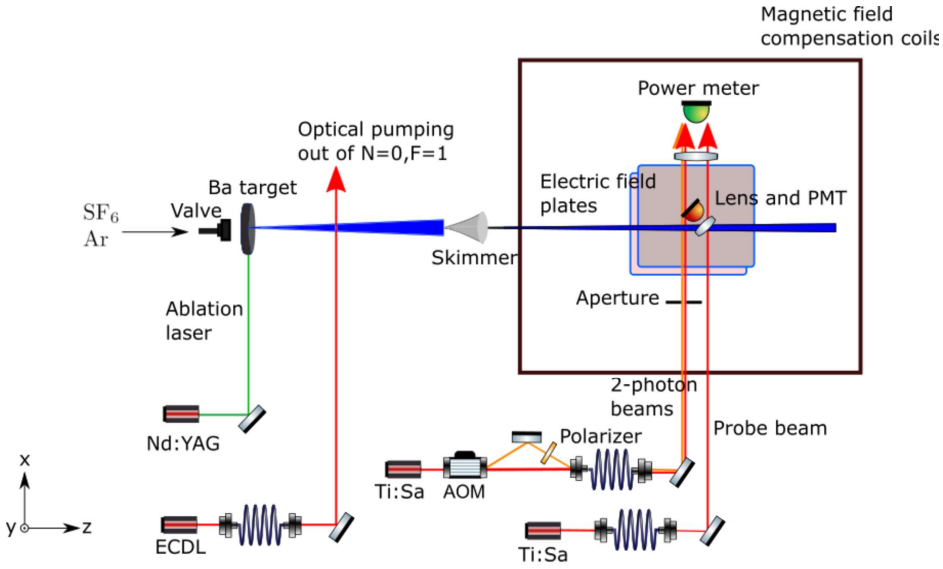

Figure 5.1: Diagram of setup for performing coherent state transfer in electric and magnetic fields in Region B of the experiment from a previous version of the NL-eEDM experiment. Molecules are created in a supersonic source (Region A1) and undergo optical pumping out of the $X^2\Sigma^+(v=0, N=0, +, F=1)$ ground sublevel (Region A2). The centre of the molecular beam passes through a skimmer and enters the field region with electric field plates. Two CW laser beams with a frequency difference (sideband detuning) close to the hyperfine splitting between $F=0,1$ are overlapped. The combined laser beam passes through an aperture such that the beam is only 1 mm diameter and intersects perpendicularly with the molecular beam (Region C). Within the same region, the population is probed using a laser beam within the electric fields plates via a different electronic excited state to the two-photon laser light frequency. LIF is collected using a lens and PMT setup with a direction perpendicular to both the molecular beam direction and the laser light's direction. The light used to undertake the two-photon transition is blocked from reaching the PMT by an optical filter. Figure taken from Rozeboom's master's thesis [96].

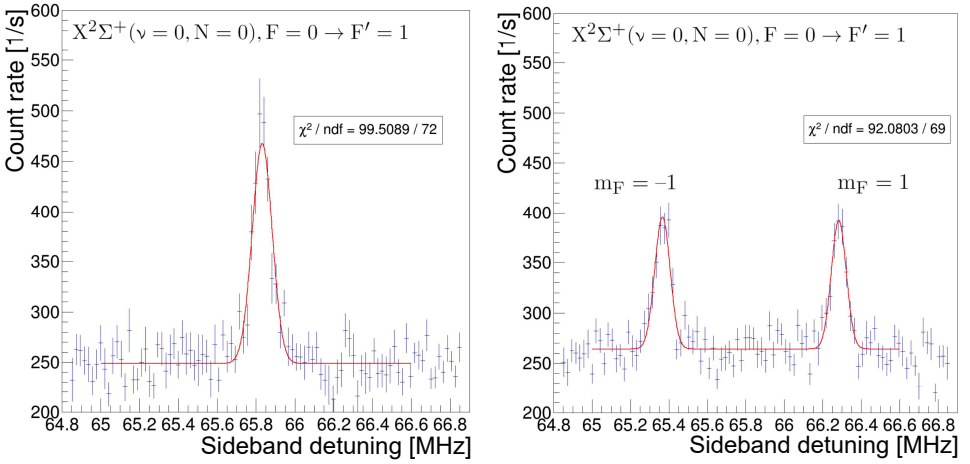

(a) $B_x = -7.4$ μT,$B_y = 0$ μT,$B_z = -0.6$ μT (b) $B_x = -4.2$ μT,$B_y = 27.6$ μT,$B_z = -5.4$ μT

Figure 5.2: Spectrum of the two-photon transition using a CW laser perpendicular to the molecular beam direction as shown in Figure 5.1. The population in the $X^2\Sigma^+(v = 0, N = 0, +, F = 1)$ ground state is probed via an excited state. The count rates recorded are plotted versus the AOM frequency (sideband detuning) which is the frequency difference between the two laser beams that drive the two-photon transition via a virtual excited state. In (a), no magnetic field is applied in the $\hat{y}$ direction. In (b) a magnetic field has been applied such that the Zeeman splitting equals around 1 MHz. The population is no longer degenerate so the amplitudes of the peaks are smaller than in (a). The measured magnetic field values are given in the subcaptions and have no calibration applied. In this case the electric field plates were set to 0 V/cm. The data points are fitted with a Gaussian (red line). The reduced χ^2 value of the fitted line is given on the figure. These were some of the first two-photon resonances observed for BaF, and these are the original figures found in Rozeboom's master's thesis [96].

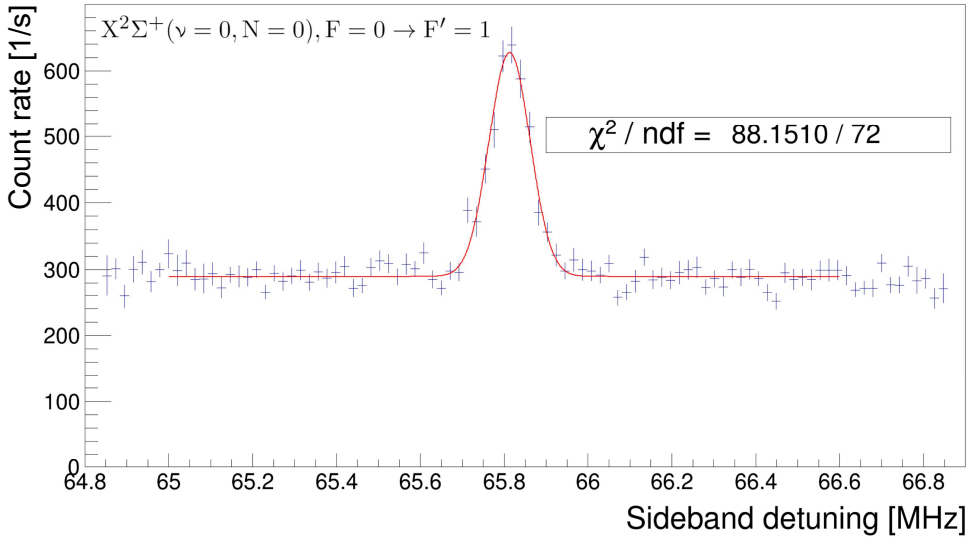

Figure 5.3: Measured magnetic fields: $B_x = 12$ μT,$B_y = -1.4$ μT,$B_z = -10.8$ μT (no calibration applied). Spectrum of the two-photon transition using a CW laser perpendicular to the molecular beam direction as shown in Figure 5.1. The population in the $X^2\Sigma^+(v = 0, N = 0, +, F = 1)$ ground state is probed via an excited state. The count rates recorded are plotted versus the AOM frequency which is the frequency difference between the two laser beams that create the two-photon transition via a virtual excited state. A magnetic field has been applied in the $\hat{x}$ direction, and no Zeeman splitting of the $m_F = \pm 1$ levels is observed. In this case the electric field was set to be 0 V/cm. The data points are fitted with a Gaussian line shape (red line). The reduced χ^2 value of the fitted line is given on the figure. These were some of the first two-photon resonances observed for BaF, and this is the original figure found in Rozeboom's master's thesis [96].

5.1.2 Combination of magnetic field directions

The hyperfine magnetic sublevel $m_F = 0$ is degenerate with the $m_F = \pm 1$ sublevels in zero fields. The latter are the sublevels used in the superposition in the eEDM experiment. However, without a magnetic field in the $\hat{x}$-direction, $m_F = 0$ is not included in the superposition of the m_F levels during the coherent optical state transfer from $F = 0$ to $F = 1$. This is the case that is required for the NL-eEDM experiment. The orientation of the electric field, magnetic field, the $\vec{k}$ and polarisation of the laser light are all crucial for the experiment and are also described in OBE calculations.

In Figure 5.4, the magnetic field in the $\hat{y}$-direction is high enough that the Zeeman effect has split the $m_F = \pm 1$ sublevels by approximately 1 MHz in both (a) and (b). When the magnetic field is only applied in the $\hat{y}$-direction as in Figure 5.4(a), population is only observed in the $m_F = \pm 1$ magnetic sublevels. This means that these are the only two m_F levels included in the superposition as required for the NL-eEDM experiment.

If a magnetic field is applied in both the $\hat{y}$ and $\hat{x}$-directions, as in Figure 5.4(b), three peaks are observed. In the middle of the two $m_F = \pm 1$ magnetic sublevels, the $m_F = 0$ magnetic sublevel is observed. The existence of population in $m_F = 0$ shows that the magnetic sublevel is included in the superposition between the $F = 1, m_F$ states within the coherent state transfer from $F = 0$ level. In order to suppress this, the magnitude, direction, and homogeneity of the magnetic fields must be well controlled inside the interaction zone. This is discussed in great detail in [18].

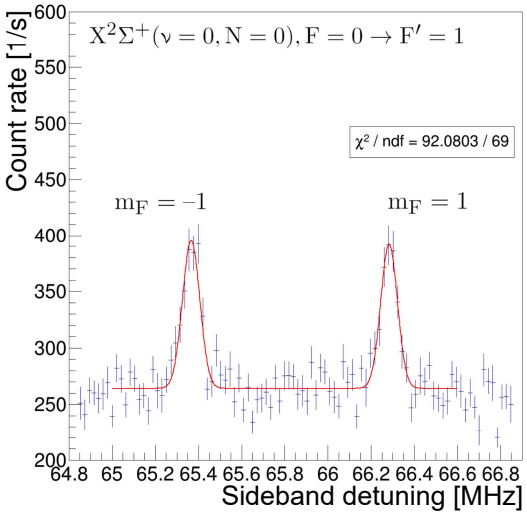

(a) $B_x = -4.2\ \mu$T,$B_y = 27.6\ \mu$T,$B_z = -5.5\ \mu$T

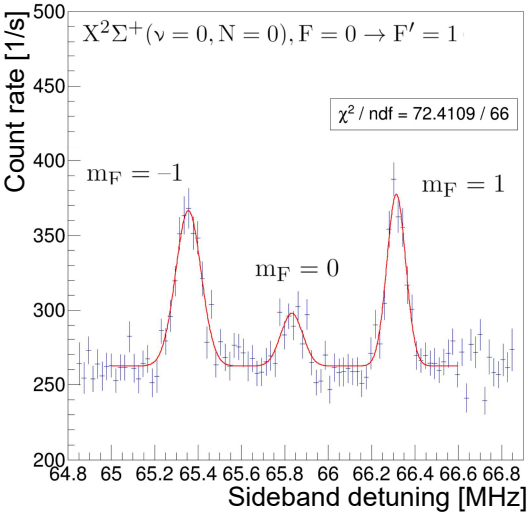

(b) $B_x = 15.2\ \mu$T,$B_y = 26.0\ \mu$T,$B_z = -6.6\ \mu$T

Figure 5.4: Spectrum of the two-photon transition using a CW laser perpendicular to the molecular beam direction as shown in Figure 5.1. The population in the $X^2\Sigma^+(v = 0,\ N = 0, +, F = 1)$ ground state is probed via an excited state. The counts are plotted versus the AOM frequency (sideband detuning) which is the frequency difference between the two laser beams that drive the two-photon transition (via a virtual excited state). The measured applied magnetic fields are given in the sub-captions (no calibration has been applied to these values). In (a), a magnetic field is applied in the $\hat{y}$ direction but not the $\hat{x}$ direction. In (b) a magnetic field has been applied in both $\hat{x}$ and $\hat{y}$ such that an additional $m_F = 0$ peak is observed in the middle of the two peaks labelled $m_F = \pm 1$. In this case no electric field was applied. The data points have been fitted with a Gaussian line shape (red line). These are original figures taken from Rozeboom's master's thesis [96].

5.1.3 Light shift effects

In order to find a suitable detuning Δ for the experiment, the light shift has been experimentally characterised. By changing the frequency of the laser light used to create the coherent state transfer laser light pulses, their frequency difference could be kept the same while their overall frequencies could be changed. A titanium sapphire laser (Freq3) was used for these experiments and its frequency was stepped across hundreds of MHz below, through and then higher than the resonance frequency in order to characterise the full spectrum. For each frequency step the AOM was scanned across the hyperfine structure frequency in order to build a 2-dimensional histogram to map out the light shift (AC Stark shift) effects.

In Figure 5.5, the laser light frequency is plotted versus the frequency $\omega_{PS}/2\pi$, where the colour shows the number of photons counted per laser pulse. A projection of just the top or bottom regions of this plot ends up in a figure similar to Figure 5.2(a). There are frequency gaps between the steps of Freq3 used to build this histogram that cannot be seen due to the binning in most cases, except for the occasional empty bin which is shown as a white space.

The bright horizontal lines in the center of the vertical axis show the case where the light is on resonance and a single photon transition is undertaken which transfers population to the $F = 1$ ground level that is probed. When the transition instead empties the $F = 1$ level this is observed as a horizontal dark blue line in the data. In order to not have any direct single-photon transitions take place, Δ must be large as it decreases the probability of such a transition. As $|\Delta|$ decreases, the light shift increases and therefore we observe a curve that decreases the ω_{PS} required to observe the two-photon transition. The light shift is in the same direction from both sides of the transition.

The plot explains why a large detuning Δ is desirable for Freq3 in the eEDM experiment as it reduces both the AC Stark shift and the probability of a single-photon transition. The ideal case for the eEDM experiment is with minimised sensitivity to the detuning Δ, so we use a $\Delta = 1000$ MHz in the experiment so that the light shift and the likelihood of a single-photon transition taking place are both very small. In addition, at high Δ, the difference between the two applied laser frequencies from the ground state hyperfine structure components becomes comparatively reduced.

The magnetic field is small enough in Figure 5.5 that the two $m_F = \pm 1$ sublevels are overlapped so there is only one curved line on each side of the single-photon resonance horizontal lines. In Figure 5.6, a magnetic field has been applied in the $\hat{z}$ direction in order to split the $m_F = \pm 1$ hyperfine sublevels by around 1 MHz. They are shown as the two curved lines on each side of the resonance rather than just the one. The two lines correspond to the two peaks shown in Figure 5.2(b) and Figure 5.4(a). The rest of the structure of the plot is very similar.

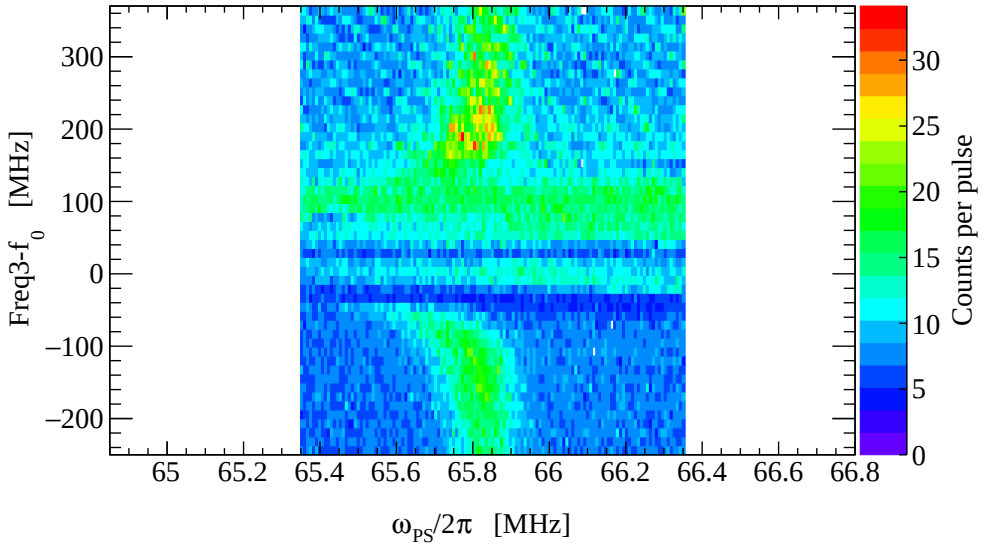

Figure 5.5: A map of the AC Stark shift is shown in a 2 dimensional histogram. The laser frequency Freq3 has been stepped below, through and then above the resonance frequency for the $X^2\Sigma(v = 0, N = 0) \rightarrow A^2\Pi_{1/2}(v = 0, J = 1/2)$ transition. For each frequency step of Freq3 the AOM frequency that defines the frequency difference between the two laser frequency components was scanned around the hyperfine structure as shown in Figure 5.3. The $F = 1$ sublevel of the ground state is probed via the $A^2\Pi_{3/2}(v = 0, J = 3/2)$ and the counts collected by the PMT at Region B of the experiment per molecular pulse are plotted as a rainbow colour scale. The laser light used for the two-photon transition is blocked from being collected by the PMT using an optical bandpass filter as described in Section 3.3.8. The magnetic field is such that the two $m_F = \pm 1$ components are overlapping in frequency. As Freq3 gets closer to the resonance, the AC Stark shift increases which is shown as a red-shifting curve. Close to the resonance in the center of the vertical axis one-photon transitions take place rather than two-photon transitions which means there is a direct transition via the real excited state. The horizontal lines in which there are very few counts shows where the $F = 1$ ground level has been depleted by the single photon transition. There are also bright horizontal lines which is where the population has been directly transferred from the originally populated $F = 0$ level into the $F = 1$ level. Data taken on the 27th of October. It has been plotted with the same axes as Figure 5.6 and therefore there is white space where there is no data. The data at the top of the plot has a larger background level than below which may be due to a change of power in Freq3.

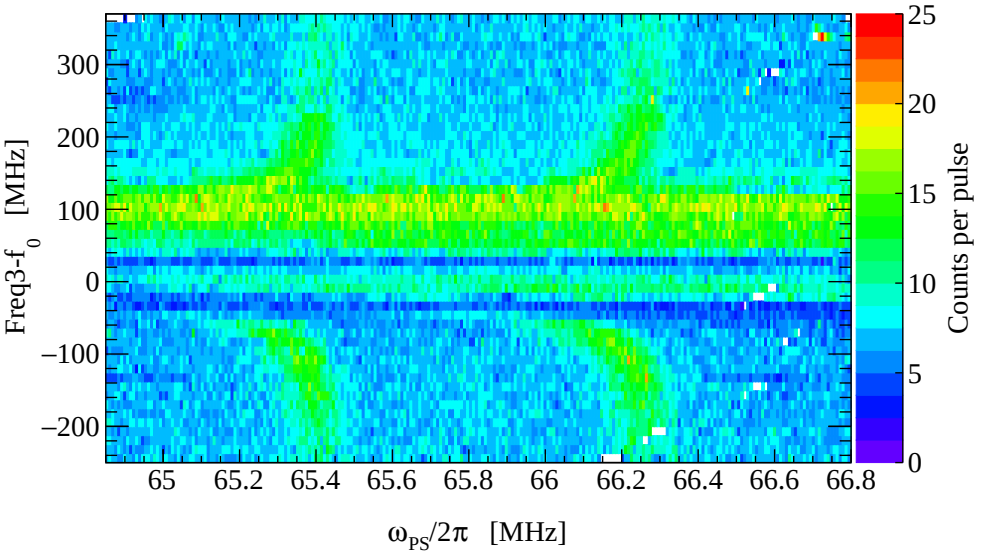

Figure 5.6: 2 dimensional histogram showing where the laser frequency Freq3 has been stepped below, through and then above the resonance frequency for the $X^2\Sigma(v = 0, N = 0) \rightarrow A^2\Pi_{1/2}(v = 0, J = 1/2)$ transition. For each frequency step of Freq3 the AOM frequency that defines the frequency difference between the two laser frequency components was scanned as shown previously in Figure 5.4(a). The $F = 1$ sublevel of the ground state is probed via the $A^2\Pi_{3/2}(v = 0, J = 3/2)$ and the counts collected by the PMT at Region B of the experiment per molecular pulse are plotted as a rainbow colour scale. The laser light used for the two-photon transition is blocked from being collected by the PMT using an optical bandpass filter as described in Section 3.4.1. The magnetic $m_F = \pm 1$ sublevels are split by about 850 kHz which corresponds to a magnetic field of around 30 μT in the $\hat{y}$ direction. As Freq3 gets closer to the resonance, the AC Stark shift shifts both m_F components which is shown as a red-shifting curve. Close to the resonance in the center of the vertical axis one-photon transitions take place rather than two-photon transitions which means there is a direct transition via the real excited state. The horizontal lines which have very few counts show where the $F = 1$ ground level has been depleted by the single photon transition. There are also bright horizontal lines which is where the population has been directly transferred from the originally populated $F = 0$ level into the $F = 1$ level. Data taken 19th October 2020.

5.2 Longer coherence times using the interaction zone

The use of the interaction zone, discussed in great detail in [18] and briefly summarised in Section 2.3, allows longer interaction times to be used for the coherent state transfer pulses while remaining in a homogeneous field region.

In this section, the experiments performed using the interaction zone are described, with the use of a controlled E- and B-field region and longer coherence times t and precession period T. The optical setup described in Section 3.4.5 provides complete customisation of the number of pulses and their timings. Both single and double laser light pulses are used for different parameter measurements. To quantify the results of these experiments, we use a model function that we fit numerically and define variables for direct comparison with the OBE calculations. Parameters such as the pulse timings, intensities, and electric fields are varied and the changes in the spin precession spectrum are quantified.

5.2.1 Model function used for numerical fitting

In Section 2.3.5, a quantum description of the population of the states was defined using the optical Bloch equations. To fit the data we use a three state approximation for an analytical description of the interference pattern. The three states are the $|1,\pm1\rangle$, $|0,0\rangle$ sublevels. The $|1,0\rangle$ sublevel is far detuned in the applied electric field due to the tensor Stark shift and therefore it is excluded. Even with no electric field applied, the magnetic field orientation means that the contribution of the $|1,0\rangle$ level in the superposition is strongly suppressed as shown in Section 5.1.2.

Following the argumentation in [98], an analytical description of the interference lineshape is used for numerical fits. The description gives the population in a particular F hyperfine state of $N = 0$ and depends on many parameters. In the description in [98], T is defined as the free evolution period between the two pulses, and τ_1 and τ_2 are the lengths of time that for which the two RF pulses are applied. In contrast, in our description, T is the time from the beginning of the first pulse to the beginning of the second pulse, and t is the time length of both pulses. We define a single detuning δ and a single Rabi frequency Ω_{PS} for both pulses.

The signal defined as the probability of finding a molecule in the state $F = 0$ is an interference of two amplitudes

$$P_{F=0} = |A + B|^2, \tag{5.1}$$

where the probability of finding a molecule in the other hyperfine sublevel $P_{F=1}$ is

$$P_{F=1} = 1 - |A + B|^2, \tag{5.2}$$

with definitions as given in Section 3.5 of [45] by

$$A = -\frac{{\Omega_{PS}}^2}{{\Omega_{PS}}^2 + \delta^2} \cos\left(\frac{\tilde{\phi}}{2}\right) \sin^2\left(\frac{t\sqrt{\Omega_{PS}^2 + \delta^2}}{2}\right) e^{-i(\delta_{\text{free}}(T-t)+\Phi)}, \tag{5.3}$$

and

$$B = e^{-i\delta t}\left(\cos\left(\frac{t\sqrt{\Omega_{PS}^2+\delta^2}}{2}\right) + i\frac{\delta}{\sqrt{\Omega_{PS}^2+\delta^2}}\sin\left(\frac{t\sqrt{\Omega_{PS}^2+\delta^2}}{2}\right)\right)^2. \tag{5.4}$$

The times T and t are the phase evolution period and the Raman pulse length, and Φ is an additional phase applied in between the pulses. δ_{free} is the detuning during the free evolution time. δ_{free} can vary due to a change of shifts due to experiment's parameters such as magnetic and electric fields. $\tilde{\phi} = 2(\mu B + D^{\not{P},\not{T}}E)(T-t)/\hbar$ is the phase accumulated in the $|1,\pm1\rangle$ states.

In order to fit the analytical expression numerically, the interferometry signal is expressed as the probability

$$P_{F=1} = S_R + S_I + S_C, \tag{5.5}$$

where

$$S_C = \left({c_1}^2 + \frac{\delta^2}{{W_1}^2}{s_1}^2\right)\left({c_2}^2 + \frac{\delta^2}{{W_2}^2}{s_2}^2\right), \tag{5.6}$$

and

$$S_I = \left(\frac{(\Omega_{PS}+\varepsilon)(\Omega_{PS}-\varepsilon)}{W_1W_2}s_1s_2cos(\phi)\right)^2 \approx \left(\frac{\Omega_{PS}^2}{W_1W_2}s_1s_2cos(\phi)\right)^2 \tag{5.7}$$

and using the same $(\Omega_{PS}+\varepsilon)(\Omega_{PS}-\varepsilon) = \Omega_{PS}^2$ approximation,

$$S_R = 2\frac{\Omega_{PS}^2}{W_1W_2}s_1s_2cos(\phi)\left[\left(\frac{\delta}{W_1}s_1c_2 + \frac{\delta}{W_2}s_2c_1\right)\sin(\vartheta) + \left(\frac{\delta^2}{W_1W_2}s_1s_2 - c_1c_2\right)\cos\vartheta\right], \tag{5.8}$$

using

$$W_i = \sqrt{\delta^2 + (\Omega_{PS}\pm\varepsilon)^2}, \tag{5.9}$$

where for one pulse the sign in the second term is positive and for the other it is negative. The previous equations also use

$$c_i = \cos\left(\frac{1}{2}tW_i\right), s_i = \sin\left(\frac{1}{2}tW_i\right), \tag{5.10}$$

and

$$\vartheta = \delta_{\text{free}}(T-t) + \Phi, \tag{5.11}$$

where δ_{free} is the average RF detuning during the free evolution period, 2ε is the difference in Rabi frequency between the first and second pulse. ϑ is a combination

of the detuning imbalances between pulses and detuning shifts during the free time evolution. In addition, the fit assumes an EDM that is too small to be observed a single fit so we define $\phi = \mu_B B(T+t)/\hbar$. Laser polarisation is assumed to be perfect and the efficiency of the optical pumping is included as the Offset in C. The light shift is ignored by the analytical description. At $\phi = \pi$, S_I and $S_R = 0$.

These equations are solved numerically using the fit function in Cern's ROOT package [66]. The fit parameters are:

- The offset from the initial conditions set by the state preparation (Offset).
- The maximum possible contrast as defined by $2 \times \text{Offset} + C_{\max} = 1$.
- T - the time between the start of the first pulse and the start of the second.
- t - the length of the pulses.
- δ the detuning that includes the hyperfine structure which depends on the electric field via the tensor Stark shift.
- Ω_{PS} - the average Rabi rotation frequency of the two pulses.
- ε - the difference from the average Rabi frequency for each pulse.
- ϑ - a combination of the detuning change between the pulses and from each pulse.
- B - the magnetic field.

The time T is fitted in wider scans but is a fixed parameter in the narrower scans that are ideal for the eEDM experiment measurements where the set point because the timings are very precisely realised in the experiment as discussed in Section 3.4.5.

5.2.2 Definition of the contrast axis of the spin precession spectra

When we make calculations using the optical Bloch equations we use the probability to find molecules in either F=1 and F=0 as the observables $P_{i=0,1}$ (see for example, Figure 5.15 during the discussion of the OBE calculations). In the experiment we measure the rate of photon fluorescence using transitions from these ground state levels. This is proportional to the probability to find a molecule in that level, but is not directly comparable without normalisation and rescaling. Under this process we aquire a variable called the Contrast (C) which is directly comparable to the probability of being in either the $F = 0, 1$ sublevels.

The photon counting rate for the signal at D has been converted into a background reduced and molecule number normalised signal called Sig(t), defined in Equation 3.7 (see Sections 3.4.1 and 3.4.2). The complex interference pattern relies on various experiment's parameters. We convert Sig(t) into C. When C is 1, the probability of finding a molecule in $F = 1$ is 100%, and when it is 0, the probability is 0%. The fringe amplitude is reduced from the full range by the initial condition of the states after state preparation by hyperfine optical pumping as discussed in Section 3.4.3.

This depends on the experimental conditions of the experiment, and needs to be extracted from the data. A finite hyperfine pumping efficiency results in a fraction ϵ_{hfp} to remain in the $F = 1$ sublevel. The consequence of this is that the maximum fringe value will be $1 - \epsilon_{\mathrm{hfp}}$ and the minimum fringe value will be $0 + \epsilon_{\mathrm{hfp}}$. The sensitivity of the experiment depends on the contrast that is experimentally obtained so we aim to have maximised hyperfine pumping (see Section 3.4.3). The value ϵ_{hfp} is extracted from the numerical fit as the offset from 0 for $\mathrm{Sig}(t)$, which we here call simply Offset.

In addition to the efficiency of the hyperfine pumping, conversion from $\mathrm{Sig}(t)$ to a fringe contrast also requires the numerical fit to calculate what the maximum fringe amplitude (Amp) is. This value is calculated in the fitting procedure which takes into account all the required variables such as magnetic field, electric field, laser light intensity, light shifts, polarisation and number of molecules. The conversion is then implemented by

$$\mathrm{C} = \mathrm{Sig}(t) \div \left(\frac{\mathrm{Amp}}{2 \times \mathrm{Offset} + \mathrm{Amp}} \right), \tag{5.12}$$

where C is directly comparable to the calculation of P_i by the optical Bloch equations. In the upcoming interference spectra in this chapter the $\mathrm{Sig}(t)$ have been converted to C. The uncertainty in the contrast comes from the original PMT counts at Regions B and D for the background removal and normalisation processes as described in Sections 3.4.1 and 3.4.2. The value of the uncertainties are propagated in the same way as the values as described in this section.

5.2.3 Definition of the frequency axis of the spin precession spectra

The horizontal axis of the spin precession spectra (see Figures 5.8 and 5.10) is derived from the set points of stepped frequencies created by the frequency generators as described in Section 3.4.5. The set points of the generated RF signals sent to the AOMs for each shot are measured and the difference is plotted as the horizontal axis. The set point frequencies are plotted rather than the measured frequencies due to the discretisation error in the counting measurement method, which limits the frequency measurement to about 10^{-6} (100 Hz from 66 MHz). Integrating ten readouts of the measured frequency gives a precision of only 10 Hz precision in one second of data acquisition at an ablation pulse rate of 10 Hz.

The plotted variable is defined as $\omega_{PS}/2\pi$, which is the difference between the P and S laser frequencies converted from radians. Different spin precession spectra in this work were taken in various E-fields so the centre point of these plots are shifted with respect to each other. This is discussed further in Section 5.4.3 and quantified in Figure 5.14.

The uncertainty of the frequency arises from phase noise of the two coherent state transfer laser light pulses, with timings set by frequency synthesisers (as described in Section 3.4.5) which are synchronised in both frequency and phase. The phase noise between the two frequency synthesisers is measured using a Minicircuits ZRPD-

1 Phase detector to be $<< 1°$. The uncertainty gained in $T = 1$ ms is estimated to be 30 mrad and amounts to 10 Hz.

5.3 Single pulse experiments

The experiment, optical Bloch equations and numerical fitting of the model function are all set up that full flexibility of the parameters of the pulses can be utilised. We therefore use the same calculation and experimental methods to take measurements with a single pulse as with two pulses. In the model function, setting either the intensity of the second pulse to 0 or setting the value of T to be 0 allows a single pulse to be calculated.

Using a single pulse means that the interaction zone can be probed and its dimensions mapped by varying its intensity and timing parameters.

5.3.1 Effective Rabi Frequency

The Rabi frequencies Ω_P, Ω_S depend on the amplitude of the electric field strength of the laser light and the matrix elements of the dipole operator. The electric field strength of the laser light is related to its intensity via

$$I_{i,\mathrm{sat}} = \frac{\pi hc}{3\lambda_i^3}\Gamma_i, \tag{5.13}$$

which using $\Gamma = 1/\tau \approx 1/57$ ns^{-1} [42] and $\lambda = 860$ nm gives $I_{\mathrm{sat}} \approx 0.6$ mW/cm^2. The intensity is related to the Rabi frequency via

$$\frac{I_i}{I_{i,\mathrm{sat}}} = \frac{2\Omega_i^2}{\Gamma_i^2}. \tag{5.14}$$

The two-photon Rabi frequency is $\Omega_{PS} = \frac{\Omega_P \Omega_S}{2\Delta}$ where Δ is the detuning from the excited state. A full derivation is given in Section 4.3.2 of [45]. Ω_{PS} is well-defined for a two level system with $\delta = 0$. When the laser light frequencies are not on resonance the effective Rabi frequency is used which is defined as

$$\Omega_{\mathrm{eff}} = \sqrt{\Omega_{PS}^2 + \delta^2}. \tag{5.15}$$

By multiplying this value by the pulse length t and dividing by π we define the Rabi oscillation rotation that for a π-pulse and a full population transfer, $\Omega_{\mathrm{eff}} t/\pi = 1$. This effective Rabi frequency is what is measured in the experiment. Changes in the laser pulse intensity, electric and magnetic fields (via shifts that change the detunings) and pulse length δ all are extracted by measuring the rotation of the Rabi oscillation.

5.3.2 Rabi oscillation

Two cases are shown for a single pulse experiment in Figure 5.7. Two Rabi oscillation rotations have been measured using the fitting procedure discussed in Section 5.2.1, and as discussed in Section 4.4 of [46], this is in excellent agreement with the calculations using the OBE. The fitting procedure is the same as that for two pulses, but

defined as the second pulse having zero intensity. The rotation of the Rabi oscillation is extracted by comparing the amplitude of the side peaks with the central peak. The side peaks are due to the shape of the laser pulses and the widths of the peaks are due to the length of the laser pulse t, which was kept the same between the two cases. A change in effective Rabi frequency Ω_{eff} is therefore measured.

These plots were created by changing the delay of the pulse arrival from 3.2 ms to 4.2 ms such that the intensity changed between the two cases. This technique is used in [18] to map out the field homogeneity of the interaction zone by using a single short pulse and changing the delay such that the laser light pulse interacts with the molecular pulse at different positions of the interaction zone.

The intensity of the laser pulses changes as the light has a divergence as it travels through the experiment, such that the intensity of the first laser light pulse is always less than that of the second pulse. In this case, the delay change means changing the position that the molecules are in within the interaction zone when probed by the pulse. The Rabi frequency experienced by the particular molecular pulse is compared to that measured at other regions. In addition, if the laser beam is not completely overlapped with the direction of the molecular beam, this will be observed in the data.

In addition, changing the delay allows the characterisation of the interaction zone. By applying a short t laser light pulse in different regions of the interaction zone with varying delay, the electric and magnetic field are extracted from the fit for each timing step and a map of the fields is created. The magnetic field increases before and after the interaction zone region and the electric field decreases. These cause shifts via a chance in Zeeman and tensor Stark shifts which result in a detuning change, which changes the Rabi frequency. These field changes are measured by the fitting procedure Section 5.2.1. This is discussed in detail in Section 5.3 of [18]. Using this technique the beginning and end of the homogeneous regions of the interaction zone are defined and therefore the ideal delay settings for maximising the time T for the time from the beginning of the first to the beginning of the second pulse. By maximising T, a higher statistical precision is achieved.

By manually changing the delay that is applied to the laser pulses that create and readout the superposition, the effect is characterised and compared to the OBE. In this way, subsequent possible systematic effects from a change of the delay in the experiment are characterised and identified. We can use this characterisation to define how well that the delay must be known in order to acquire a certain eEDM limit.

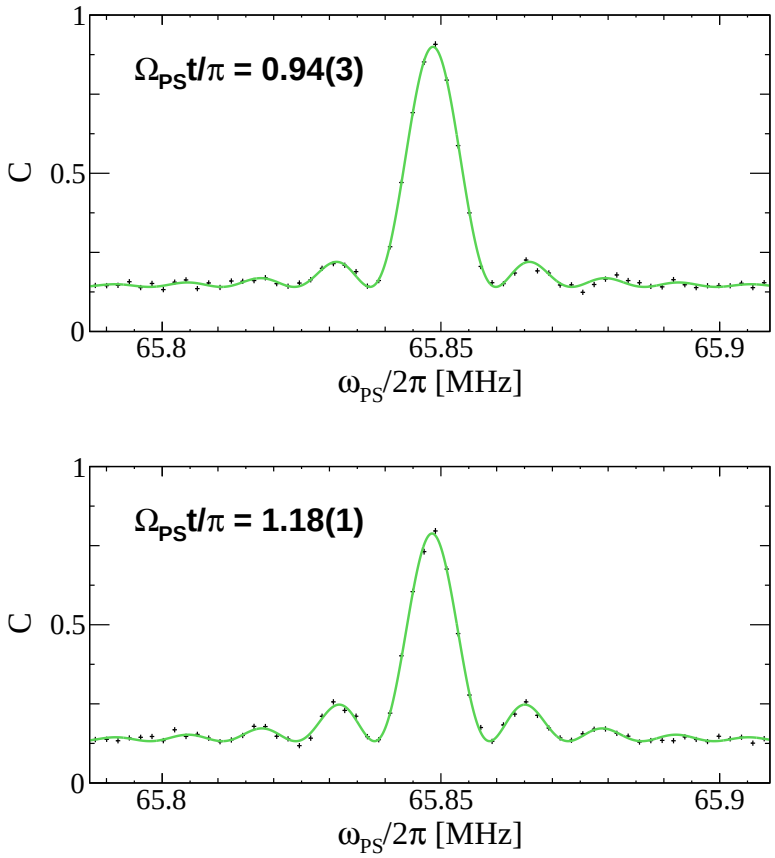

Figure 5.7: Two-photon spectrum in the case of a single laser pulse for coherent state transfer. The pulse length t is 80 µs and the Rabi phases $\Omega_{PS}t/\pi = 0.94(3)$ (top) and $\Omega_{PS}t/\pi = 1.18(1)$. The frequency of the difference between the two laser frequencies used for the coherent state transfer ($\omega_{PS}/2\pi$, see Section 5.2.3) is stepped from 65.786 MHz to 65.910 MHz and is plotted against the contrast C (see Section 5.2.2). The same numerical fit function is used as for the double pulse measurements as double pulse but set to have only one pulse. The delay was changed from 3.2 to 4.2 ms from the start of the laser ablation and the intensity was not changed. The timings were manually changed to show the capabilities of the method. Such changes are detectable and therefore quantifiable by the fit. Plots also shown in [45]. Data taken 25th November 2022.

5.3.3 Pulse length t change

In Figure 5.8 a single pulse has been applied at a delay of 3.2 ms with different pulse length times t. A spectrum showing the resulting population distribution across the $N = 0, F = 0, 1$ states has been plotted for each one. In the top left case, no pulse has been applied and the population is almost entirely in the $F = 0$ state. As the pulse gets longer, the population distribution changes from the top right where the peaks are similar in amplitude to the bottom left where the two $F = 1$ peaks are higher in amplitude than the one $F = 0$ peak. Finally a pulse length is used in the bottom left example that achieves close to a perfect π-pulse, where the population is coherently transferred entirely into the $F = 1$ hyperfine level and the $F = 0$ is similar in magnitude to the background noise. By probing both the $F = 0$ and $F = 1$ populations, the population transfer is monitored and therefore the ϕ is extracted without the requirements of normalisation as discussed in Section 3.4.2. This simultaneous monitoring of the populations is not yet implemented in the experiment. In the plots shown in Figure 5.8, the data has been taken and processed in the same way as described in Chapter 4.

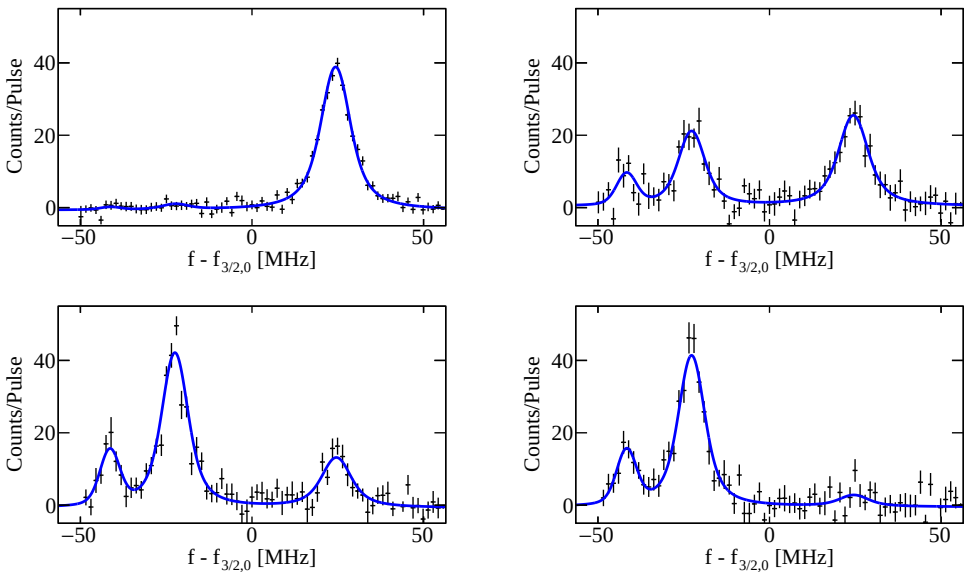

Figure 5.8: Spectroscopy of the $X^2\Sigma^+(N = 0) \rightarrow A^2\Pi_{3/2}(J = 3/2)$ transition versus measured intensity multiplied by the period of the single pulse. The population in the ground $F = 0, 1$ states varies with the phase of the Rabi Oscillation. The times are starting from the top left and continuing in a clockwise direction: $t = 0, 40, 60, 80$ μs. Data taken 29th March 2023.

As the pulse length changes, the population that is coherently transferred to end up in either the $F = 0$ or $F = 1$ level in $F = 0$ after the spin precession changes. Defining 100% population in $F = 0$ as C = 1, and 100% in $F = 1$ as C = −1, a variable named Asymmetry is defined. This definition is equal to $-((2 \times C) - 1)$, where the definition of C is found in Section 5.2.2. The asymmetry also depends on the initial conditions of the state preparation, and if the optical pumping out of the $F = 1$ hyperfine state does not have 100% efficiency then total asymmetry= 1 cannot be reached.

The calculated asymmetry for various pulse lengths is shown in Figure 5.9(a). The first four data points are calculated from the spectra shown in Figure 5.8. The data points are calculated as

$$\text{Asymmetry} = \frac{\text{Amp}_{0-1} - \text{Amp}_{1-2}}{\text{Amp}_{0-1} + \text{Amp}_{1-2}}, \tag{5.16}$$

where Amp_{0-1} is the fitted area under the $X^2\Sigma^+(N = 0, F = 0) \rightarrow A^2\Pi_{3/2}(J' = 3/2, F' = 1)$ resonance and Amp_{1-2} is the fitted area under the $X^2\Sigma^+(N = 0, F = 1) \rightarrow A^2\Pi_{3/2}(J' = 3/2, F' = 2)$ resonance as described in Section 4.3.3. The asymmetry reduces as the pulse length increases. Two data points were taken for the same pulse length which are shown at with slightly different values due to a change of intensity which is measured in the experiment.

The loss in contrast of the asymmetry is due to the range of Rabi frequencies for the molecules in the pulse, which comes from the Gaussian distribution of the laser pulses used for the coherent state transfer as described in Section 3.4.5. The Rabi frequency depends on the intensity of the light which depends on the position of the molecule within the light used for the coherent state transfer. The FWHM of the light distribution is 2 cm and the central 5 mm diameter contribute to the signal.

The fitted asymmetry line shown in Figure 5.9(a) is an integral over the probability distribution of the Rabi frequency a distance r from the centre of the distribution. The Rabi frequency at distance r is given as

$$\Omega_{\text{PS}}(r) = \Omega_0 \cdot \exp\left(\frac{-r^2}{2\sigma^2}\right), \tag{5.17}$$

where Ω_0 is the Rabi frequency at the centre of the distribution and σ is the standard deviation of the distribution. The maximum possible position r_{max} is the furthest distance from the centre that the molecule's in the beam can interact with the laser light. The asymmetry is given by

$$\text{Asymmetry}(t) = -\frac{2}{r_{\text{max}}^2} \int_0^{r_{\text{max}}} \cos\left(t \cdot \Omega_0 \cdot \exp\left(\frac{-r^2}{2\sigma^2}\right)\right) \cdot r \; dr, \tag{5.18}$$

where the number of molecules that observe this Rabi frequency is $2\pi r$ and the asymmetry has been normalised to be between −1 and +1. As the molecules interact with the laser pulse for longer pulse times t, the molecules interact with different intensities of the light as the width changes more, and therefore the range of Rabi frequencies experienced by the molecules increases. When integrated across the width of the distribution, this creates a drop in the absolute value of the asymmetry.

The asymmetry value does not depend on the number of molecules if both $F = 1$ and $F = 0$ are measured simultaneously, which they are not in this case. Figure 5.9(b) shows the area under the fitted curve as a function of the Rabi frequency multiplied by the pulse time. The data has not been normalised so there are fluctuations in the value which are due to the change in the number of molecules as discussed in Section 3.4.2. Normalisation of the data before fitting would also overcome the molecular fluctuations, except for the size of the uncertainty due to the amount of statistics collected. Although there are molecular fluctuations, there is not a large enough drop in molecule number to account for the loss of asymmetry as observed in Figure 5.9(a), so it is due mainly to the Gaussian distribution in the $x - y$ plane of the laser light pulse.

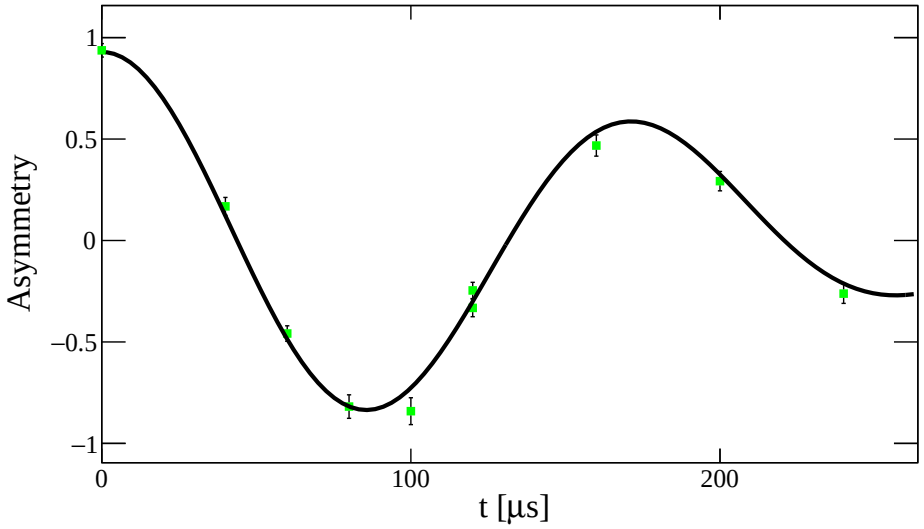

(a) The asymmetry (where 1 is 100% of the molecules in $F = 0$ and -1 is 100% in $F = 1$) is plotted (green data points) versus the pulse lengths applied. There are two data points with a pulse length of 120 μs, which have different asymmetries due to slightly different laser intensities. The initial conditions are dependent on the efficiency of the hyperfine optical pumping in the state preparation stage. A π-pulse is defined as the phase at which the coherent state population transfer to F=1 which is defined as an asymmetry of -1. The Rabi frequency is calculation from a measurement of the sum digitised photodiode of the integrated power of the two polarisation components of the laser pulse (see Section 3.4.5). A curve defined as Equation 5.18 has been numerically fitted to the data points with a $\chi^2_{\text{red}} = 1.5$. The contrast in the asymmetry reduces as the phase increases due to the truncated Gaussian intensity distribution. The horizontal error bars are too small to be seen and the vertical error bars are taken from the fit of each spectrum and is dominated by the statistical fluctuations. Data taken 29th March 2023.

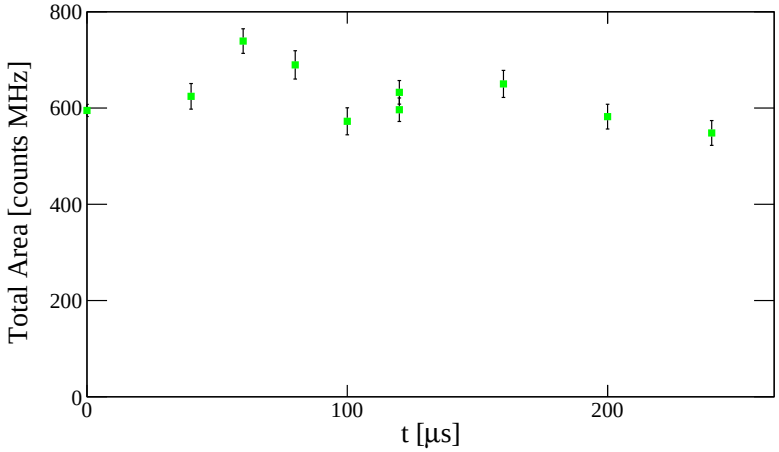

(b) The Rabi frequency multiplied with the pulse length is plotted against the total area under the curve of the fit applied given in counts (per molecular pulse) multiplied by the frequency in MHz, which is proportional to the number of molecules. The molecule number is shown to not decrease enough to explain the loss of asymmetry contrast observed in (a). The molecule number extracted from the fit.

Figure 5.9: The asymmetry between the populations in $F = 0$ and $F = 1$ for different pulse lengths and the total area under the curve for each spectrum. A selection of the spectra used to extract the asymmetries are shown in Figure 5.8.

5.4 Double pulse Experiments

By comparison of experimental results with calculations using the optical Bloch equations (OBE), the effect that systematic errors have on the measurement results is limited. Using this technique, the effect that specific parameters have on the results is described such that their signals are identified and disentangled from each other.

5.4.1 Spin Precession Spectrum

In Figure 5.10, a spectrum gained from varying the detuning applied for the spin precession process is shown. The contrast C (see Section 5.2.2) of the spectrum is plotted as a function of the frequency difference $\omega_{PS}/2\pi$ applied to the two AOMs (see Section 5.2.3). These spectra are the basis of our systematic effect characterisation and are obtained due to the excellent control we have on our all-optical spin precession creation parameters such as phase, frequency and timings. The applied laser field $\omega = \omega_S - \omega_P$ for the light pulses works as a reference oscillator in order to obtain a phase difference measurement. The two applied pulses are stable in their relevant phases in order for such an experiment to work. In addition, phase jumps are allowed in between these pulses as long as they are not sensitive in time. Obtaining a phase measurement gives much higher precision than a frequency spectrum as it takes all available relevant information coherently into account [45].

The shape of the spectrum depends on the experiment's parameters (see Section 5.2.1). For example, the sharpness of the peaks in the interference spectrum is defined by T and the size of the envelope function originates from t. The middle region is flat in the ideal case and the height of this region depends on the phase ϕ. The frequency that this flat region occurs at depends on the tensor Stark shift of the $m_F = \pm 1$ states via the electric field applied. The width of the flat section depends on the intensity of the laser light pulses.

Spectra such as the one shown in Figure 5.10 have a wider range of frequencies than is optimally required for an eEDM experiment with highest sensitivity. In a perfect π-pulse the central part is most sensitive to the eEDM by being in the middle of the contrast axis at $C = 0.5$. Calculations of spectra with perfect π-pulse conditions are shown in [45]. Other regions of the spectrum remain sensitive to the eEDM, and therefore a balance must be taken between the range of frequencies to create a spectrum that can be compared to the numerical fit and the OBE calculations to measure changes in the experiment, and maximising the sensitivity of the experiment. This is quantified with calculations as discussed in Section 5.4.3.1.

The range of frequencies that is experimentally useful to probe depends on the parameter that is being measured. The spectrum is most sensitive to the intensity of the laser light pulse intensities used for coherent state transfer in the wings, whereas for magnetic field the centre is the most sensitive.

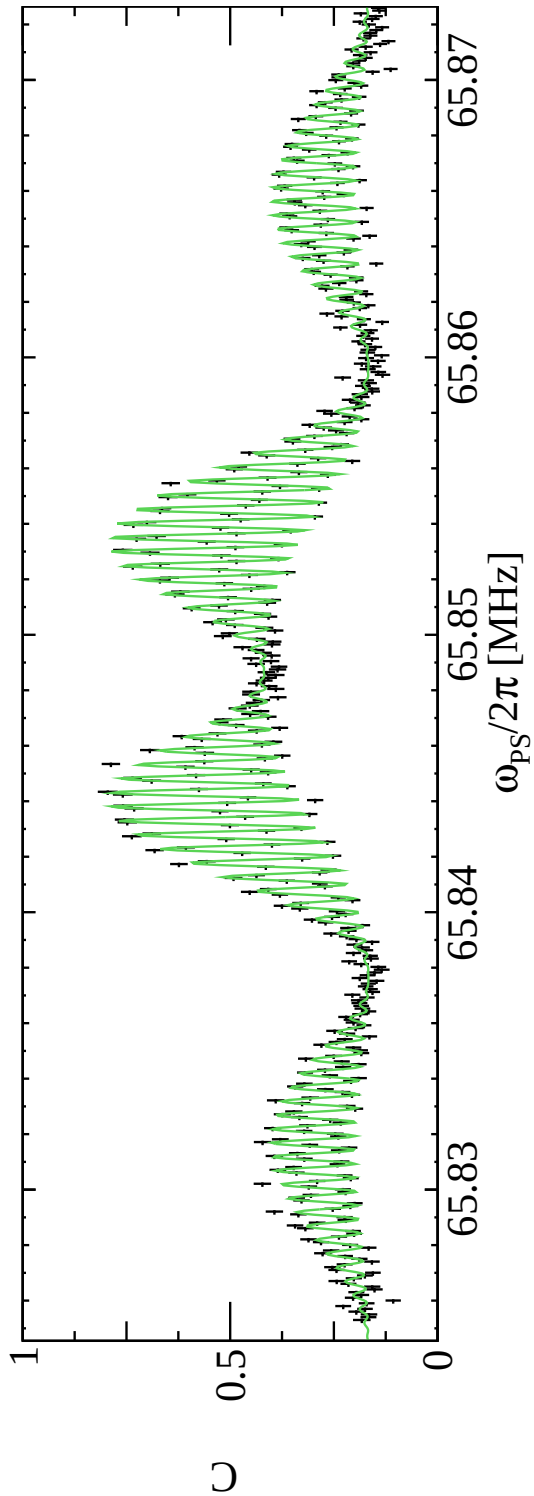

Figure 5.10: Black data points: the contrast of the spectrum is plotted against the frequency difference set by the two AOMs. The green line is an analytical equation fit numerically described in Section 5.2.1. The pulse timings were $T = 2$ ms, $t = 80$ μs and the electric field was set to 0 V/cm. The data was taken 8th of December 2022. The flat section in the middle of the plot is the most sensitive to the eEDM. There are 480 frequency points and the χ^2_{red} is 1.95.

5.4.2 Rabi frequency dependence on pulse intensity

In Section 5.3.3, the variation of the Rabi phase applied in a single pulse was shown by changing the pulse length. The Rabi phase $\Omega_{\mathrm{PS}}t$ is also dependent on the intensity of the overlapping laser beams that create the coherent transfer to transfer the molecules into and out of the superposition state. In Figure 5.11, the overlapped beam power measured by a photodiode as described in Section 3.4.5 is plotted against the calculated Rabi phase from each spectrum shown in Figure 5.12. The Rabi frequency becomes an observable using this method.

As the Rabi phase changes from a π-pulse, the flat section that is most sensitive to magnetic field changes and the EDM is not longer flat, with either increasing or decreasing laser light intensity. Figure 5.12 shows a wider range of frequencies than would be used in an EDM experiment to show the larger overall structure of the spin precession spectrum in different Rabi phases. As the intensities change more, the side band structure flattens with low intensity and increases with higher intensity, while the structure of the middle section (approximately 65.840 to 65.855 MHz for the top plot) becomes smaller. At Rabi phases like these that are far from a π-pulse, the smaller signals mean that the the associated χ^2_{red} values given in the caption become larger, and it is consequently harder to use these fits to extract quantitative parameters with which an EDM can be measured.

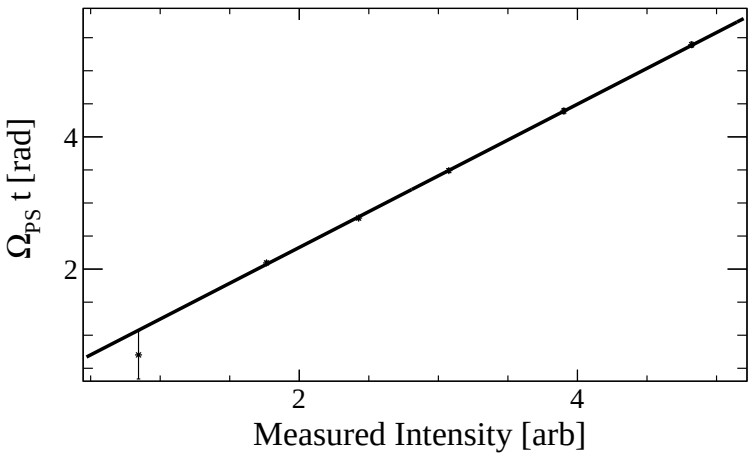

Figure 5.11: The calculated Rabi phase $\Omega_{\mathrm{PS}}t$ from each spectrum shown in Figure 5.12 is plotted against the integrated intensity of the coherent state transfer overlapped laser beams measured by a photodiode. The calculated Rabi phase is a calculated as a parameter of the numerical fitting function. The lowest intensity data point has a larger uncertainty as very few molecules are transferred into the superposition state so the statistics are smaller. The black line shows the fitted linear dependence. The data was taken on the 28th October 2022.

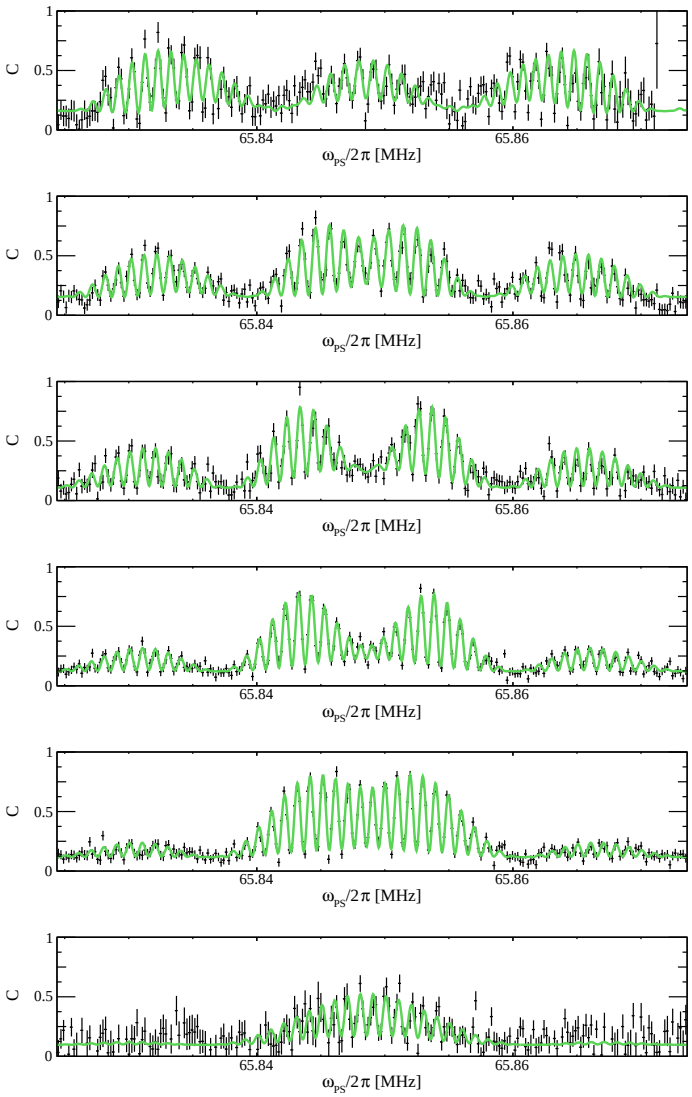

Figure 5.12: Interference spectrum showing how intensity changes the observed spectrum by changing the Rabi frequency where the top figure has the highest power, and the bottom figure has the lowest. The measured intensities for these are plotted against the calculated Rabi frequency multiplied by the pulse length in Figure 5.11. The B and E fields and timing parameters of the laser pulses were kept constant, and the intensity was varied by changing the power of the original laser from which the two overlapped laser beams are derived so both beam powers were changed by the same ratio. The χ^2_{red} values for the fitted lines green are (from top to bottom) 1.5, 1.2, 1.1, 1.0, 1.0, and 1.3. The ideal case is a π-pulse, for which the closest plot is the 3rd from the top. The uneven sides bands show evidence of inhomogeneity in the experiment. The electric field was set to 0 kV/cm in all cases. The line was made with five fitted parameters: contrast offset, contrast amplitude, Rabi frequency, centre frequency and the intensity ratio. The data was taken on the 28th October 2022.

The hyperfine splitting of the ground state (HFS) is extracted as one of the fitted parameters of the model function (see Section 4.3.3) which can be seen as the green line in the spin precession spectra. Extrapolating the HFS from the plots shown in Figure 5.12 to the case with zero intensity and therefore no light shift, gives HFS= 65.848714(40) MHz. The uncertainty is dominated by the light shifts as they are not included in the numerical fitting function and has a correction of $\mathcal{O}(130)$ Hz from Doppler shifts. This value is different from the literature value as discussed in Section 4.3.2.

At the top and bottom of Figure 5.13 (b), two histograms are plotted with results similar to Figure 5.12 but for a smaller frequency range, for a higher (top) and lower (bottom) laser light intensity case. In between these two figures is a three dimensional histogram with counts plotted as colours from dark blue (no counts) to bright yellow (high count rate), and the vertical axis the Rabi phase. This plot shows the change of the shape of the spin precession spectrum when the intensity of the overlapping coherent state transfer laser beams are changed. Comparing the top and bottom plots, it is observed that the number of peaks in the flatter section changes from three in the lower Rabi phase case to one in the higher Rabi phase case.

The results using calculations with OBE as described in Section 5.4.3.1 are shown in Figure 5.13 (a). The red box indicates the area of the plot that is displayed in the experiment data of (b). The number of central peaks also changes from three with the lower Rabi phase to one for higher Rabi phase. The overall change of shape of the spin precession spectrum is in agreement with the experimental results. A comparison of the two shows that there is an imbalance between the amplitudes of the peaks at lower frequency and higher frequency in the experimental data that is not seen in the calculations. This points to inhomogeneity in the experiment or imbalance in the individual laser light beams that overlap and create the coherent state transfer in the experiment. This measurement means that this is known about and that such systematic errors can be overcome.

For OBE calculations such as Figure 5.13(a) and Figure 5.15 and those given in [45], the horizontal axis is $\delta = \omega_{PS} - \omega_{\mathrm{HFS}}(E_0)$ such that the plot is centered around 0. For the experimental data plots, we can extract the tensor Stark shift ω_{HFS} using the fitting function so this is not subtracted.

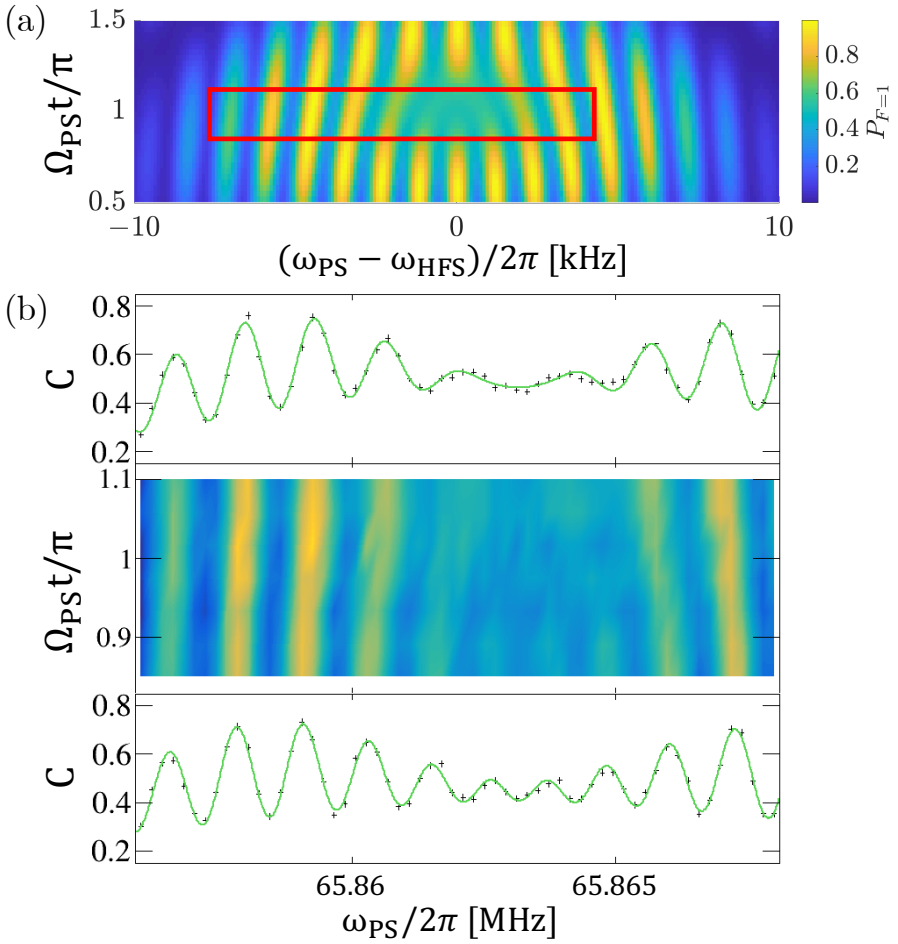

Figure 5.13: (a) Calculation of $P_{F=1}$ as function of $\delta = \omega_{PS} - \omega_{\mathrm{HFS}}(E_0)$ and state rotations of $\Omega_{PS}t$ ranging from $\pi/2$ to $3\pi/2$. The magnetic field B provides a phase $\phi = \pi/2$ (see Equation 2.5). Note, that the number of interference fringes is different by 2 for $\Omega_{PS}t/\pi$ larger, respectively smaller than 1. The red box indicates the region measured in (b). (b) Observed fringe pattern for different $\Omega_{PS}t$, at $\phi \approx \pi/2$. The spectra at the top and the bottom are at $\Omega_{PS}t/\pi = 1.092(6)$ and $\Omega_{PS}t/\pi = 0.853(6)$. The line through the data points is the result from OBE. The uncertainties on the data points result from photon counting statistics. Data taken 25th June 2022.

5.4.3 Effect of electric and magnetic fields on the spin-precession results

Figure 5.15(c) is experimentally verified in Figure 5.14(a). The applied electric field was changed and two of the spectra are plotted in the same figure in order to show the observed frequency shift. The horizontal axis is the RF difference between the AOMs as discussed in Section 3.4.5. The vertical are discussed in Sections 5.2.2 and 5.2.3 and the fits applied to the data points is discussed in Section 5.2.1. In Figure 5.14(b) the applied electric fields are plotted versus the extracted centre point of the fit which includes the tensor Stark shift. The vertical axis is given as $\omega_{\mathrm{HFS}}/2\pi$ as it is the calculated hyperfine structure frequency. The shift in frequency per electric field is defined as the slope of the tensor Stark shift at that electric field value $d\omega_{\mathrm{tensor}}/dE$. The slope is determined to be 14.99(7) Hz/(V/cm).

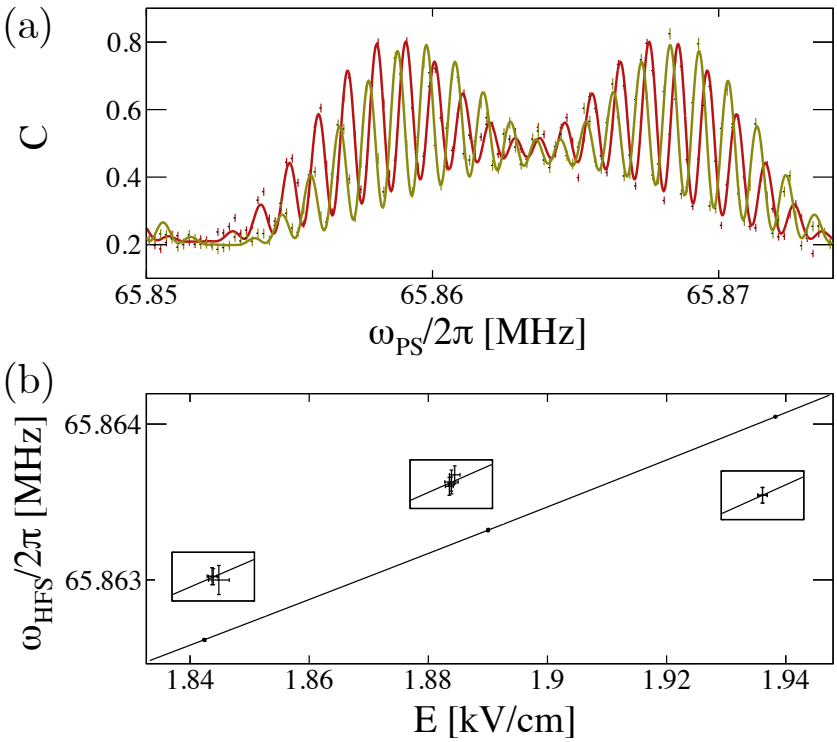

Figure 5.14: (a) Observed interference pattern for electric field $E = 1.8900(3)$ kV/cm (red) and $E = 1.9383(3)$ kV/cm (green). The electric-field-dependent hyperfine structure $\omega_{\mathrm{HFS}}(E)$ is determined by the center frequency of the interference pattern. The magnetic field is $B = 4.04(7)$ nT and the timings are $T = 1$ ms and $t = 80$ μs. The contrast C is the experimental realisation of $P_{F=1}$. The uncertainties of the data points are determined by the counting statistics of the fluorescence signal. (b) The hyperfine structure splitting $\omega_{\mathrm{HFS}}(E)$ changes with electric field by 14.99(7) Hz/(V/cm) at $E = 1.9$ kV/cm. The three insets are at 100 times enlarged scale to show the uncertainties (i.e. 1 V/cm, resp. 20 Hz). Figure and caption from [46].

5.4.3.1 OBE calculations of the magnetic and electric fields

The external electric fields and magnetic fields have identifiable and separate effects on the shape of the interference spectrum. In Figure 5.15, these two effects are shown and are observably different to each other. The optical Bloch equations have been used to calculate the populations P_i in different spin-precession conditions.

Two of the conditions that can change in the experiment and are essential to measure are the magnetic fields and the electric fields. The effect that these parameters have on P_i has been calculated in order to understand how to identify changes from particular parameter variations during the experiment. The phase ϕ is determined by the magnetic and electric field via the Zeeman effect and the EDM as described by Equation 2.5. In addition, the electric field affects the phase via the tensor Stark effect as $\theta = \delta \cdot T$ due to $\delta = \omega_{PS} - (\omega^0_{\mathrm{HFS}} - \omega_{\mathrm{tensor}}(E))$. The two phases ϕ and θ have distinguishable signatures in the interference signals which is shown in Figure 5.15. This means that changes in the experimental spin-precession spectrum signals are identified as being from either the eEDM, magnetic field or electric field changes.

As is observed in Figure 5.15a, an increase of ϕ leads to a population $P_{F=1}$ increase for all values of ω_{PS}. The difference between the two plotted conditions is shown in (b). In comparison, a change of electric field and therefore θ gives a frequency shift along the horizontal axis of (c). The difference between the two θ conditions is given in (d). The two effects are clearly quantifiable and distinguishable from each other. The dashed lines in (b) and (d) are the average of $\Delta P_{F=1}$ across the plotted 8 kHz frequency axis. With respect to the sensitivity at the most sensitive point ($\delta = 0$ kHz), the EDM reduces by only $\approx 10\%$, which is very small in comparison to the precision gained by the quantification of the possible systematic effects. This is why the use of such spectra gives a net gain in precision over only observing at the most precise point. In this way, the possible systematic effects are quantified simultaneously to the eEDM extraction experiment, rather than more supplementary experiments being required.

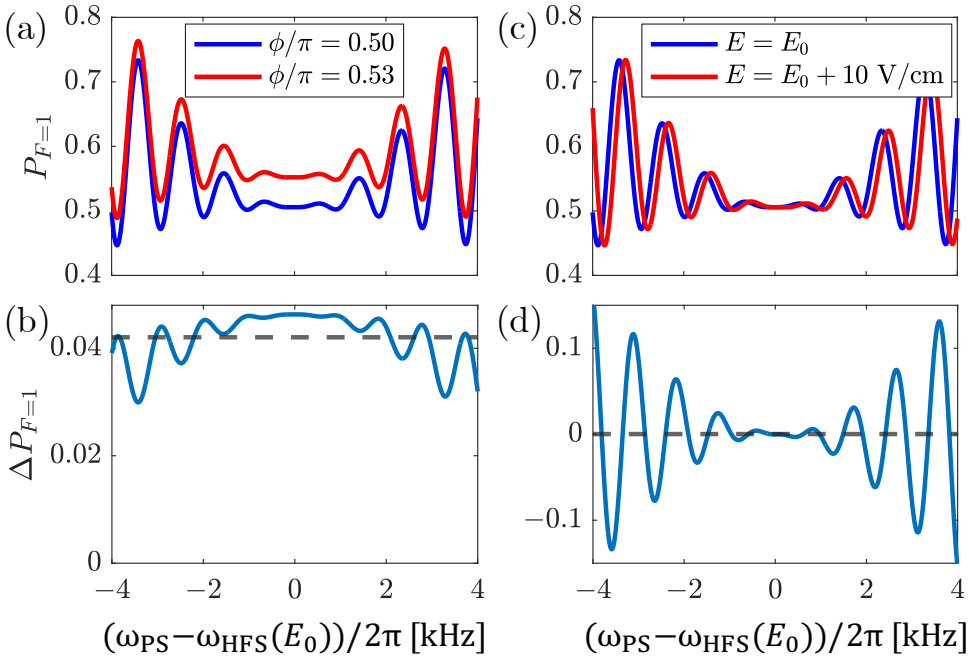

Figure 5.15: (a) Calculation of $P_{F=1}$ for different two-photon detuning $\delta = \omega_{PS} - \omega_{\mathrm{HFS}}(E)$ around the working point of the experiment, i.e. $\Omega_{PS}t \approx \pi$, and $E_0 = 2$ kV/cm, for $\phi/\pi = 0.50$ (blue) and $\phi/\pi = 0.53$ (red). (b) The difference between the red and blue curves in (a), i.e. $\Delta P_{F=1}$ for a change of $\Delta\phi = 0.03\pi$ as function of the detuning. At $\delta = 0$, $P_{F=1} \approx \sin^2(\phi/2)$ and therefore $\Delta P_{F=1} \approx \Delta\phi/2$. The dotted line is $P_{F=1}$ averaged over the interval $\delta = -4$ kHz to $\delta = 4$ kHz. (c) $P_{F=1}$ as function of δ for $\Omega_{PS}t \approx \pi$ and $\phi = \pi/2$, for electric fields $E = E_0$ (blue) and $E = E_0 + 10$ V/cm (red). A change in the electric field results in a shift of the spectrum, for an electric-field dependence of the tensor Stark shift ω_{tensor} of 14.9 kHz/(kV/cm). (d) The difference between the red and blue curves in (b), i.e. $\Delta P_{F=1}$ for a change of electric field $\Delta E = 10$ V/cm. This provides the sensitivity to the externally applied electric field due to $\omega_{\mathrm{tensor}}(E)$. The average value (dotted line) remains zero in this case. The large values of $\Delta\phi$ and ΔE are chosen for visibility. Figure and caption from [46].

5.5 Conclusion

We have shown that the first generation of the NL-eEDM experiment has been successfully built and the ideal working points for the experiment have been established. Many systematic effects have been analysed and their effects on the complex spin precession spectrum have been quantified using an analytical description and comparison with calculations using the optical Bloch equations. The particularly useful part of this technique is that it requires fewer auxiliary measurements to measure the parameter changes, as this information is gained from the spin precession spectrum itself without losing significant EDM sensitivity.

The analytical description is limited in that it only includes the 3 ground state sublevels $|N = 0, F = 1, m_F = \pm 1\rangle$ and $|N = 0, F = 0, m_F = 0\rangle$, whereas the OBE calculations include many more. In addition, potential shifts from the AC Stark shift (light shift) are not included in the description, although due to the large detuning Δ, any light shift experienced is very small. Furthermore, the light shift cancels with a well-defined ratio of S and P as described in [45]. If the OBE calculations are defined numerically, they can be used to fit the experimental data to replace the analytical fit currently used, although this would take much more computing power.

This entirely optical spin precession method is firstly useful for EDM experiments and can additionally be used to measure molecular properties such as rotational and hyperfine frequency splittings with $\mathcal{O}$(Hz) precision, as well as the (tensor) Stark shift of energy levels in an electric field to an unprecedented precision. The experiment is now ready for long term data taking in order to obtain the first eEDM limit using BaF.

Chapter 6

Summary and outlook: an eEDM measurement using BaF

6.1 Summary of thesis

The search for new physics to fully understand all observations of the universe (such as the three generations of particle, the origin of fundamental symmetry violations and the large number of free parameters in the SM) involves many Beyond-the-Standard-Model theories. Proposed models are constrained by either directly measuring the exotic particles of whose existence they speculate, or measuring the novel effects the models or exotic particles produce. These complimentary methods limit the parameter spaces that models occupy, and in some cases lead to a rejection of the model.

In an eEDM investigation, such as the NL-eEDM collaboration which has been the subject of this thesis, the experiment measures a combination of many CP violating effects [99]. In order to differentiate the eEDM from other sources of CP violation, many experiments probing a variety of different systems have been set up around the world. **Chapter 1** gives a general introduction and an overview of the context of our collaboration within the field of experiments attempting to probe the eEDM. In addition, a summary of the further reading from published work and theses is provided in order to place the work of this thesis within the NL-eEDM collaboration.

In **Chapter 2**, the approach of the NL-eEDM experiment itself is introduced. Its basic concept is a double differential experiment that uses spin precession to extract the EDM value. The BaF molecule and its features are described, as well as the particular molecular states and transitions used within this work. The place that this thesis has within the context of the wider NL-eEDM collaboration is described in this chapter. The essential ingredients towards an eEDM measurement that are described include:

- Calculations of the dynamical evolution of the quantum mechanical description of BaF in external electric and magnetic fields using optical Bloch equations.
- The production of BaF molecules, for which the supersonic source is used in this work.

- Probing and manipulating the energy levels of BaF with laser light.
- The homogeneous magnetic and electric field region in which the spin precession takes place.
- The control and measurement of systematic effects.
- The data acquisition system to combine the datastream of many devices.

In **Chapter 3**, the first experimental results of this work are given. The techniques for probing population, signal processing and normalisation, hyperfine and rotational optical pumping, and frequency control are described and their results are shown. An investigation of the velocity and width of the molecular beam is shown. The optical setup for the coherent state transfer pulses is described and the data acquisition system (and associated timings) that combines information from various devices is discussed.

Chapter 4 covers the spectroscopic techniques employed to probe the particular molecular states that are used in the NL-eEDM measurement. Spectroscopy was undertaken to obtain both wide frequency scans ($\mathcal{O}(10)$ GHz) to measure vibrational and rotational splittings, and narrow frequency scans ($\mathcal{O}(100)$ MHz) to precisely extract hyperfine splittings for the $X^2\Sigma^+(v = 0, 1, 2, N = 0, 1, 2, 3, 4, 7)$ ground state levels and low lying $A^2\Pi_{1/2}(v' = 0, 1, J' = 1/2(-)\ -3/2(-)$ and $A^2\Pi_{3/2}(v' = 0, J' = 3/2(-)\ -5/2(-))$ excited state levels.

In **Chapter 5**, the results obtained using spin precession are given. The effect of both the magnitude and orientation of the magnetic fields are discussed, as well as the light shift effect. The interaction zone allows precession times of $\mathcal{O}$(ms) in a homogeneous field region. The eEDM is searched for by first preparing the BaF molecules in a superposition state of the $F = 1, m_F = \pm 1$ sublevels of the $X^2\Sigma^+(v = 0, N = 0)$ ground state with customisable laser pulse. The superposition then precesses in a region of homogeneous magnetic field and electric field with an alternating direction. The superposition is then read out with a second laser pulse and the final population distribution over the $F = 0$ and $F = 1$ levels is analysed to test for a potential EDM.

The change of the spin precession spectra due to variations of parameters are explained in this chapter by testing with both single and double laser pulse setups. The rotation of the effective Rabi pulse by changing the intensity or timings of a single laser pulse are shown. Experiments using the double pulse setup are employed to characterise the systematic effects that laser light intensity, electric field or magnetic field change can produce. These effects are quantifiable by using a model function in addition to comparison with the OBE and are therefore controllable in the extraction of an eEDM.

This experiment is the first in the history of EDM searches where the preparation and analysis of the system takes place with laser light counter-propagating with a molecular beam. This combined with a long homogeneous interaction zone gives excellent parameter resolution that enables the restriction of the possible systematic effects while simultaneously probing the EDM. This thesis has prepared the spectroscopy background for the ongoing first search experiments for an EDM on the electron by the NL-eEDM collaboration.

6.2 Outlook of the NL-eEDM Experiment

6.2.1 Improving statistics with supersonic beam

The molecular flux in each pulse varies greatly and on average reduces over time in the supersonic source as can be seen in Figures 3.15(a) and 3.19. As the barium target rotates, we observe variation as the laser ablation hits a new spot. In addition, repositioning the laser ablation on the target or changing the laser ablation power gives inconsistent changes to the signal we observe, with rates of $\mathcal{O}(10)$ times higher than average observed for short periods of a few minutes. Optimisation of the supersonic source parameters was previously done in [40], and since that investigation the source has been moved, attached to the rest of the experiment, and many of the parameters have changed, i.e.: the gas pressure, the laser ablation power, the rotation speed of the target and the focusing of the ablation laser on the target. With re-optimisation of the ablation parameters, a more consistently high molecular flux would be achieved by the supersonic source.

Additional signal can be obtained by rotationally pumping more molecules from other rotational and vibrational states into the $N = 0$ ground state. We already do this as shown in Section 3.4.4 for $N = 2 \rightarrow N = 0$ and more levels can be included as the source populates many low lying vibrational and rotational levels. In addition, odd N levels can be rotationally pumped into $N = 0$, bypassing the parity selection rules, by using a small electric field to mix the parity levels of the $A^2\Pi_{3/2}(v', J')$ levels. An order of magnitude could feasibly be obtained in the population of the $N = 0$ ground level by rotationally cooling up to $N = 5$, but this would involve a lot of different laser frequencies. This process would be easier with a rotationally colder source (e.g. the cryogenic source) where the lowest levels have a higher percentage of the overall population distribution.

Optical cycling of the detection transition has been shown in other experiments [100] to increase signal to noise ratio by detecting multiple photons per molecule while not losing spin precession information. In our case, optical cycling of the $X^2\Sigma^+(v = 0, N = 0, F = 1) \rightarrow A^2\Pi_{3/2}(v' = 0, J' = 3/2, F' = 2)$ transition used for probing the population of the $F = 1$ hyperfine sublevel of the ground state would have the same effect. Optical cycling of transitions from the $N = 1$ ground state have been previously shown [101] and is presently being worked on for laser cooling as part of the NL-eEDM experiment.

6.2.2 Contrast measurement

The definition of the contrast used to compare to the probability of finding a molecule in a particular state in the population distribution analysis is given in Section 5.2.2. In Figure 6.1, a spectrum is shown where the populations of both the $F = 0$ and $F = 1$ sublevels of the $X^2\Sigma^+(v = 0, N = 0)$ ground state have been probed and plotted in the same figure. In this case each energy level was probed in separate experiments.

Fluctuations in, for example, molecule number from the supersonic source or probing laser light intensity would be overcome by measuring the population at region D of both of the $F = 0, 1$ sublevels of the $X^2\Sigma^+(v = 0, N = 0)$ ground state simultaneously for every molecular shot. The asymmetry of the population is straightforward

to extract in this case in comparison to the current method applied in the experiment. The normalisation process of the signal is also greatly simplified, as well as the understanding of the Rabi phase.

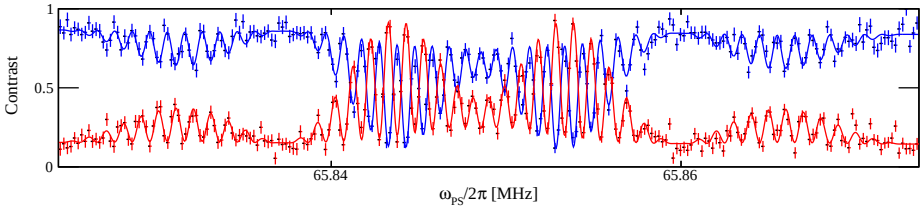

Figure 6.1: Interference plot showing the contrast (which is 1 when the probability of finding a molecule in the $F = 1$ state is 100%) versus the frequency difference in the overlapped laser beam pulses when probing either $F = 0$ (blue) or $F = 1$ (red). The two histograms are not perfect inversions of each other as they were not taken simultaneously.

6.2.3 Electric field switching

For the double differential experiment described in Section 2.2.1, the electric field direction must be switched, which is not described in this thesis but is described in [18, 44]. The ideal switching time for the averaging of the statistics must be balanced with the requirements of the experiment for the time to charge the electric field plates and their stability.

Allan variance calculations (as described in Appendix A) can be used to optimise how long to keep certain parameters, such as the electric field direction, constant for eEDM analysis. A form of this processing was also used to probe the frequency distribution with different averaging times in Figure 3.7. By probing the count rate distribution with different averaging times, we can find ideal averaging time. Initial tests have shown that the time should be less than $<<$ 1 minute, as this is approximately the rotation time of the target which creates a lot of noise in the count rate of the molecular signal. Other sources of noise can be identified using this technique.

The optimised switching time for count rate averaging is balanced with ergonomic requirements of electric field plate charging times to optimise the switching rate. Switching too fast can introduce sparking and magnetic fields inside the interaction zone. The current plate charging times, set by the total resistance and capacitance formed by the field plates, cables and feedthroughs used in the electronics, is $RC =$ 250 ms.

6.2.4 A phase sensitive measurement

Frequency is used as the horizontal axis in the spin precession spectra rather than the laser beam phase, although the measurement is phase sensitive. The uncertainty of the frequency originates from the phase noise from the signal generators. The current setup gives high accuracy from $\mathcal{O}$(mrad) to $\mathcal{O}$(400 krad). If this uncertainty limits the experimental sensitivity, the signal generators can be upgraded to reduce the phase noise.

6.2.5 Frequency comb

The frequency of up to 8 lasers is simultaneously controlled by the WLM as described in Section 3.3.6, and no calibration of the WLM device is used. We observe a frequency stability of <MHz over 12 hours (see Section 3.3.6.1). Frequency calibration is done by spectroscopy for new experiment runs. If greater precision is required, the frequency comb can be used for frequency control of the laser light.

6.2.6 Experiment run time

The statistical precision is described in Equation 1.2, and depends on the total number of molecules detected in the experiment. Running the experiment for longer increases this total number and therefore improves the precision.

The current stability of the experiment is $>$ 24 hours with automised electric field direction switching and constant timing parameters. Low maintenence is required and the code of the DAQ system as described in [44] is reliable and stable. An experiment run of around 2 weeks has recently been completed and experience of how to run the experiment has been collected. Running the experiment for longer will allow the statistical uncertainty to further reduce.

6.2.7 Slow, bright, cold beam of BaF

The upgrade of the NL-eEDM experimental setup is predicted to create a substantial improvement of around 100$\times$ for the number of molecules per pulse (from cryogenic source vs supersonic source) and around a 20$\times$ longer interaction time [41]. The upgraded setup described in [39] is shown in Figure 6.2. The individual components depicted already exist or are presently being developed. The supersonic source is replaced by a combination of a cryogenic source, a molecular lens for beam brightness enhancement, a Stark decelerator for longitudinal slowing, and transverse laser cooling for phase space density increase. The molecules will arrive at the interaction zone in a cold, bright beam pulse travelling with an average velocity of 30 ms^{-1}, in comparison to the 580 ms^{-1} velocity from the supersonic source.

In order to compare the NL-eEDM experiment using the supersonic source versus the planned upgrade, the repetition rate of the experiment should be included in Equation 1.2. Different sources have different velocity spreads $\frac{\Delta v}{v}$, and this must be taken into account in the NL-eEDM experimental procedure when upgrading the beam intensity. Any upgrade to the NL-eEDM has to take these effects in combination with the brighter, colder and slower beam to attain an improved sensitivity.

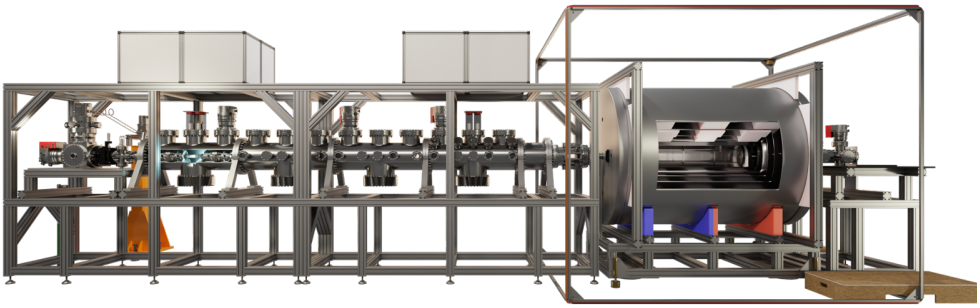

Figure 6.2: The planned upgraded experimental setup for the NL-eEDM collaboration [39], consisting of a cryogenic source of BaF molecules (leftmost), molecular lens (next), Stark Decelerator (long middle region), laser cooling and state preparation (immediately after), magnetic shield (as described in this work) encasing the interaction zone where the superposition precession takes place, and ending in a detection region (rightmost part of the beamline). The magnetic shield is inside three large pairs of rectangular compensation coils which reduce the environmental magnetic field on average to below 10% of the earth's field. Figure taken from [44].

6.2.8 eEDM Limit

The electric field (see Figures 5.14 and 5.15) has been shown using OBE to require a fractional uncertainty of $\Delta E/E < 4 \times 10^{-6}$ to obtain a precision of $d_e = 10^{-27}$ $e$cm. Similar limits have been derived for parameters such as intensity, magnetic field, detunings and pulse timings and their working-point sensitivities are shown in Table 5.1 of [45].

Following the discussion from Sections 5.3-4 of [45], we make an estimation of the statistical sensitivity we can achieve based on the current working experimental setup conditions, and then another estimation including the improvements of the setup.

The total detection efficiency is $\epsilon = 2.8 \times 10^{-3}$. For a detected photon number per pulse of 100, there are therefore a total number of molecules per pulse of 3.6×10^4. At a repetition rate of 10 Hz we have 864000 pulses per day. An electric field of $E = 5$ kV/cm gives the molecular polarisation factor $P(E) \approx 0.35$. Combining these values with a precession time of $T = 1$ ms and $E \cdot A = 6.5$ GV/cm [102] yields a current statistical eEDM sensitivity of

$$\sigma_{d_e} \approx 3 \times 10^{-26}\ e\text{cm day}^{-1}. \tag{6.1}$$

The detection solid angle and quantum efficiency of the detection devices can be feasibly improved to increase the efficiency to obtain $\varepsilon \approx 0.01$. In addition, optical cycling can improve the sensitivity as described in [45]. The number of molecules per pulse can be increased $10\times$ to 10^5 by optimising the operating conditions of the supersonic source such as the gas pressure, ablation laser spot size and target rotation speed. Doubling the repetition rate has also been previously shown to work for the

supersonic source, and can be even higher with geometry optimised for the pumping of the seed gas load.

In addition, slower molecules from the cryogenic source with a significantly higher flux would also increase the precession time to about $T = 3$ ms. Using an electric field of $E = 10$ kV/cm, which in preliminary tests has been proven to be achievable, gives $P(E) \approx 0.5$. A combination of these improvements gives a competitive [10, 21, 103] estimated statistical sensitivity of

$$\sigma_{d_e} \approx 5 \times 10^{-28}\ e\text{cm day}^{-1}. \tag{6.2}$$

A further slowed and bright molecular beam using the Stark decelerator, laser cooling and molecular lensing promises an even more stringent limit on the eEDM.

Chapter 7

Nederlandse Samenvatting

De zoektocht naar nieuwe natuurkunde om alle waarnemingen van het universum volledig te begrijpen (zoals 3 deeltjesgeneraties, de oorsprong van fundamentele symmetriebreking en het grote aantal vrije parameters in het standaardmodel) omvat veel theorieën voorbij het Standaardmodel. Voorgestelde modellen worden begrensd door het direct meten van de exotische deeltjes waarvan deze het bestaan suggereren, of door het meten van de nieuwe effecten die de modellen of exotische deeltjes produceren. Deze complementaire methoden beperken de parametergebieden die modellen innemen, en leiden in sommige gevallen zelfs tot het uitsluiten van het model.

Een niet-nul permanente elektrische dipool moment (EDM) zou zowel de pariteit (P) en tijdsomkeer (T) symmetrie schenden, evenals de gecombineerde ladingconjugatie (C) en pariteit-symmetrie in het geval van het gecombineerde CPT-theorema. Het EDM wordt in het standaardmodel voorspeld om niet-nul doch klein te zijn, terwijl het voor sommige modellen vele ordes van grootte groter kan zijn. Het EDM van het elektron (eEDM) is een van de observabelen die wereldwijd in veel verschillende atomaire, moleculaire en ionische systemen worden getest. EDM's op deeltjes van hogere generaties (bijv. muonen en hyperonen) zijn ook interessant voor het vakgebied. Het is essentieel om een dergelijke observabele in verschillende omstandigheden en systemen te onderzoeken, aangezien elk experiment eigen systematische fouten zal hebben.

In een eEDM onderzoek, zoals de NL-eEDM collaboratie die het onderwerp van deze scriptie is geweest, meet het experiment een combinatie van veel CP-schendende effecten [99]. Om het eEDM te onderscheiden van andere bronnen van CP-schending, zijn over de hele wereld veel experimenten opgezet die verschillende systemen onderzoeken. **Chapter 1** geeft een algemene inleiding en een overzicht van de context van onze collaboratie binnen het veld van experimenten die proberen het eEDM te onderzoeken. Daarnaast wordt in dit hoofdstuk een samenvatting gegeven van verder lezen uit gepubliceerd werk en scripties om het werk van deze scriptie binnen de NL-eEDM collaboratie te plaatsen.

In **Chapter 2** wordt de aanpak van het NL-eEDM experiment zelf geïntroduceerd. Het basisconcept is een dubbel differentieel experiment dat spinprecessie gebruikt om de EDM waarde te extraheren. Het BaF molecuul en zijn kenmerken worden

beschreven, evenals de specifieke moleculaire toestanden en overgangen die in dit werk worden gebruikt. De plaats die deze scriptie inneemt binnen de bredere context van de NL-eEDM collaboratie wordt beschreven in dit hoofdstuk. De essentiële ingrediënten voor een eEDM meting die worden beschreven, omvatten:

- Berekeningen van de dynamische evolutie van de kwantummechanische beschrijving van BaF in externe elektrische en magnetische velden met behulp van optische Bloch vergelijkingen.
- De productie van BaF moleculen, waarvoor in dit werk de supersonische bron wordt gebruikt.
- Het onderzoeken en manipuleren van de energieniveaus van BaF met laserlicht.
- Het homogene magnetische en elektrische veldgebied waarin de spinprecessie plaatsvindt.
- De controle over en meting van systematische effecten.
- Het data-acquisitiesysteem om de datastroom van meerdere apparaten te combineren.

In **Chapter 3** worden de eerste experimentele resultaten van dit werk gegeven. De technieken voor het onderzoeken van populatie, signaalverwerking en normalisatie, hyperfijn en rotationeel optisch pompen, en frequentieregeling worden beschreven en hun resultaten worden getoond. Een onderzoek naar de snelheid en breedte van de moleculaire bundel wordt getoond. De optische opstelling voor de pulsen voor coherente toestandsoverdracht wordt beschreven en het data-acquisitiesysteem (en bijbehorende timing) dat informatie van verschillende apparaten combineert, wordt besproken.

Chapter 4 behandelt de spectroscopische technieken die worden toegepast om de specifieke moleculaire toestanden te onderzoeken die worden gebruikt in de NL-eEDM-meting. Spectroscopie werd uitgevoerd om zowel brede frequentiescans ($\mathcal{O}$(10 GHz)) te verkrijgen om vibratie- en rotatiesplitsingen te meten, als smalle frequentiescans ($\mathcal{O}$(100 MHz)) om hyperfijnsplitsingen nauwkeurig te extraher en voor de $X^2\Sigma^+(v = 0, 1, 2,\ N = 0, 1, 2, 3, 4, 7)$ grondtoestand niveaus en laagliggende $A^2\Pi_{1/2}(v' = \ 0, 1, J' = 1/2(-) - 3/2(-)$ en $A^2\Pi_{3/2}(v' = 0, J' = 3/2(-) - 5/2(-))$ aangeslagen toestandsniveaus.

In **Chapter 5** worden de resultaten gegeven die zijn verkregen met behulp van spinprecessie. Het effect van zowel de grootte als de oriëntatie van de magnetische velden wordt besproken, evenals het lichtverschuivingseffect. De interactiezone maakt precessietijden van $\mathcal{O}$(ms) mogelijk in een homogeen veldgebied. Het eEDM wordt gezocht door eerst de BaF moleculen voor te bereiden in een superpositietoestand van de $F = 1, m_F = \pm 1$ subniveaus van de $X^2\Sigma^+(v = 0, N = 0)$ grondtoestand met aanpasbare laserpuls. De superpositie precessieert vervolgens in een gebied van homogeen magnetisch veld en elektrisch veld met een wisselende richting. De superpositie wordt vervolgens uitgelezen met een tweede laserpuls en de uiteindelijke

populatiedistributie over de $F = 0$ en $F = 1$ niveaus wordt geanalyseerd in een test voor een mogelijk EDM.

De verandering van de spinprecessiespectra als gevolg van variaties van parameters wordt in dit hoofdstuk uitgelegd door testen met zowel enkele als dubbele laserpulstopstellingen. De rotatie van de effectieve Rabi-puls door de intensiteit of de timing van een enkele laserpuls te veranderen, wordt getoond. Experimenten met de dubbele pulstopstelling worden gebruikt om de systematische effecten te karakteriseren die kunnen worden veroorzaakt door veranderingen in laser intensiteit, elektrisch veld of magnetisch veld. Deze effecten zijn kwantificeerbaar door het gebruik van een modelfunctie naast vergelijking met de optische Bloch vergelijkingen en zijn daarom controleerbaar tijdens de extractie van een eEDM.

Dit experiment is het eerste in de geschiedenis van EDM zoektochten waar de voorbereiding en analyse van het systeem plaatsvinden door laserlicht dat tegen de moleculaire bundel in propageert. Dit, in combinatie met een lange homogene interactiezone, geeft uitstekende parameterresolutie die het mogelijk maakt om de mogelijke systematische effecten te beperken, terwijl tegelijkertijd het EDM wordt onderzocht. Deze scriptie heeft de spectroscopieachtergrond voorbereid voor de lopende eerste experimenten naar een EDM op het elektron door de NL-eEDM collaboratie.

Chapter 8

Acknowledgements

Over the course of this PhD, many people have supported, mentored and taught me. I would like to in particular thank my supervisor **Lorenz Willmann** for teaching me everything from how to work in the lab, to how to think about science. Your instinctive knowledge of experimental physics has had a real impact on me. Thank you for teaching me how to always ask "what is the problem you want to solve?". This I will take with me throughout the rest of my career.

Thank you also to **Klaus Jungmann**, especially for his extensive and speedy reading of this thesis. I would often get feedback within an hour of me sending the latest version, which is unheard of in academia. I very much enjoyed working with you and hope you enjoy your retirement. In addition, thank you to **Steven Hoekstra**, who originally hired me and provided a lot of personal support, especially at the beginning of my PhD.

Thanks also to my reading committee **Ronnie Hoekstra**, **Tim Langen**, and **Marcel Merk** for taking the time to read and comment on my thesis. A particular thank you to **Marcel**, who was also my Nikhef C3 member. You really helped me in many ways and were always very pleasant and interested in my work.

I enjoyed working in a tight-knit sub-team during my PhD, the 'Fast-Beam-lab', otherwise known as the 'Snelle Bundel Bende'. **Thomas**, my one constant office mate for the last five years, I have really enjoyed working with you. Our long chats over countless breaks and lunches have been really fulfilling. I was very happy to be asked to be your paranymph. **Anno**, thanks for being so much more than a IT-support guy. Writing our theses at the same time means that we have had a lot in common. I am especially grateful that you translated my Nederlandse Samenvatting and my popular dutch summary. Your thesis is going to be one of the best-looking ones ever! Your high standards for yourself inspire me and I know you will go on to do amazing things in your life. **Alexander**, my office mate for a shorter time, thanks for usually being the smartest guy in the room. Your ability to see straight through to the heart of a problem is incredible. I really enjoyed our USA/ Canada trip together, and I hope you enjoy your post-doc in Paris very much. **Parul**, you were the first other PhD student that I worked closely with in the lab in Groningen, and you taught me many things. I really enjoy that we still contact each other every

time something big happens in the cricket world. Your encyclopaedic knowledge of names, numbers and Nobel prize winners will never fail to impress me.

Oliver, thanks so much for building so much of the optics and laser setup. Thanks also for being a great guy to chat with both in the lab and as a super cool DJ. I really liked coming to your shows! **Leo**, thanks for your endless engineering and electronics help. I would have been lost without you in these things. Thanks also for your starring role as the evil villain in the movie we made for Thomas. **Hilde**, thanks for always calmly helping me when I was worrying about an administrative issue. It was very much appreciated. **Roman**, although your time with our collaboration was short, you had a very big impact on me. I hope to feel as competent as you are one day. **Heleen**, it was very nice to share a room with you at the summer school, and I am so glad that you have joined the collaboration now. I hope you have a lot of success in your PhD. Thanks also to the dynamic duo of **Joost** and **Ties**, who are rarely seen apart. You made lunches at the food court and conferences particularly fun. Good luck with the final years of your PhDs!

Thanks very much to all the other people in the NL-eEDM collaboration over the years: **Kevin**, **Artem**, **Yanning**, **Malika**, **Pi**, **Rick**, **Wim**, **Anastasia**, and **Rob**. You have all had a part in developing me as a person as well as with the scientific content of this thesis, and for this I am very grateful.

I have also worked together with many students over the years, and a few really stand out. **Thya, Sander, and Rutger**, who started on the same day as me, I really enjoyed our short time together. **Attie**, my first bachelor student, taught me a lot about working with others. Lunches were considerably less fun when **Hidde** left, as he was always the life of the party. Working with the trio of **Jente**, **Stef** and **Luuk** was particularly productive in the difficult conditions during the pandemic. More recently, both **Tesse**, **Vedang** and **Lisa** stood out as bright stars as bachelor students. I wish you all the best in your futures. **Tesse**, see you at CERN this summer!

In the VSI there are also many people I would like to thank. **Elwin**, **Bart**, **Gerco**, **Julia**, **Steve**, **Kristof** (and your cats), **Mina**, **Yuly**, **Jennifer**, **Eduardus**, **Nikolaos**, **Briain**, **Arif** and **Andrej**, thank you all for creating a friendly and fun environment in which to undertake my PhD. Special thanks in particular to **Eric**, for being an excellent co-organiser of the VSI Christmas quiz for several years.

In Groningen I made excellent friendships that I know will last a lifetime. I would like to especially thank **Kristin**, **Rachael** and **Natalia**. Thanks for the tennis, the movie nights, the dinners, the fancy dress parties, the trips away and so much more. Our friendship has become so much stronger in the few years and I cannot begin to tell you how much that means to me. Special thanks also to my beautiful ladies **Claudia** and **Andrea**, who got me through so much. The hysterical laughter when the three of us together is so important to me and you have really been a lifeline in my time in Groningen. Thanks for teaching me how to sing karaoke in Italian and Spanish and how to cook the best Italian food. Having friends that require no effort or pretence to be around is incredible and we were always like that together. I really love all of you.

My life in Groningen was enhanced so much by the many parties, brunches and dinners with all the biologists, chemists and bio-catalysis people I was friends with during my

time here. To the 'bad-boiz': **Rudy**, **Titia**, **Elyse** and **Roxana**, thank you so much for all of the amazing times we have had over the years. There are too many to count and for that I will always be grateful. Thank you for being there for me in so many ways. You made my time in Groningen so much brighter. **Alessandro**, thanks for always keeping in contact with me for all the F1 and AC Milan news, and for always educating me in the particulars of italian cooking. **Bart**, **Fabrizio**, **Gemma**, **Gwen**, **Saniye**, **Suzanne**, **Cate**, **Eleonora**, **Lars**, **Marta**, **Mathijs**, **Max**, **Cora**, **Michela**, **Valeria** (my cheese-mate), **Rita**, **Franco**, **Friso**, **Laura**, and **Linda**, thanks for all the countless happy times. I have loved spending time with all of you. Thank you also to **Rik**, for all of your kindness.

A huge thank you to my friends back home in the UK. **Jade**, thank you for always knowing me so well, and for all your strength. You're the best. **Sam** and **Jake**, your friendship and your love inspires me so much. **Charlotte** and **Jimmy**, I am so happy that you guys always make such an effort into our long-distance friendship. It is rare and extremely meaningful. I loved being able to be a small part of your wedding. **Jess** and **Luke**, thanks for always making me laugh and for the sheer amount of time we have known each other! It is quite incredible. To **Jonny**, **Robbie**, **Ana** and **Conor**, thanks for making every milestone special and for being such a huge part of my journey not only as a physicist but also as a person. **Oliver**, thanks for knowing since we were born as still being my friend. Life is never boring around you and it never will be.

I am also so thankful for my paranymph, **MD**, who never fails to cheer me up and is a beacon of fun, warmth and is an unending joy to be around. You are an incredibly strong person and I can't wait to visit your family home in Italy one day. I am so glad that we became friends and please never stop sending me funny memes. I am so looking forward to seeing you when you are visiting Geneva! To my other paranymph, **Sylvia**, thanks for being the best person I know. Thanks for being there in my darkest times and my brightest. The amount of effort and love you pour into the people and things you care about will never cease to amaze me. I will sincerely miss us being such close neighbours in my next adventure in Geneva, but you absolutely cannot get rid of me so please expect many phone calls. Also thanks for adopting Mira and letting me be her second mum, which has really brought me so much joy in the last 1.5 years!

Finally, thank you to my family. **Reuben**, my not-so-little brother, thanks for everything. I hope to have many ski trips and visits to Norway in the future. You are such a go-getter and I know you will always be so successful at everything you do. **Dad**, thanks for reading my thesis and finding many typos! You have always inspired me to work hard and to be my true self. Thanks for ferrying me and my belongings around Europe. You find enjoyment in everything you do and you are always reliable in being there when someone is needed, which I appreciate and love so much. **Mum**, thanks for always talking to me on the phone while was I cycling around Groningen. Thanks for your endless empathy and your love. Thanks for indoctrinating me from an early age in science fiction and fantasy and the best music. You introduced me to Dana Scully, Seven of Nine, Kara Thrace, Jadzia Dax and all of the inspirational characters that formed me and my future career. I am so grateful that we have such a strong bond and that you are always there for me.

I could spend another ten pages thanking so many more people, so I will simply end with quotes from two of my favourite authors:

> *"Any road followed precisely to its end leads precisely nowhere. Climb the mountain just a little bit to test that it's a mountain. From the top of the mountain, you can not see the mountain. "*

— Dune, Frank Herbert

> *"There is nothing like looking, if you want to find something. You certainly usually find something, if you look, but it is not always quite the something you were after. "*

— The Hobbit, J.R.R. Tolkien.

Love and thanks,
Ginny

Appendix A

Allan Variance Analysis

The procedure for Allan Variance analysis begins by creating a histogram of the data with specific bin size that is set to be just above the minimum so that there is at least one data point per bin. The histogram is the number of occurrences of the data in each bin.

A loop is setup over the number of powers of two to be investigated. The content of each $i + 1$ bin is subtracted from each i bin, where i begins at the first bin that is filled. A histogram of the differences is then created.

Five numbers are extracted from the histogram of differences: the mean and its error, and the root-mean-square (rms) and its error, and the bin size which is a value in time. These values are stored. The mean can be used to observe possible drifts in the data, supplementary to the allan variance analysis.

At the end of the loop, the dataset is rebinned by a factor of two so the bin sizes are doubled, and the loop continues until the number of powers of two has completed. An example of a set of histograms for which the rms and bin size are extracted for allan variance analysis is shown in Figure 3.7. The total time of the dataset may not be available to analyse if it is longer than the exact time that is a power of 2 of the initial bin size. The rms and its error of the differences data for each bin size is then plotted versus the bin size and this is called the allan variance.

By comparing the change in rms for consecutive bin sizes within the Allan Variance plot, information about the averaging of noise within the experiment can be extracted. We can also understand whether more data points should be taken to allow more averaging by observing if it significantly reduces the rms to take double the data length.

Appendix B

Detection Efficiency of PMTs

PMTs also have a specific quantum efficiency which depends on the laser light frequency. For transitions from the $X^2\Sigma^+(v=0) \rightarrow A^2\Pi_{3/2}$, the Thorlabs PMT1000 series has a typical radiant sensitivity of $40-50$ mA/W, versus the higher wavelength transition $X^2\Sigma^+(v=0) \rightarrow A^2\Pi_{1/2}$ for which the Thorlabs PMT has a typical radiant sensitivity of $10-20$ mA/W. A typical radiant sensitivity from the Hamamatsu H10721-2 [72] for the $X^2\Sigma^+(v=0) \rightarrow A^2\Pi_{3/2}$ transition is $13-14$ mA/W and for the $X^2\Sigma^+(v=0) \rightarrow A^2\Pi_{1/2}$ transition it has a steep gradient drop versus frequency and is approximately $9-11$ mA/W. Detection without photon counting has also been investigated. Here the integrated photon flux is converted to an analogue voltage.

The conversion from sensitivity to an output voltage is defined as

$$\begin{aligned} &\text{Output } (V) \\ &= \text{ Transimpedence Gain}(V/A) \times \text{Sensitivity (A/W)} \\ &\times \text{Gain} \times \text{Input Optical Power } (W). \end{aligned} \tag{B.1}$$

Appendix C

Hyperfine Spectroscopy of BaF

Here all the spectra from Tables 4.3 and 4.4 are depicted. These spectra are each fitted with a model function as described in Section 4.3.3. Each spectrum has splitting parameters extracted from it which are listed in the tables.

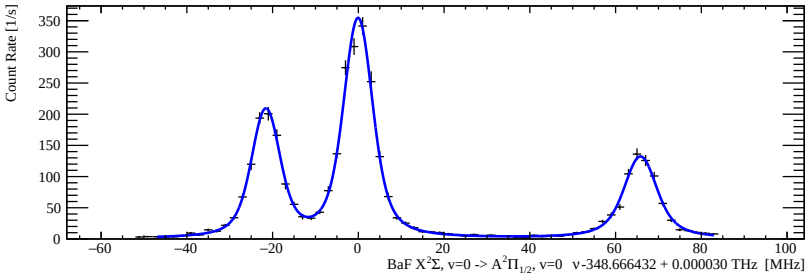

(a)

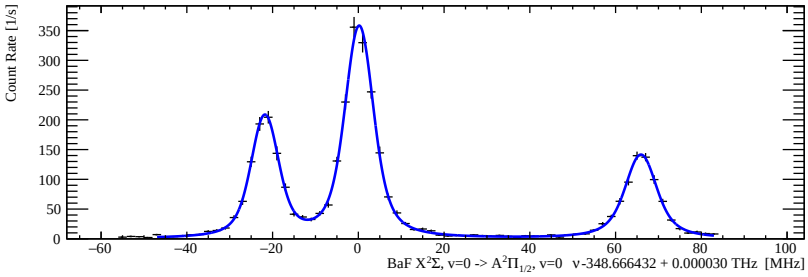

(b)

Figure C.1: Spectra showing the $X^2\Sigma^+(v = 0, N = 0) \rightarrow A^2\Pi_{1/2}(v' = 0, J' = 1/2)$ transition.

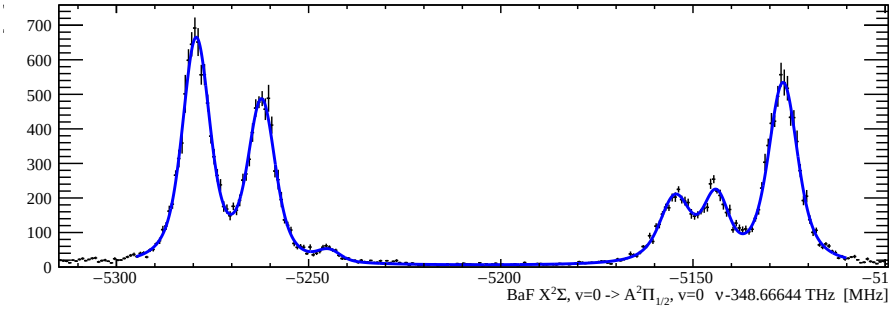

(a)

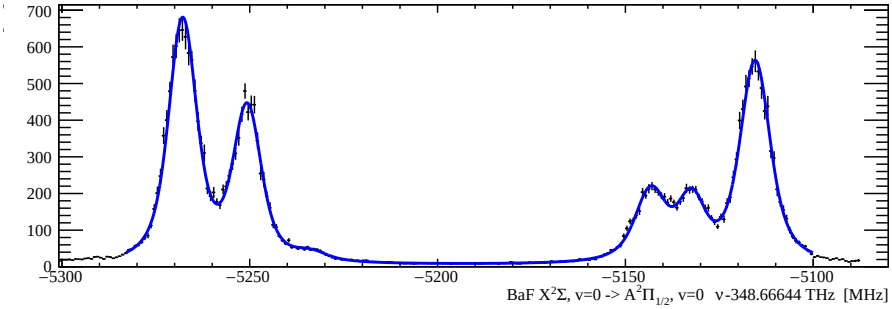

(b)

Figure C.2: Spectra showing the $X^2\Sigma^+(v = 0, N = 1) \rightarrow A^2\Pi_{1/2}(v' = 0, J' = 1/2)$ transition.

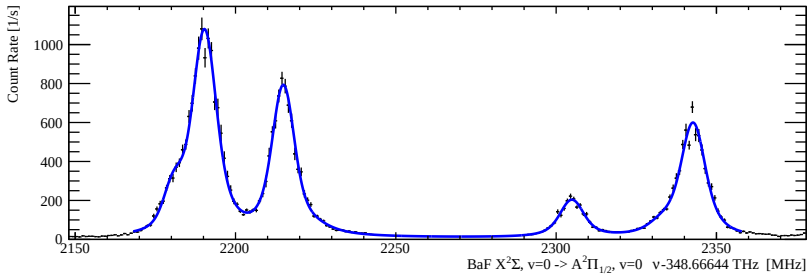

(a)

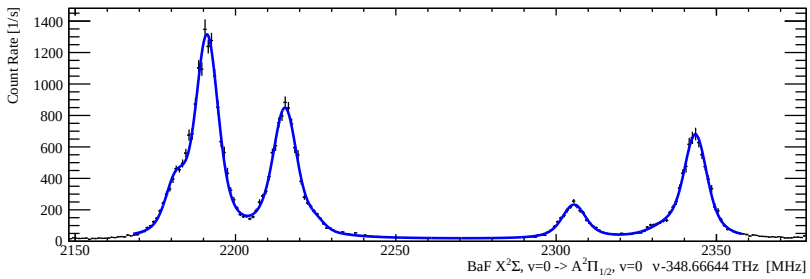

(b)

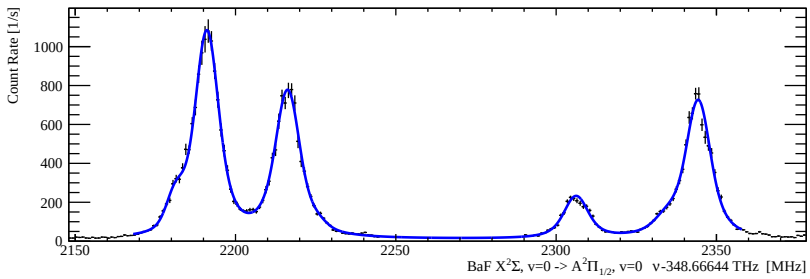

(c)

Figure C.3: Spectra showing the $X^2\Sigma^+(v = 0, N = 1) \rightarrow A^2\Pi_{1/2}(v' = 0, J' = 3/2)$ transition.

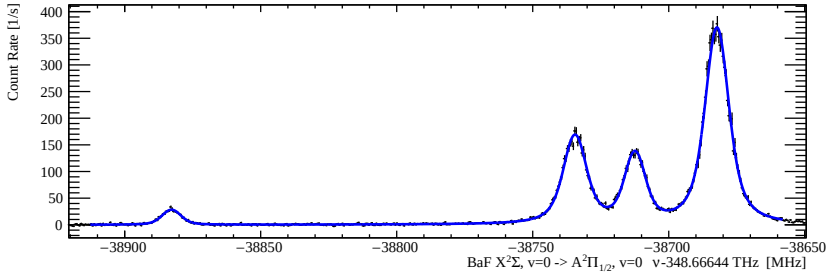

(a)

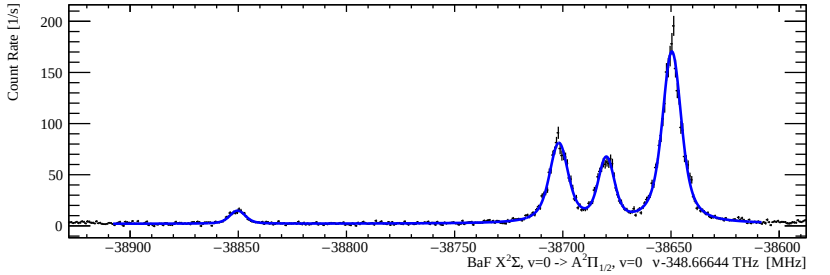

(b)

Figure C.4: Spectra showing the $X^2\Sigma^+(v = 0, N = 2) \rightarrow A^2\Pi_{1/2}(v' = 0, J' = 1/2)$ transition.

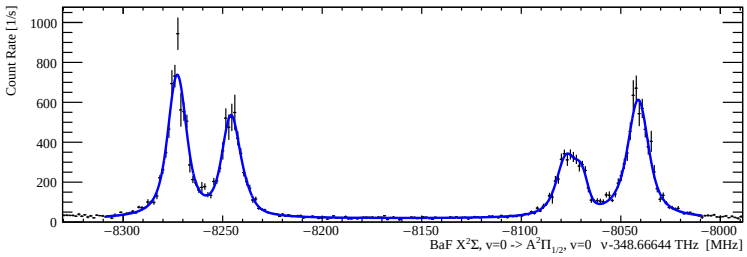

(a)

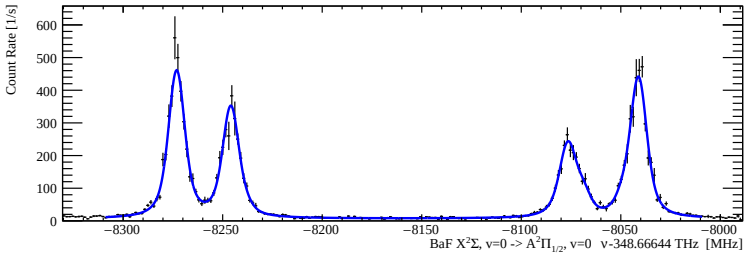

(b)

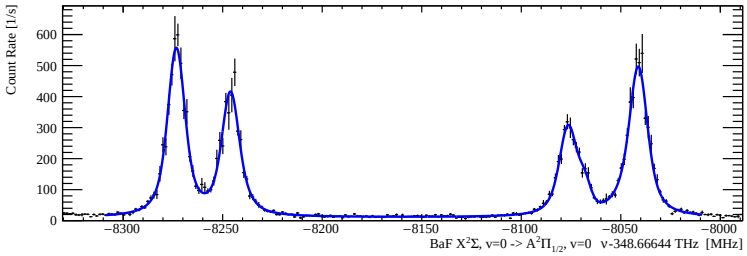

(c)

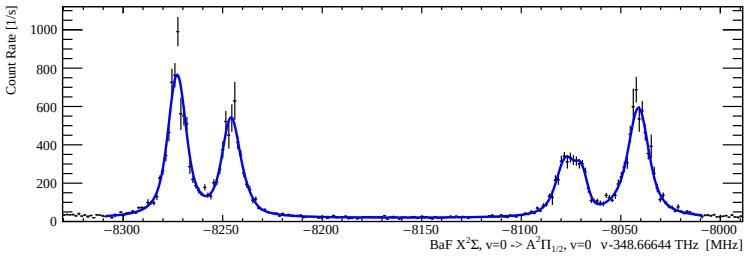

(d)

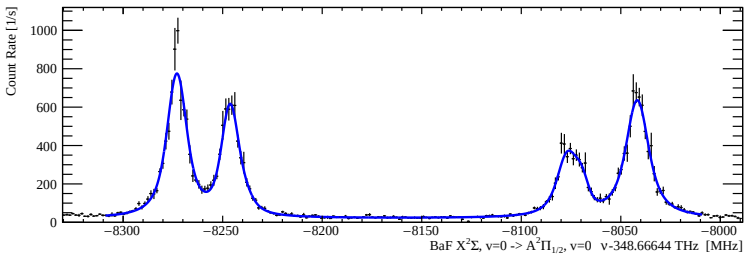

(e)

Figure C.5: Spectra showing the $X^2\Sigma^+(v = 0, N = 2) \rightarrow A^2\Pi_{1/2}(v' = 0, J' = 3/2)$ transition.

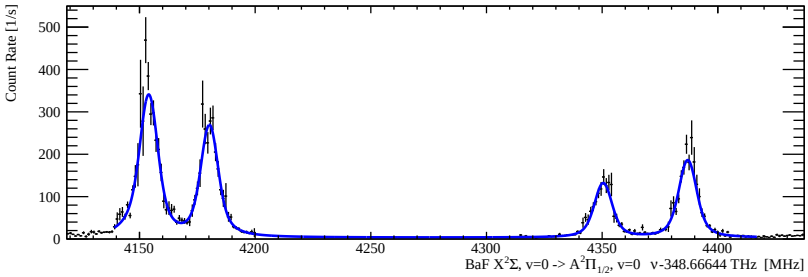

(a)

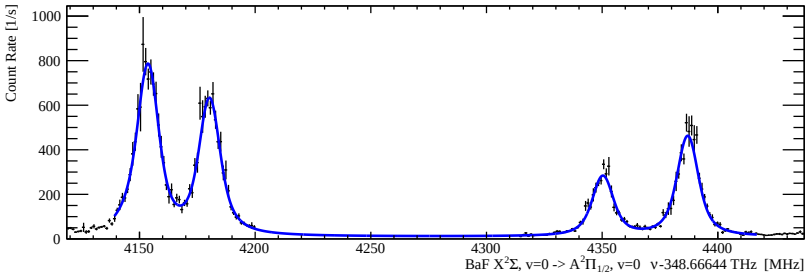

(b)

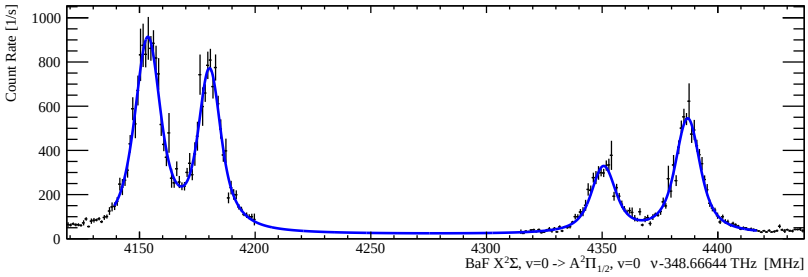

(c)

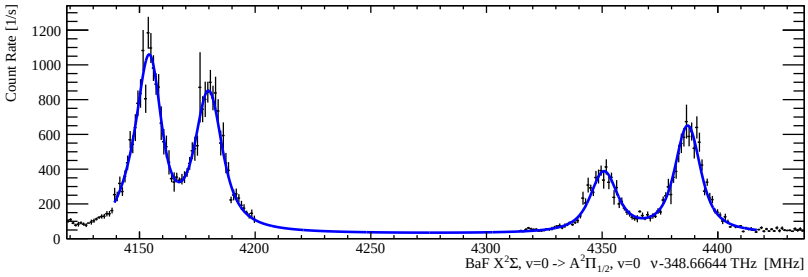

(d)

Figure C.6: Spectra showing the $X^2\Sigma^+(v = 0, N = 2) \rightarrow A^2\Pi_{1/2}(v' = 0, J' = 3/2)$ transition.

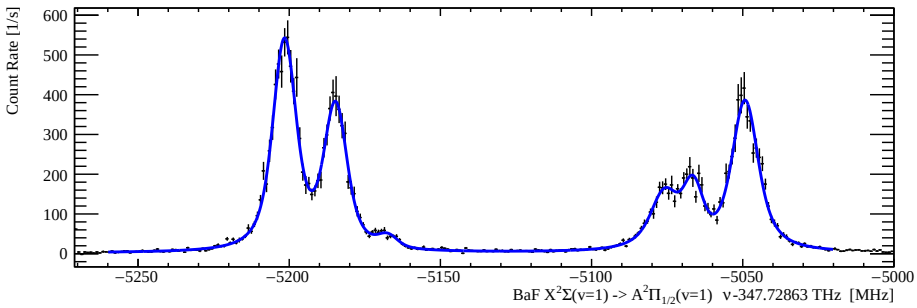

Figure C.7: Spectrum showing the $X^2\Sigma^+(v = 1, N = 1) \rightarrow A^2\Pi_{1/2}(v' = 1, J' = 1/2)$ transition.

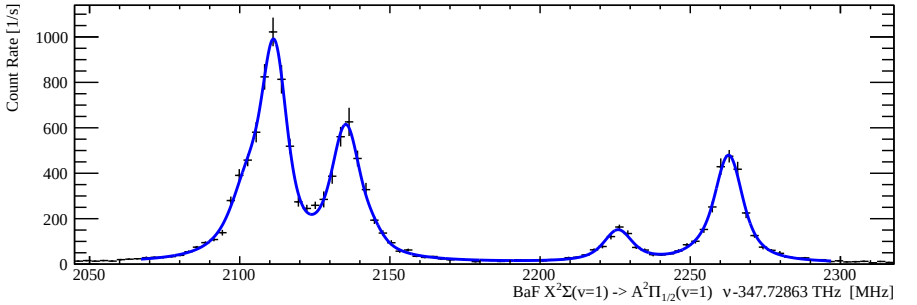

Figure C.8: Spectrum showing the $X^2\Sigma^+(v = 1, N = 1) \rightarrow A^2\Pi_{1/2}(v' = 1, J' = 3/2)$ transition.

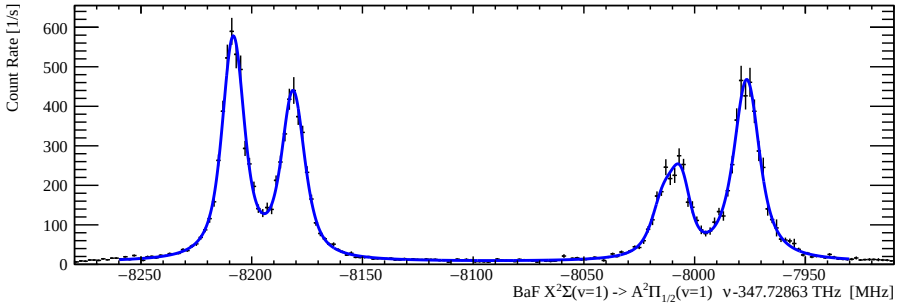

Figure C.9: Spectrum showing the $X^2\Sigma^+(v = 1, N = 2) \rightarrow A^2\Pi_{1/2}(v' = 1, J' = 3/2)$ transition.

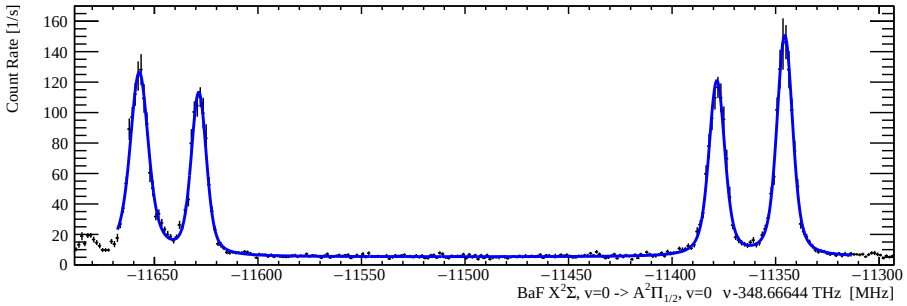

Figure C.10: Spectrum showing the $X^2\Sigma^+(v=0, N=3) \rightarrow A^2\Pi_{1/2}(v'=0, J'=5/2)$ transition.

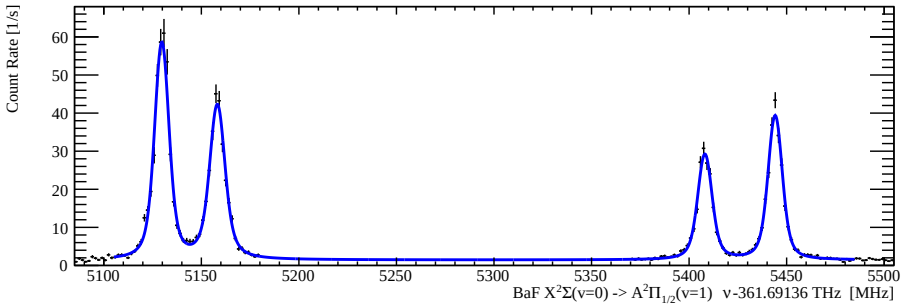

(a)

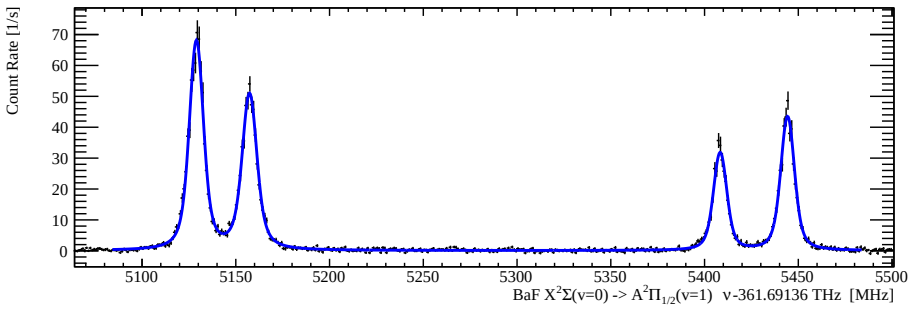

(b)

Figure C.11: Spectra showing the $X^2\Sigma^+(v=0, N=3) \rightarrow A^2\Pi_{1/2}(v'=0, J'=7/2)$ transition.

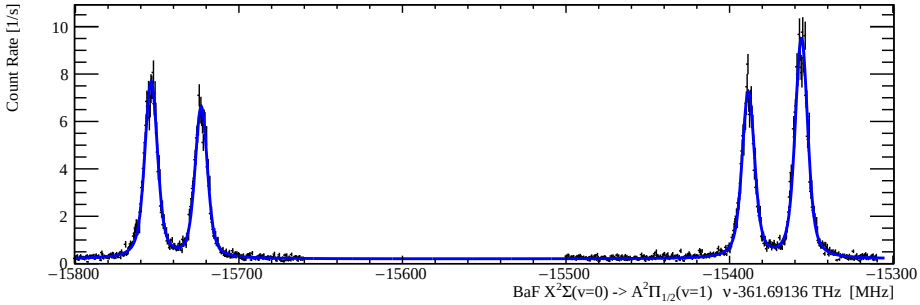

Figure C.12: Spectrum showing the $X^2\Sigma^+(v = 0, N = 4) \rightarrow A^2\Pi_{1/2}(v' = 0, J' = 7/2)$ transition.

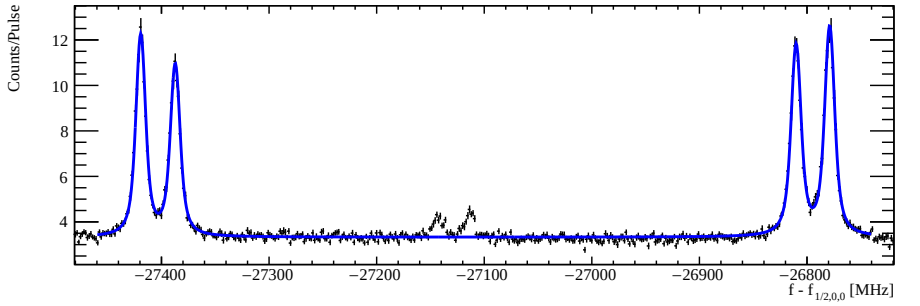

Figure C.13: Spectrum showing the $X^2\Sigma^+(v = 0, N = 7) \rightarrow A^2\Pi_{1/2}(v' = 0, J' = 13/2)$ transition.

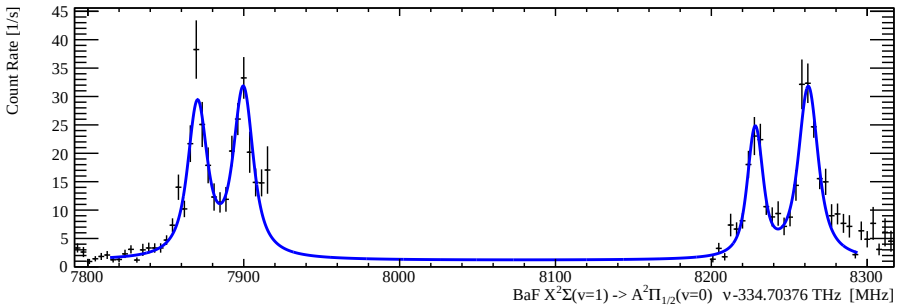

Figure C.14: Spectrum showing the $X^2\Sigma^+(v=1, N=4) \rightarrow A^2\Pi_{1/2}(v'=1, J'=9/2)$ transition.

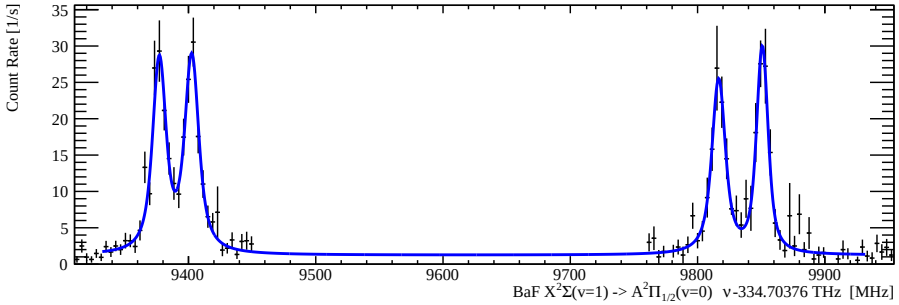

Figure C.15: Spectrum showing the $X^2\Sigma^+(v=1, N=5) \rightarrow A^2\Pi_{1/2}(v'=1, J'=11/2)$ transition.

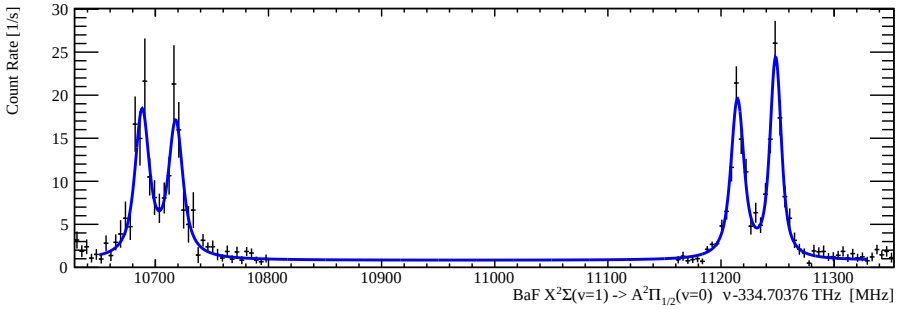

Figure C.16: Spectrum showing the $X^2\Sigma^+(v=1, N=6) \rightarrow A^2\Pi_{1/2}(v'=1, J'=13/2)$ transition.

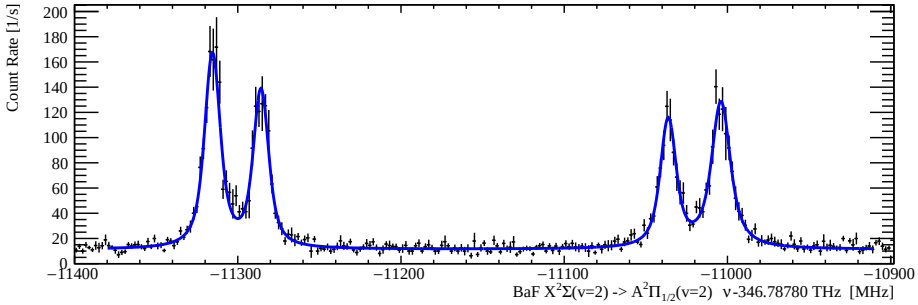

Figure C.17: Spectrum showing the $X^2\Sigma^+(v = 2, N = 3) \rightarrow A^2\Pi_{1/2}(v' = 2, J' = 5/2)$ transition.

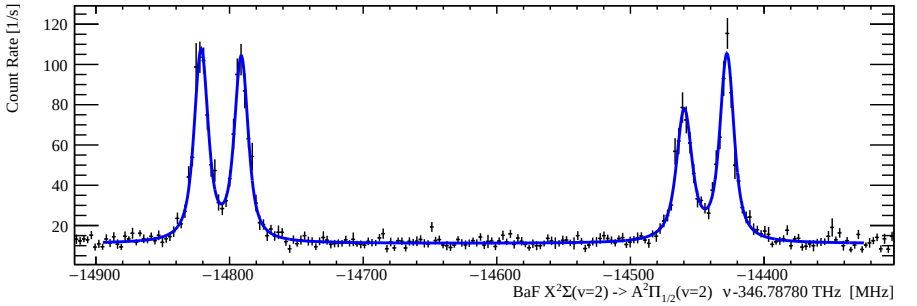

Figure C.18: Spectrum showing the $X^2\Sigma^+(v = 2, N = 4) \rightarrow A^2\Pi_{1/2}(v' = 2, J' = 7/2)$ transition.

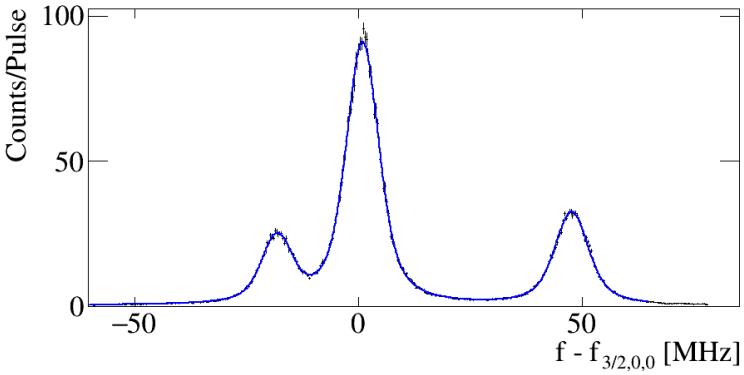

Figure C.19: Spectrum showing the $X^2\Sigma^+(v=0, N=0) \rightarrow A^2\Pi_{3/2}(v'=0, J'=3/2)$ transition.

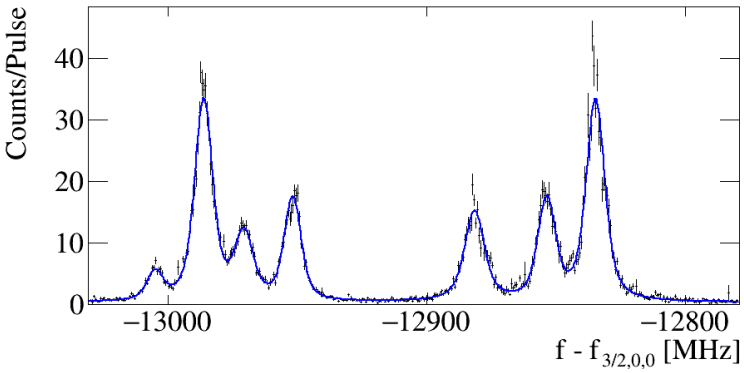

Figure C.20: Spectrum showing the $X^2\Sigma^+(v=0, N=1) \rightarrow A^2\Pi_{3/2}(v'=0, J'=3/2)$ transition.

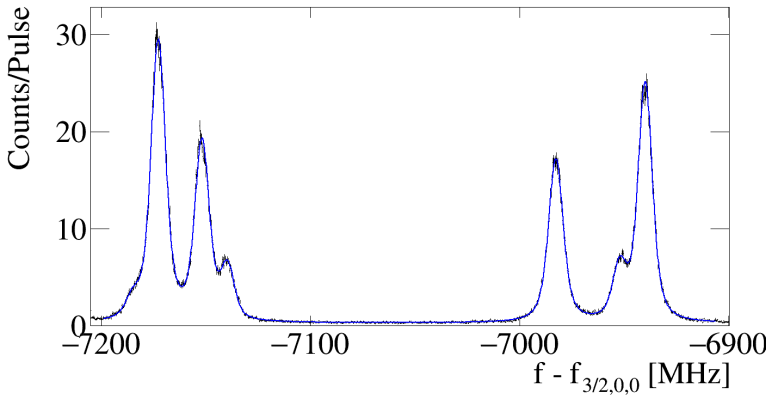

Figure C.21: Spectrum showing the $X^2\Sigma^+(v=0, N=2) \rightarrow A^2\Pi_{3/2}(v'=0, J'=5/2)$ transition.

Bibliography

[1] J. H. Christenson, J. W. Cronin, V. L. Fitch, and R. Turlay. Evidence for the 2π Decay of the K_2^0 Meson. *Phys. Rev. Lett.*, 13:138–140, Jul 1964. doi: 10.1103/PhysRevLett.13.138. URL https://link.aps.org/doi/10.1103/PhysRevLett.13.138. 3

[2] W. Bernreuther and M. Suzuki. The electric dipole moment of the electron. *Rev. Mod. Phys.*, 63:313–340, Apr 1991. doi: 10.1103/RevModPhys.63.313. URL https://link.aps.org/doi/10.1103/RevModPhys.63.313. 3

[3] LHCb collaboration. LHCb Detector Performance. *International Journal of Modern Physics A*, 30(7), 2015. ISSN 0217-751X. doi: 10.1142/S0217751X15300227. URL http://arxiv.org/abs/1412.6352{%}0Ahttp://dx.doi.org/10.1142/S0217751X15300227. 3

[4] M. Pospelov and A. Ritz. Electric dipole moments as probes of new physics. *Ann. Phys.*, 318(1):119–169, 2005. doi: 10.1016/j.aop.2005.04.002. URL https://doi.org/10.1016/j.aop.2005.04.002. 3, 4

[5] Norval Fortson, Patrick Sandars, and Stephen Barr. The Search for a Permanent Electric Dipole Moment. *Physics Today*, 56(6):33–39, Jun 2003. ISSN 00319228. doi: 10.1063/1.1595052. URL http://physicstoday.scitation.org/doi/10.1063/1.1595052. 3

[6] M.E. Pospelov and I.B. Khriplovich. Electric dipole moment of the W boson and the electron in the Kobayashi-Maskawa model. *Sov. J. Nucl. Phys.*, 53:638–640, 1991. URL http://inis.iaea.org/search/search.aspx?orig_q=RN:23084502.

[7] Yuichiro Nakai and Matthew Reece. Electric dipole moments in natural supersymmetry. *Journal of High Energy Physics*, 2017(8):31, Aug 2017. ISSN 1029-8479. doi: 10.1007/JHEP08(2017)031. URL https://doi.org/10.1007/JHEP08(2017)031.

[8] P.G.H. Sandars. Enhancement factor for the electric dipole moment of the valence electron in an alkali atom. *Physics Letters*, 22(3):290 – 291, 1966. ISSN 0031-9163. doi: https://doi.org/10.1016/0031-9163(66)90618-4. URL http://www.sciencedirect.com/science/article/pii/0031916366906184. 3

[9] Yohei Ema, Ting Gao, and Maxim Pospelov. Standard model prediction for paramagnetic electric dipole moments. *Phys. Rev. Lett.*, 129:231801, Nov 2022. doi: 10.1103/PhysRevLett.129.231801. URL https://link.aps.org/doi/10.1103/PhysRevLett.129.231801. 3

[10] Tanya S. Roussy, Luke Caldwell, Trevor Wright, William B. Cairncross, Yuval Shagam, Kia Boon Ng, Noah Schlossberger, Sun Yool Park, Anzhou Wang, Jun Ye, and Eric A. Cornell. An improved bound on the electron's electric dipole moment. *Science*, 381(6653):46–50, 2023. doi: 10.1126/science.adg4084. URL https://www.science.org/doi/abs/10.1126/science.adg4084. 3, 5, 6, 18, 127

[11] S. Abel, S. Khalil, and O. Lebedev. EDM constraints in supersymmetric theories. *Nuclear Physics B*, 606(1):151–182, 2001. ISSN 0550-3213. doi: https://doi.org/10.1016/S0550-3213(01)00233-4. URL https://www.sciencedirect.com/science/article/pii/S0550321301002334. 3

[12] Eugene D. Commins. Electric dipole moments of leptons. In Benjamin Bederson and Herbert Walther, editors, *Advances In Atomic, Molecular, and Optical Physics*, volume 40, pages 1–55. Academic Press, 1999. doi: https://doi.org/10.1016/S1049-250X(08)60110-X. URL https://www.sciencedirect.com/science/article/pii/S1049250X0860110X. 4

[13] O. P. Sushkov and V. V. Flambaum. Parity Violation Effects in Diatomic Molecules. *Sov. Phys. JETP*, 48:608, 1978. URL http://jetp.ras.ru/cgi-bin/dn/e_048_04_0608.pdf.

[14] P.G.H. Sandars. Measurability of the Proton Electric Dipole Moment. *Phys. Rev. Lett.*, 19:1396–1398, Dec 1967. doi: 10.1103/PhysRevLett.19.1396. URL https://link.aps.org/doi/10.1103/PhysRevLett.19.1396.

[15] P. A.B. Haase, Diewertje J. Doeglas, Alexander Boeschoten, Ephraim Eliav, Miroslav Iliaš, Parul Aggarwal, H. L. Bethlem, Anastasia Borschevsky, Kevin Esajas, Yongliang Hao, Steven Hoekstra, Virginia R. Marshall, Thomas B. Meijknecht, Maarten C. Mooij, Kees Steinebach, Rob G. E. Timmermans, Anno P. Touwen, Wim Ubachs, Lorenz Willmann, and Yanning Yin. Systematic study and uncertainty evaluation of P, T-odd molecular enhancement factors in BaF. *Journal of Chemical Physics*, 155(3), Jul 2021. ISSN 0021-9606. doi: 10.1063/5.0047344. URL https://doi.org/10.1063/5.0047344. 4, 6, 9, 10

[16] I.B. Khriplovich and S.K. Lamoreaux. *CP Violation Without Strangeness*. Springer Berlin Heidelberg, 1997. ISBN 9783642645778. doi: 10.1007/978-3-642-60838-4. URL https://dx.doi.org/10.1007/978-3-642-60838-4. 4

[17] I.B. Khriplovich and S.K. Lamoreaux. *CP Violation Without Strangeness*, chapter 3: General Features of EDM Experiments. Springer Berlin Heidelberg, 1997. ISBN 9783642645778. URL https://dx.doi.org/10.1007/978-3-642-60838-4. 4

[18] Thomas Meijknecht. *Electric and Magnetic Field Control for Electric Dipole Moment Searches*. PhD thesis, University of Groningen, 2023. URL https://research.rug.nl/en/publications/electric-and-magnetic-field-control-for-electric-dipole-moment-se. 4, 6, 9, 13, 21, 22, 23, 24, 33, 85, 90, 94, 99, 104, 124

[19] M. V. Romalis and E. N. Fortson. Zeeman frequency shifts in an optical dipole trap used to search for an electric-dipole moment. *Physical Review A - Atomic, Molecular, and Optical Physics*, 59(6):4547–4558, 1999. ISSN 10941622. doi: 10.1103/PhysRevA.59.4547. URL http://physics.princeton.edu/romalis/papers/Romalis{_}1999{_}2.pdf. 4

[20] H. Bethlem, A. Borschevsky, S. Hoekstra, K. Jungmann, R. Timmermans, W. Ubachs, and L. Willmann. Physics beyond the Standard Model with cold molecules: Measuring the electric dipole moment of the electron in BaF. NWO Proposal, 2016. 4

[21] The ACME Collaboration. Improved limit on the electric dipole moment. *Nature*, 2018. doi: 10.1038/s41586-018-0599-8. URL https://doi.org/10.1038/s41586-018-0599-8. 5, 6, 18, 127

[22] J. J. Hudson, D. M. Kara, I. J. Smallman, B. E. Sauer, M. R. Tarbutt, and E. A. Hinds. Improved measurement of the shape of the electron. *Nature*, 473 (7348):493–496, May 2011. doi: 10.1038/nature10104. URL https://doi.org/10.1038/nature10104. 5, 18

[23] W. B. Cairncross, D. N. Gresh, M. Grau, K. C. Cossel, T. S. Roussy, Y. Ni, Y. Zhou, J. Ye, and E. A. Cornell. Precision measurement of the electron's electric dipole moment using trapped molecular ions. *Phys. Rev. Lett.*, 119: 153001, 2017. URL https://link.aps.org/doi/10.1103/PhysRevLett.119.153001. 5

[24] A. C. Vutha, M. Horbatsch, and E. A. Hessels. Orientation-dependent hyperfine structure of polar molecules in a rare-gas matrix: A scheme for measuring the electron electric dipole moment. *Phys. Rev. A*, 98:032513, Sep 2018. doi: 10.1103/PhysRevA.98.032513. URL https://link.aps.org/doi/10.1103/PhysRevA.98.032513. 5, 6, 85

[25] S J Li, H D Ramachandran, R Anderson, and A C Vutha. Optical control of baf molecules trapped in neon ice. *New Journal of Physics*, 25(8):082001, aug 2023. doi: 10.1088/1367-2630/ace9f3. URL https://dx.doi.org/10.1088/1367-2630/ace9f3. 6

[26] I. Kozyryev and N. R. Hutzler. Precision measurement of time-reversal symmetry violation with laser-cooled polyatomic molecules. *Phys. Rev. Lett.*, 119:133002, Sep 2017. doi: 10.1103/PhysRevLett.119.133002. URL http://dx.doi.org/10.1103/PhysRevLett.119.133002. 5

[27] Benjamin L Augenbraun, Zack D Lasner, Alexander Frenett, Hiromitsu Sawaoka, Calder Miller, Timothy C Steimle, and John M Doyle. Laser-cooled

polyatomic molecules for improved electron electric dipole moment searches. *New Journal of Physics*, 22(2):022003, Feb 2020. doi: 10.1088/1367-2630/ab687b. URL https://dx.doi.org/10.1088/1367-2630/ab687b. 6

[28] Y. J. Kim, C.-Y. Liu, S. K. Lamoreaux, G. Visser, B. Kunkler, A. N. Matlashov, J. C. Long, and T. G. Reddy. New experimental limit on the electric dipole moment of the electron in a paramagnetic insulator. *Phys. Rev. D*, 91:102004, May 2015. doi: 10.1103/PhysRevD.91.102004. URL https://link.aps.org/doi/10.1103/PhysRevD.91.102004.

[29] S. Eckel, A. O. Sushkov, and S. K. Lamoreaux. Limit on the electron electric dipole moment using paramagnetic ferroelectric $eu_{0.5}ba_{0.5}tio_3$. *Phys. Rev. Lett.*, 109:193003, Nov 2012. doi: 10.1103/PhysRevLett.109.193003. URL https://link.aps.org/doi/10.1103/PhysRevLett.109.193003.

[30] Kia Boon Ng, Yan Zhou, Lan Cheng, Noah Schlossberger, Sun Yool Park, Tanya S. Roussy, Luke Caldwell, Yuval Shagam, Antonio J. Vigil, Eric A. Cornell, and Jun Ye. Spectroscopy on the electron-electric-dipole-moment–sensitive states of thf^+. *Phys. Rev. A*, 105:022823, Feb 2022. doi: 10.1103/PhysRevA.105.022823. URL https://link.aps.org/doi/10.1103/PhysRevA.105.022823. 5

[31] G. Feinberg. Effects of an electric dipole moment of the electron on the hydrogen energy levels. *Phys. Rev.*, 112:1637–1642, Dec 1958. doi: 10.1103/PhysRev.112.1637. URL https://link.aps.org/doi/10.1103/PhysRev.112.1637. 5

[32] P.G.H. Sandars. The electric dipole moment of an atom. *Physics Letters*, 14(3):194 – 196, 1965. ISSN 0031-9163. doi: https://doi.org/10.1016/0031-9163(65)90583-4. URL http://www.sciencedirect.com/science/article/pii/0031916365905834. 5

[33] S. A. Murthy, D. Krause, Z. L. Li, and L. R. Hunter. New limits on the electron electric dipole moment from cesium. *Phys. Rev. Lett.*, 63:965–968, Aug 1989. doi: 10.1103/PhysRevLett.63.965. URL https://link.aps.org/doi/10.1103/PhysRevLett.63.965. 5

[34] B. C. Regan, Eugene D. Commins, Christian J. Schmidt, and David DeMille. New limit on the electron electric dipole moment. *Phys. Rev. Lett.*, 88:071805, Feb 2002. doi: 10.1103/PhysRevLett.88.071805. URL https://link.aps.org/doi/10.1103/PhysRevLett.88.071805. 5

[35] N.J. Fitch and M.R. Tarbutt. *Chapter Three - Laser-cooled molecules*, volume 70 of *Advances In Atomic, Molecular, and Optical Physics*, pages 157–262. Academic Press, 2021. doi: https://doi.org/10.1016/bs.aamop.2021.04.003. URL https://www.sciencedirect.com/science/article/pii/S1049250X21000033. 6

[36] Malika Denis, Pi A. B. Haase, Rob G. E. Timmermans, Ephraim Eliav, Nicholas R. Hutzler, and Anastasia Borschevsky. Enhancement factor for the electric dipole moment of the electron in the baoh and yboh molecules. *Phys. Rev. A*, 99:042512, Apr 2019. doi: 10.1103/PhysRevA.99.042512. URL https://link.aps.org/doi/10.1103/PhysRevA.99.042512. 6

[37] Loïc Anderegg, Nathaniel B. Vilas, Christian Hallas, Paige Robichaud, Arian Jadbabaie, John M. Doyle, and Nicholas R. Hutzler. Quantum Control of Trapped Polyatomic Molecules for eEDM Searches. *arXiv pre-print*, 2023. URL https://doi.org/10.48550/arXiv.2301.08656. 6

[38] Yuly Chamorro, Anastasia Borschevsky, Ephraim Eliav, Nicholas R. Hutzler, Steven Hoekstra, and Lukáš F. Pašteka. Molecular enhancement factors for the $\mathcal{P},\mathcal{T}$-violating electric dipole moment of the electron in $BaCH_3$ and $YbCH_3$ symmetric top molecules. *Phys. Rev. A*, 106:052811, Nov 2022. doi: 10.1103/PhysRevA.106.052811. URL https://link.aps.org/doi/10.1103/PhysRevA.106.052811. 6

[39] Parul Aggarwal, Hendrick L. Bethlem, Anastasia Borschevsky, Malika Denis, Kevin Esajas, Pi A. B. Haase, Yongliang Hao, Steven Hoekstra, Klaus Jungmann, Thomas B. Meijknecht, Maarten C. Mooij, Rob G. E. Timmermans, Wim Ubachs, Lorenz Willmann, and Artem Zapara. Measuring the electric dipole moment of the electron in BaF. *The European Physical Journal D*, 72 (11):197, Nov 2018. ISSN 1434-6060. doi: 10.1140/epjd/e2018-90192-9. URL http://arxiv.org/abs/1804.10012. 6, 9, 10, 71, 73, 125, 126

[40] P. Aggarwal, H. L. Bethlem, A. Boeschoten, A. Borschevsky, K. Esajas, Y. Hao, S. Hoekstra, K. Jungmann, V. R. Marshall, T. B. Meijknecht, M. C. Mooij, R. G. E. Timmermans, A. Touwen, W. Ubachs, L. Willmann, Y. Yin, and A. Zapara. A supersonic laser ablation beam source with narrow velocity spreads. *Review of Scientific Instruments*, 92(3), March 2021. ISSN 0034-6748. doi: 10.1063/5.0035568. URL https://doi.org/10.1063/5.0035568. 6, 17, 22, 30, 72, 73, 74, 123

[41] Parul Aggarwal. *Production, deceleration and trapping of SrF molecules*. PhD thesis, University of Groningen, 2021. URL https://research.rug.nl/en/publications/production-deceleration-and-trapping-of-srf-molecules. 6, 17, 25, 26, 30, 125

[42] P. Aggarwal, V. R. Marshall, H. L. Bethlem, A. Boeschoten, A. Borschevsky, M. Denis, K. Esajas, Y. Hao, S. Hoekstra, K. Jungmann, T. B. Meijknecht, M. C. Mooij, R. G. E. Timmermans, A. Touwen, W. Ubachs, S. M. Vermeulen, L. Willmann, Y. Yin, and A. Zapara. Lifetime measurements of the $A\,^2\Pi_{1/2}$ and $A\,^2\Pi_{3/2}$ states in BaF. *Phys. Rev. A*, 100:052503, Nov 2019. doi: 10.1103/PhysRevA.100.052503. URL https://link.aps.org/doi/10.1103/PhysRevA.100.052503. 6, 17, 26, 40, 71, 72, 103

[43] Malika Denis, Pi A. B. Haase, Maarten C. Mooij, Yuly Chamorro, Parul Aggarwal, Hendrick L. Bethlem, Alexander Boeschoten, Anastasia Borschevsky, Kevin Esajas, Yongliang Hao, Steven Hoekstra, Joost W. F. van Hofslot, Virginia R. Marshall, Thomas B. Meijknecht, Rob G. E. Timmermans, Anno Touwen, Wim Ubachs, Lorenz Willmann, and Yanning Yin. Benchmarking of the Fock-space coupled-cluster method and uncertainty estimation: Magnetic hyperfine interaction in the excited state of BaF. *Phys. Rev. A*, 105:052811,

May 2022. doi: 10.1103/PhysRevA.105.052811. URL https://link.aps.org/doi/10.1103/PhysRevA.105.052811. 6, 71

[44] Anno Touwen. *Readout and control of molecules for electric dipole moment searches*. PhD thesis, University of Groningen, 2024. 6, 10, 23, 48, 63, 65, 66, 69, 124, 125, 126

[45] Alexander Boeschoten. *Precision measurements in diatomic molecules: a route to a permanent electric dipole moment*. PhD thesis, University of Groningen, 2023. URL https://research.rug.nl/en/publications/precision-measurements-in-diatomic-molecules-a-route-to-a-permane. 6, 9, 11, 12, 13, 16, 17, 18, 19, 25, 89, 90, 99, 103, 105, 110, 114, 119, 126

[46] A. Boeschoten, V. R. Marshall, T. B. Meijknecht, A. Touwen, H. L. Bethlem, A. Borschevsky, S. Hoekstra, J. W. F. van Hofslot, K. Jungmann, M. C. Mooij, R. G. E. Timmermans, W. Ubachs, and L. Willmann. Novel spin-precession method for sensitive EDM searches. *arXiv pre-print*, 2023. URL https://doi.org/10.48550/arXiv.2303.06402. 6, 19, 20, 85, 89, 103, 116, 118

[47] Maarten Mooij. *Thesis in preparation*. PhD thesis, University of Groningen, 2024. 6, 9, 17

[48] Maarten C. Mooij, Hendrick L. Bethlem, Alexander Boeschoten, Anastasia Borschevsky, Ties H. Fikkers, Steven Hoekstra, Joost W. F. van Hofslot, Klaus Jungmann, Virginia R. Marshall, Thomas B. Meijknecht, Rob G. E. Timmermans, Anno Touwen, Wim Ubachs, and Lorenz Willmann. A novel method to determine the phase-space distribution of a pulsed molecular beam, 2024. URL https://arxiv.org/abs/2401.16588v1.

[49] M C Mooij, H L Bethlem, A Boeschoten, A Borschevsky, K Esajas, T H Fikkers, S Hoekstra, J W F van Hofslot, K Jungmann, V R Marshall, T B Meijknecht, R G E Timmermans, A Touwen, W Ubachs, L Willmann, and Y Yin. Influence of source parameters on the longitudinal phase-space distribution of a pulsed cryogenic beam of barium fluoride molecules, 2024. URL https://arxiv.org/abs/2401.16590. 6, 9

[50] Kevin Esajas. *Intense slow beams of heavy molecules to test fundamental symmetries*. PhD thesis, University of Groningen, 2021. URL https://research.rug.nl/en/publications/intense-slow-beams-of-heavy-molecules-to-test-fundamental-symmetr. 6

[51] Artem Zapara. *Dynamics of molecular beams in a traveling-wave Stark decelerator*. PhD thesis, University of Groningen, 2019. URL https://research.rug.nl/en/publications/dynamics-of-molecular-beams-in-a-traveling-wave-stark-decelerator. 6

[52] P. Aggarwal, Y. Yin, K. Esajas, H. L. Bethlem, A. Boeschoten, A. Borschevsky, S. Hoekstra, K. Jungmann, V. R. Marshall, T. B. Meijknecht, M. C. Mooij,

R. G. E. Timmermans, A. Touwen, W. Ubachs, and L. Willmann. Deceleration and Trapping of SrF Molecules. *Phys. Rev. Lett.*, 127:173201, Oct 2021. doi: 10.1103/PhysRevLett.127.173201. URL https://link.aps.org/doi/10.1103/PhysRevLett.127.173201. 6, 17

[53] Anno Touwen, Joost W. F. van Hofslot, Thijs Qualm, Richard Borchers, Roman Bause, Hendrick L. Bethlem, Alexander Boeschoten, Anastasia Borschevsky, Ties H. Fikkers, Steven Hoekstra, Klaus Jungmann, Virginia R. Marshall, Thomas B. Meijknecht, Maarten C. Mooij, Rob G. E. Timmermans, Wim Ubachs, and Lorenz Willmann. Manipulating a beam of barium fluoride molecules using an electrostatic hexapole, 2024. URL https://arxiv.org/abs/2402.09300. 6, 10

[54] Yongliang Hao, Lukáš F. Pašteka, Lucas Visscher, Parul Aggarwal, Hendrick L. Bethlem, Alexander Boeschoten, Anastasia Borschevsky, Malika Denis, Kevin Esajas, Steven Hoekstra, Klaus Jungmann, Virginia R. Marshall, Thomas B. Meijknecht, Maarten C. Mooij, Rob G. E. Timmermans, Anno Touwen, Wim Ubachs, Lorenz Willmann, Yanning Yin, and Artem Zapara. High accuracy theoretical investigations of CaF, SrF, and BaF and implications for laser-cooling. *The Journal of Chemical Physics*, 151(3):034302, 2019. doi: 10.1063/1.5098540. URL https://doi.org/10.1063/1.5098540. 6, 10

[55] Yongliang Hao. *Theoretical investigations for testing the fundamental symmetries of the Standard Model with diatomic molecules*. PhD thesis, University of Groningen, 2020. URL https://research.rug.nl/en/publications/theoretical-investigations-for-testing-the-fundamental-symmetries. 6

[56] Pi Haase. *Electronic structure theory meets precision measurements*. PhD thesis, University of Groningen, 2021. URL https://pure.rug.nl/ws/portalfiles/portal/195934669/Propositions.pdf. 6

[57] Martin Jung. A robust limit for the electric dipole moment of the electron. *Journal of High Energy Physics*, 168, 2013. doi: 10.1007/JHEP05(2013)168. URL https://doi.org/10.1007/JHEP05(2013)168. 9

[58] Norman F. Ramsey. A molecular beam resonance method with separated oscillating fields. *Phys. Rev.*, 78:695–699, Jun 1950. doi: 10.1103/PhysRev.78.695. URL https://link.aps.org/doi/10.1103/PhysRev.78.695. 12

[59] David Patterson, Julia Rasmussen, and John M Doyle. Intense atomic and molecular beams via neon buffer-gas cooling. *New Journal of Physics*, 11(5): 055018, May 2009. doi: 10.1088/1367-2630/11/5/055018. URL https://dx.doi.org/10.1088/1367-2630/11/5/055018. 17

[60] Nicholas R. Hutzler, Maxwell F. Parsons, Yulia V. Gurevich, Paul W. Hess, Elizabeth Petrik, Ben Spaun, Amar C. Vutha, David DeMille, Gerald Gabrielse, and John M. Doyle. A cryogenic beam of refractory, chemically reactive molecules with expansion cooling. *Phys. Chem. Chem. Phys.*, 13:18976–18985, 2011. doi: 10.1039/C1CP20901A. URL http://dx.doi.org/10.1039/C1CP20901A. 17

[61] W. Demtröder. *Laser Spectroscopy*, volume 1: Basic Principles. Springer, 4th edition, 2008. ISBN 978-3-540-73415-4. URL https://link.springer.com/book/10.1007/978-3-662-08260-7. 18

[62] W. Demtröder. *Laser Spectroscopy*, volume 2: Experimental Techniques. Springer, 4th edition, 2008. ISBN 978-3-540-74952-3. URL https://link.springer.com/book/10.1007/978-3-662-44641-6.

[63] Ingolf V. Hertel and Claus-Peter Schulz. *Molecular Spectroscopy*. Springer Berlin Heidelberg, Berlin, Heidelberg, 2015. ISBN 978-3-642-54313. doi: 10.1007/978-3-642-54313-5. URL https://doi.org/10.1007/978-3-642-54313-5. 18

[64] C. D. Panda, B. R. O'Leary, A. D. West, J. Baron, P. W. Hess, C. Hoffman, E. Kirilov, C. B. Overstreet, E. P. West, D. DeMille, J. M. Doyle, and G. Gabrielse. Stimulated Raman adiabatic passage preparation of a coherent superposition of ThO $H^3\Delta_1$ states for an improved electron electric-dipole-moment measurement. *Phys. Rev. A*, 93:052110, May 2016. doi: 10.1103/PhysRevA.93.052110. URL https://link.aps.org/doi/10.1103/PhysRevA.93.052110. 18

[65] John M Brown and Alan Carrington. *Rotational spectroscopy of diatomic molecules*. Cambridge molecular science series. Cambridge University Press, Cambridge ; New York, 2003. ISBN 0521530784. URL https://www.cambridge.org/core/books/rotational-spectroscopy-of-diatomic-molecules/D22ED9CC569BFEA46F6C8ADACBA1138B. 20

[66] Rene Brun and Fons Rademakers. Root — an object oriented data analysis framework. *Nuclear Instruments and Methods in Physics Research Section A: Accelerators, Spectrometers, Detectors and Associated Equipment*, 389(1): 81–86, 1997. ISSN 0168-9002. doi: https://doi.org/10.1016/S0168-9002(97)00048-X. URL https://www.sciencedirect.com/science/article/pii/S016890029700048X. New Computing Techniques in Physics Research V. 23, 76, 101

[67] *Technical Information Wavelength Meter WS8-2*, Mar 2021. URL https://www.highfinesse.com/en/wavelengthmeter/wavelengthmeter-further-information/technical-information-wavelengthmeter-ws8-2.pdf. 40

[68] Kristian König, Phillip Imgram, Jörg Krämer, Bernhard Maaß, Konstantin Mohr, Tim Ratajczyk, Felix Sommer, and Wilfried Nörtershäuser. On the performance of wavelength meters: Part 2—frequency-comb based characterization for more accurate absolute wavelength determinations. *Applied Physics B*, 126(5):86, Apr 2020. ISSN 1432-0649. doi: 10.1007/s00340-020-07433-4. URL https://doi.org/10.1007/s00340-020-07433-4. 40, 82

[69] M. Verlinde, K. Dockx, S. Geldhof, K. König, D. Studer, T. E. Cocolios, R. P. de Groote, R. Ferrer, Yu. Kudryavtsev, T. Kieck, I. Moore, W. Nörtershäuser,

S. Raeder, P. Van den Bergh, P. Van Duppen, and K. Wendt. On the performance of wavelength meters: Part 1—consequences for medium-to-high-resolution laser spectroscopy. *Applied Physics B*, 126(5):85, Apr 2020. ISSN 1432-0649. doi: 10.1007/s00340-020-07425-4. URL https://doi.org/10.1007/s00340-020-07425-4. 40, 82

[70] Tesse Tiemans. Investigating the Viability of Using Avalanche Photodiodes for State Detection of BaF in the NL-eEDM Experiment, 2022. URL https://fse.studenttheses.ub.rug.nl/id/eprint/27906. 45

[71] *PMT1000 Series Photomultiplier Tubes User Guide.* Thorlabs, Jun 2019. URL https://www.thorlabs.de/drawings/2fe797cb6d2e7884-6F734540-DF94-B662-50A9249A922A4926/PMT1001_M-Manual.pdf. 45

[72] *Photomultipler Tube Modules.* Hamamatsu Photonics K.K, Mar 2019. URL https://www.hamamatsu.com/content/dam/hamamatsu-photonics/sites/documents/99_SALES_LIBRARY/etd/PMTmodules_TPMO0011E.pdf. 45, 139

[73] *MLS-85-SB Black Thermal Control Paint / Coating.* AZ Technology, 1997. URL https://www.aztechnology.com/product/13/mls-85-sb. 46

[74] *Product Specification Sheet, Photodiodes, FGA04.* Thorlabs, Dec 2010. URL https://www.thorlabs.com/drawings/d40c066308a75b99-73B92CA8-C743-4730-B978B582FF88C7C5/DET36A_M-Manual.pdf. 46

[75] *FDS1010 - Si Photodiode Spec Sheet.* Thorlabs, Feb 2017. URL https://www.thorlabs.com/drawings/d40c066308a75b99-73B92CA8-C743-4730-B978B582FF88C7C5/DET36A_M-Manual.pdf. 47

[76] *Hard-Coated UV/VIS/NIR Bandpass Filters.* Thorlabs, 2023. URL https://www.thorlabs.com/newgrouppage9.cfm?objectgroup_id=1860. 51, 54

[77] E. Kirilov, W. C. Campbell, J. M. Doyle, G. Gabrielse, Y. V. Gurevich, P. W. Hess, N. R. Hutzler, B. R. O'Leary, E. Petrik, B. Spaun, A. C. Vutha, and D. DeMille. Shot-noise-limited spin measurements in a pulsed molecular beam. *Phys. Rev. A*, 88:013844, Jul 2013. doi: 10.1103/PhysRevA.88.013844. URL https://link.aps.org/doi/10.1103/PhysRevA.88.013844. 53

[78] J. F. Barry, E. S. Shuman, and D. DeMille. A bright, slow cryogenic molecular beam source for free radicals. *Phys. Chem. Chem. Phys.*, 13:18936–18947, 2011. doi: 10.1039/C1CP20335E. URL http://dx.doi.org/10.1039/C1CP20335E. 53

[79] Elisabeth Bobrova Blyumin. Counting statistics of an electron electric dipole moment experiment. Bachelor's Thesis, University of Groningen, 2023, 2023. URL https://fse.studenttheses.ub.rug.nl/id/eprint/29700. 55

[80] *FS725 — Benchtop rubidium frequency standard*. Stanford Research Systems, 2015. URL https://www.thinksrs.com/downloads/pdfs/manuals/FS725m.pdf. 66

[81] V.R. Marshall, A. Boeschoten, T. B. Meijknecht, A. Touwen, H. L. Bethlem and A. Borschevsky, S. Hoekstra, J. W. F. van Hofslot, K. Jungmann, M. C. Mooij, R. G. E. Timmermans, W. Ubachs, L. Willmann. Resolved Hyperfine structure of BaF states, in preparation. 71

[82] W. E. Ernst, J. Kändler, and T. Törring. Hyperfine structure and electric dipole moment of BaF X $^2\Sigma^+$. *J. Chem. Phys.*, 84(9):4769–4773, 1986. doi: 10.1063/1.449961. URL https://doi.org/10.1063/1.449961. 71, 85

[83] C. Effantin, A. Bernard, J. d'Incan, G. Wannous, J. Vergès, and R.F. Barrow. Studies of the electronic states of the BaF molecule. *Molecular Physics*, 70(5): 735–745, 1990. doi: 10.1080/00268979000101311. URL https://doi.org/10.1080/00268979000101311. 71, 74, 87

[84] C. Ryzlewicz and T. Törring. Formation and microwave spectrum of the 2Σ-radical barium-monofluoride. *Chem. Phys.*, 51(3):329–334, 1980. doi: 10.1016/0301-0104(80)80107-8. URL https://doi.org/10.1016/0301-0104(80)80107-8. 71

[85] Wenhao Bu, Tao Chen, Guitao Lv, and Bo Yan. Cold collision and high-resolution spectroscopy of buffer-gas-cooled BaF molecules. *Phys. Rev. A*, 95: 032701, Mar 2017. doi: 10.1103/PhysRevA.95.032701. URL https://link.aps.org/doi/10.1103/PhysRevA.95.032701. 71

[86] Timothy C. Steimle, Sarah Frey, Anh Le, David DeMille, David. A. Rahmlow, and Colan Linton. Molecular-beam optical Stark and Zeeman study of the $A\,^2\Pi$–$X\,^2\Sigma^+$ (0,0) band system of BaF. *Phys. Rev. A*, 84:012508, 7 2011. doi: 10.1103/PhysRevA.84.012508. URL https://link.aps.org/doi/10.1103/PhysRevA.84.012508. 71, 87

[87] A. Bernard, C. Effantin, E. Andrianavalona, J. Vergès, and R. F. Barrow. Laser-induced fluorescence of BaF: Further results for six electronic states. *Journal of Molecular Spectroscopy*, 152(1):174–178, Mar 1992. ISSN 1096083X. doi: 10.1016/0022-2852(92)90127-A. URL https://www.sciencedirect.com/science/article/pii/002228529290127A?via{%}3Dihub.

[88] B. Guo, K.Q. Zhang, and P.F. Bernath. High-resolution fourier transform infrared emission spectra of barium monofluoride. *Journal of Molecular Spectroscopy*, 170(1):59–74, 1995. ISSN 0022-2852. doi: https://doi.org/10.1006/jmsp.1995.1056. URL https://www.sciencedirect.com/science/article/pii/S0022285285710569. 71

[89] Yuhe Zhang, Zixuan Zeng, Qian Liang, Wenhao Bu, and Bo Yan. Doppler cooling of buffer-gas-cooled barium monofluoride molecules. *Phys. Rev. A*, 105: 033307, Mar 2022. doi: 10.1103/PhysRevA.105.033307. URL https://link.aps.org/doi/10.1103/PhysRevA.105.033307. 71

[90] *Laser Power and Energy Meters Manual*. URL https://manualzz.com/doc/6519880/laser-power-and-energy-meters. 72

[91] Tao Chen, Wenhao Bu, and Bo Yan. Structure, branching ratios, and a laser-cooling scheme for the ^{138}BaF molecule. *Phys. Rev. A*, 94:063415, Dec 2016. doi: 10.1103/PhysRevA.94.063415. URL https://link.aps.org/doi/10.1103/PhysRevA.94.063415. 77

[92] P F Bernath, B Pinchemel, and R W Field. The hyperfine-structure of the calcium monohalides. *The Journal of Chemical Physics*, 74(10):5508–5515, 1981. ISSN 0021-9606. URL https://doi.org/10.1063/1.440957. 77

[93] B. E. Sauer, S. B. Cahn, M. G. Kozlov, G. D. Redgrave, and E. A. Hinds. Perturbed hyperfine doubling in the A2Π1/2 and [18.6]0.5 states of YbF. *The Journal of Chemical Physics*, 110(17):8424–8428, 05 1999. ISSN 0021-9606. doi: 10.1063/1.478751. URL https://doi.org/10.1063/1.478751. 77

[94] Alan Corney. *The width and shape of spectral lines*, chapter 8. Oxford University Press, 10 2006. ISBN 9780199211456. doi: 10.1093/acprof:oso/9780199211456.003.0008. URL https://doi.org/10.1093/acprof:oso/9780199211456.003.0008. 81

[95] E. A. Dijck, M. Nuñez Portela, A. T. Grier, K. Jungmann, A. Mohanty, N. Valappol, and L. Willmann. Determination of transition frequencies in a single ^{138}Ba^{+} ion. *Phys. Rev. A*, 91:060501, Jun 2015. doi: 10.1103/PhysRevA.91.060501. URL https://link.aps.org/doi/10.1103/PhysRevA.91.060501. 81

[96] L. Rozeboom. Two-photon transition for a measurement of the permanent electric dipole moment of the electron using BaF. Master's thesis, University of Groningen, 2021. URL https://fse.studenttheses.ub.rug.nl/24823/. 91, 92, 93, 95

[97] Alan Corney. *Atomic and Laser Spectroscopy*. Oxford University Press, 10 2006. ISBN 9780199211456. doi: 10.1093/acprof:oso/9780199211456.001.0001. URL https://doi.org/10.1093/acprof:oso/9780199211456.001.0001. 90

[98] I.J. Smallman. *A new measurement of the electron electric dipole moment using ytterbium fluoride*. PhD thesis, Imperial College London, 2013. URL https://www.imperial.ac.uk/media/imperial-college/research-centres-and-groups/the-centre-for-cold-matter/public/Joe-Smallman-2013.compressed.pdf. 99

[99] T. E. Chupp, P. Fierlinger, M. J. Ramsey-Musolf, and J. T. Singh. Electric dipole moments of atoms, molecules, nuclei, and particles. *Rev. Mod. Phys.*, 91:015001, Jan 2019. doi: 10.1103/RevModPhys.91.015001. URL https://link.aps.org/doi/10.1103/RevModPhys.91.015001. 121, 129

[100] C J Ho, J A Devlin, I M Rabey, P Yzombard, J Lim, S C Wright, N J Fitch, E A Hinds, M R Tarbutt, and B E Sauer. New techniques for a measurement of the electron's electric dipole moment. *New Journal of Physics*, 22(5):053031,

May 2020. doi: 10.1088/1367-2630/ab83d2. URL https://doi.org/10.1088/1367-2630/ab83d2. 123

[101] Tao Chen, Wenhao Bu, and Bo Yan. Radiative deflection of a baf molecular beam via optical cycling. *Phys. Rev. A*, 96:053401, Nov 2017. doi: 10.1103/PhysRevA.96.053401. URL https://link.aps.org/doi/10.1103/PhysRevA.96.053401. 123

[102] M. Abe, V. S. Prasannaa, and B. P. Das. Application of the finite-field coupled-cluster method to calculate molecular properties relevant to electron electric-dipole-moment searches. *Phys. Rev. A*, 97:032515, Mar 2018. doi: 10.1103/PhysRevA.97.032515. URL https://link.aps.org/doi/10.1103/PhysRevA.97.032515. 126

[103] D.M. Kara, I.J. Smallman, J.J. Hudson, B.E. Sauer, M.R. Tarbutt, and E.A. Hinds. Measurement of the electron's electric dipole moment using YbF molecules: methods and data analysis. *New Journal of Physics*, 14(10):103051, 2012. URL http://stacks.iop.org/1367-2630/14/i=10/a=103051. 127